

EFFECTS OF DIFFERENT DRAG-FREE SYSTEM ACCELERATION NOISE LEVELS
FOR FUTURE SATELLITE GEODESY MISSIONS

By

SEONG HYEON HONG

A DISSERTATION PRESENTED TO THE GRADUATE SCHOOL
OF THE UNIVERSITY OF FLORIDA IN PARTIAL FULFILLMENT
OF THE REQUIREMENTS FOR THE DEGREE OF
DOCTOR OF PHILOSOPHY

UNIVERSITY OF FLORIDA

2017

© 2017 Seong Hyeon Hong

To my mother in heaven and my lovely wife

ACKNOWLEDGMENTS

First of all, I owe many thanks to Dr. John W. Conklin for being my advisor. I know this research we worked on for past few years was very adventurous and required a lot of patience. In fact, I could not have completed this work without his teaching, guidance and patience. I also thank all my other committee members; Dr. Norman Fitz-Coy, Dr. Prabir Barooah and Dr. Guido Mueller for all of their time and considerations. I thank Stephen Apple from UF Precision Torsion Pendulum team for providing noise data and help plotting them. In addition, I thank all other colleagues from Precisions Space Systems Laboratory for all their support and friendship.

I thank David Wiese from JPL for his advises through emails and teleconferences and his comments during the conferences. I would also like to acknowledge Thomas Gruber from Technical University of Munich and Elisa Fagiolini from GFZ for providing additional information about their gravity field models. This research was funded by Florida Space Institute and I am very grateful of their support.

Numerous thanks to my parents for all their love and support. I am really proud to be your son. Special thanks to my lovely wife for all her care besides me. We did this together. I thank all my friends all over the world for their encouragements and prayers. Lastly and most importantly, I thank GOD for all his guidance, support and mercy he has shown me throughout my life. I came this far, all because of your allowance and the grace is all yours.

TABLE OF CONTENTS

	<u>page</u>
ACKNOWLEDGMENTS.....	4
LIST OF TABLES.....	7
LIST OF FIGURES.....	8
LIST OF ABBREVIATIONS.....	10
ABSTRACT	12
CHAPTER	
1 INTRODUCTION	14
History of Satellite Geodesy.....	14
Gravity Measurements before Satellite Geodesy	14
Satellite Geodesy	15
Early Satellite Geodesy Missions	15
The CHAMP Mission	16
The GRACE Mission	17
The GOCE Mission.....	19
The GRACE Follow-On Mission	19
Applications and Resolution Requirements of Gravity Measurements	20
Applications of Gravity Measurements	20
Resolution Requirements	21
Goals for Future Geodesy Missions.....	24
Motivation	25
Dissertation Contribution and Outline	27
2 BASIC THEORY IN SATELLITE GEODESY AND PREVIOUS STUDIES.....	29
Representation of Gravity (or gravitational) Potential	29
Analysis of Gravity Field	31
Satellite Formations	34
Singe Pair LL-SST	35
Double Pair LL-SST.....	36
Optimal Configurations	37
Drag-free Systems.....	38
Major Source of Errors.....	40
3 MISSION ARCHITECTURE.....	42
Orbit Selection	42
Ground Track Patterns.....	45

Technology and Associated Noise.....	48
Position and Range Noise Models.....	48
Acceleration Noise Models	49
Generating Colored Noise	51
Summary of the Simulation Design.....	52
4 ESTIMATION AND SIMULATION PROCEDURE	55
Gravity Model Selection	55
Creating Measurement Data.....	58
Estimation Method	59
Simulation Procedure.....	66
5 RESULT AND ANALYSIS.....	68
Representation of Solutions.....	68
Geoid Degree Difference Error	69
Equivalent Water Height	73
Discussion	82
6 IMPROVEMENTS IN ESTIMATION	88
State and Measurement Uncertainty	88
ARMA Filter	89
Accounting for Acceleration Noise in the Estimation Routine	93
Applying both the ARMA Approximation and the ANC	94
Result.....	95
Applying the ARMA Approximation and the ANC for Higher Acceleration Noise Level Mission.....	101
Discussion	105
7 TOOLBOX VALIDATION USING THE UF PRECISION TORSION PENDULUM .	108
UF Precision Torsion Pendulum	108
Accumulated Acceleration Noise	110
Result.....	113
Discussion	117
8 CONCLUSIONS AND RECOMMENDATIONS	119
Conclusions	119
Recommendations for Future Research	120
LIST OF REFERENCES	122
BIOGRAPHICAL SKETCH.....	127

LIST OF TABLES

<u>Table</u>		<u>page</u>
1-1	Applications of gravity measurements.....	20
2-1	Technology and associated residual acceleration noise.....	41
3-1	Summary of orbit parameters used for both the polar pair and inclined pair of satellites.....	47
3-2	Measurement technologies used in this analysis.....	48
3-3	LRI and Acceleration noise models used in this analysis.	49
3-4	Summary of simulation design with respect to error sources and launched missions.	54
4-1	Static and dynamic gravity models used in this analysis.	56
5-1	Spatial RMS errors for all cases in units of cm EWH.....	80
5-2	Differences between current and Wiese simulations.....	85
6-1	Spatial RMS error for Case A2 in units of cm of EWH with various MNC matrices.....	100
6-2	Spatial RMS error for Case A1 in units of cm of EWH with various MNC matrices.....	105
6-3	Spatial RMS error for Cases A1 and A2 in units of cm of EWH.....	107
7-1	Spatial RMS error for pendulum cases and Case A2 in units of cm of EWH....	117

LIST OF FIGURES

<u>Figure</u>		<u>page</u>
1-1	Time and spatial resolution requirements.....	22
1-2	Various static gravity solutions in geoid accuracy.....	23
2-1	Gravitational potential and spherical coordinate system.....	29
2-2	Reference ellipsoid, geoid and topography.	31
2-3	High-low and low-low satellite-to-satellite tracking.....	34
2-4	Single pair LL-SST configurations.	36
2-5	Double pair LL-SST configurations.....	37
2-6	Drag-free system.	39
3-1	Separation distance between the leading and trailing satellites as a function of time.....	44
3-2	Ground tracks of polar pair and inclined pairs of satellites.	46
3-3	The noise model and numerically generated noise.	53
4-1	Block diagram of the simulation procedure.....	67
5-1	Errors and Gaussian smoothed (GS) errors expressed as GDD using set 'A' true models.....	70
5-2	Errors and Gaussian smoothed (GS) errors expressed as GDD using set 'B' true models.....	71
5-3	Estimated solutions using the set 'A' true models. Units are in cm of EWH and the figure includes hydrology and ice mass variations.....	74
5-4	EWH error versus latitude plots for Cases A1 and A2.....	75
5-5	Estimated solutions using the set 'B' true models. Units are in cm of EWH and the figure includes hydrology and ice mass variations.....	78
5-6	EWH error versus latitude plots for Cases B1 and B2.....	79
6-1	ASD of the LRI generated noise, the ARMA filtered noise, and the noise model.....	93

6-2	ASD of the GOCE-level drag-free acceleration generated noise, the ARMA filtered noise, and the noise model.....	95
6-3	Errors of the ARMA and the ANC applied single pair solutions for Case A2 expressed as GDD.	97
6-4	Estimated single pair solutions for Case A2 in units of cm of EWH with various MNC matrices.	99
6-5	GS-applied single pair solutions for Case A2 in units of cm of EWH with various MNC matrices.	100
6-6	Errors of the ARMA and the ANC applied single pair solutions for Case A1 expressed as GDD.	102
6-7	Estimated single pair solutions for Case A1 in units of cm of EWH with various MNC matrices.	104
7-1	CAD model and actual apparatus of a torsion pendulum taken from Physics Space Laboratory at University of Florida in 2015.	109
7-2	Inertial members of a torsion pendulum taken from Physics Space Laboratory at University of Florida in 2017.	110
7-3	ASD of raw acceleration noise data.....	111
7-4	ASD of extracted acceleration noise data.....	112
7-5	ASD of actual pendulum noise, model-based simulated pendulum noise, and GOCE-level simulated acceleration noise.	113
7-6	Errors of the actual and the simulated UF pendulum noise applied single pair solutions expressed as GDD.	114
7-7	Estimated single pair solutions in units of cm of EWH applying the pendulum noise.....	115

LIST OF ABBREVIATIONS

ACS	Auto-covariance sequence
ANC	Acceleration noise covariance
AOD	Atmosphere and Ocean De-aliasing
AR	Auto-regressive
ARMA	Auto-regressive moving-average
ASD	Amplitude spectral density
BLUE	Best Linear Unbiased Estimator
CHAMP	Challenging Mini-Satellite Payload
CSR	Center for Space Research
DFAC	Drag-free Attitude Control
DOF	Degree of freedom
DORIS	Doppler Orbitography and Radiopositioning Integrated by Satellite
ECMWF	European Center for Medium-range Weather Forecast
EGG	Electrostatic Gravity Gradiometer
ESA	European Space Agency
EWH	Equivalent water height
FFT	fast Fourier transform
FTG	French Tidal Group
GDD	Geoid degree difference
GFZ	Geo Forschungs Zentrum
GNSS	Global Navigation Satellite System
GOCE	Gravity field and steady-state Ocean Circulation Explorer Mission
GPS	Global Positioning System
GRACE	Gravity Recovery and Climate Experiment

GRACE-FO	GRACE Follow-On
GRS	Gravitational reference sensor
GS	Gaussian Smoothing
HI	Hydrology and Ice
HL-SST	High-low satellite-to-satellite tracking
IFFT	Inverse fast Fourier transform
JPL	Jet Propulsion Laboratory
KBR	K-Band microwave ranging
LAGEOS	Laser Geodynamic Satellites
LISA	Laser Interferometer Space Antenna
LL-SST	Low-low satellite-to-satellite tracking
LRI	Laser ranging interferometer
MA	Moving-average
MNC	Measurement noise covariance
OMCT	Ocean Model for Circulation and Tides
PCCG	Preconditioned conjugate gradient
PPHA	Pacanowski, Ponte, Hirose and Ali
PSD	Power spectral density
RAAN	Right ascension of the ascending node
RK4	Runga-Kutta 4 th order
RMS	Root mean square
SLR	Satellite Laser Ranging
UF	University of Florida

Abstract of Dissertation Presented to the Graduate School
of the University of Florida in Partial Fulfillment of the
Requirements for the Degree of Doctor of Philosophy

**EFFECTS OF DIFFERENT DRAG-FREE SYSTEM ACCELERATION NOISE LEVELS
FOR FUTURE SATELLITE GEODESY MISSIONS**

By

Seong Hyeon Hong

May 2017

Chair: John W. Conklin
Major: Mechanical Engineering

This research evaluates the impact of residual acceleration noise on the estimation of the Earth's time-varying gravity field for future low-low satellite-to-satellite tracking missions.

The Gravity Recovery And Climate Experiment (GRACE) has provided monthly average gravity field solutions in spherical harmonic coefficients for more than a decade. It provides information about land and ocean mass variations with a spatial resolution of 350 km and with an accuracy within 2 cm throughout the entire Earth. GRACE Follow-on is expected to be launched in 2017 to advance the work of GRACE and to test a new laser ranging interferometer, which measures the range between the two satellites with higher precision than the K-Band ranging system used in GRACE. Moreover, there have been simulation studies that show, an additional pair of satellites in an inclined orbit increases the sampling frequency and thus reduces temporal aliasing errors.

Given the fact that future missions will likely continue to use the low-low satellite-to-satellite tracking formation with laser ranging interferometry, it is expected that the residual acceleration noise caused by non-gravitational forces and aliasing errors will

become limiting factors for the time-varying gravity field solution. We evaluate three different levels of residual acceleration noise based on demonstrated drag-free systems to find an optimal drag-free performance target for upcoming geodesy missions. We analyze both a single collinear polar pair and the optimal double collinear pair of drag-free satellites and assume the use of a laser ranging interferometer, performing estimation with two different sets of de-aliasing models to represent different levels of aliasing errors. A partitioned best linear unbiased estimator is used to compute the solutions in terms of spherical harmonics. The estimation routine was improved with precise modeling of the measurement noise covariance matrix and the entire simulation toolbox was tested by using the actual residual acceleration noise data from the UF precision torsion pendulum. It was found that the suitable residual acceleration noise is around $2 \times 10^{-12} \text{ ms}^{-2}\text{Hz}^{1/2}$. Decreasing the acceleration noise below this level did not result in more accurate gravity field solutions for the chosen mission architecture.

CHAPTER 1

INTRODUCTION

History of Satellite Geodesy

Gravity Measurements before Satellite Geodesy

Geodesy is a field of study that examines the measurements, which determine the physical quantities of the Earth. Gravity field (or potential) is one of the key measurements in geodesy, which quantify the mass distribution and hence the approximate shape of the Earth. Before the satellite geodesy era, the gravity field was measured locally by mechanical devices such as pendulums, torsion balances, static springs and etc. [Nerem et al., 1995]. Each of these devices works in different ways, and as a consequence they have different equations of motion. Classical pendulums for instance can measure the gravity by direct measurements of the period of oscillation with known mass and length of the pendulum. From the equation of motion, the natural frequency of the pendulum can be calculated and this can be converted to the local gravitational strength. The method is similar for torsion balances and static springs. If the characteristics of mechanical devices are known and the angular or translational movements are measured, signals produced by these devices can be converted to local gravity measurements. These measurements have been improved by many years of work to increase the accuracy. However, each measurement can only provide information from the specific point where the measurement was taken. Consequently with local measurements, it becomes almost impossible to measure the entire gravity field of the Earth since it requires numerous devices and efforts. Another complication is that each device has to be calibrated absolutely with high accuracy so that it can be compared with results from different measurement devices. Furthermore, some places

are prohibited by environmental conditions or political boundaries. New technology was desired to measure the gravity field of the entire Earth.

Satellite Geodesy

Satellite geodesy is a branch of geodesy that uses satellites orbiting around the Earth, mainly determining the gravity potential with the measurements taken from the satellites. These measurements include position, velocity and acceleration of the satellites, which can be used to estimate the gravity field of the Earth using the equation of motion of the satellites. Since the Earth does not have a uniform mass, it exerts different gravitational forces on the satellites at different positions and effects their flight paths. Therefore, by measuring and observing the path of satellites, one can recover the gravitational potential of the Earth. Satellite geodesy became the best way to measure the global gravity field of the Earth since satellites do not have any boundaries and can observe the entire Earth within short period of time.

Early Satellite Geodesy Missions

Satellite geodesy era began with the first satellite, Sputnik in 1957. It was limited by a discontinuous tracking system using cameras, radio Doppler and radio interferometry. Satellite Laser Ranging (SLR) was introduced in mid-1960s and it was demonstrated in Laser Geodynamic Satellites (Lageos) launched in 1976 [Nerem et al., 1995]. The accuracy of SLR with the LAGEOS mission was about 2 cm, which was a big improvement from camera tracking system which had an accuracy of about 10 m [Nerem et al., 1995]. However, there were still limitations in satellite geodesy caused by the discontinuous tracking of SLR due to high cost of ground stations and weather uncertainty. In 1990s, continuous tracking by the French Doppler Orbitography and Radiopositioning Integrated by Satellite (DORIS) system was developed [Nerem et al.,

1995]. DORIS measures the continuous range rate between the satellites and the ground stations by emitting radio signals from 50 ~ 60 ground stations, and satellites receiving these signals and measuring the Doppler shifts. The accuracy of range rate measurements were about 0.3 to 0.5 mm/s and these measurements were used to estimate the orbits of satellites with accuracy of 2.5 cm [Seeber, 2003]. Around that time, the U.S. developed another continuous tracking system called the Global Positioning System (GPS), which was first demonstrated by TOPEX/Poseidon in 1992 [Nerem *et al.*, 1995]. GPS tracking of a low Earth orbiting satellite for the purpose of Earth geodesy measurements is known as high-low satellite-to-satellite tracking (HL-SST) [Kim, 2000]. GPS can achieve the orbit determination accuracy of as low as 1 cm [Kang *et al.*, 2006]. This class of measurements provide continuous position and velocity of satellites with respect to the Earth. GPS along with DORIS initiated an escalation of accurate gravity field measurements. Nevertheless, these technologies were not sufficient to measure high spatial and temporal frequency gravity field signals with high accuracy.

The CHAMP Mission

Challenging Mini-Satellite Payload (CHAMP) (2000 ~ 2010) mission was launched in a near polar orbit and altitude of 450 km. This was a pre-GRACE technology and science mission, launched 2 years before the actual GRACE mission, which is explained in the following paragraph. CHAMP consisted of a GPS receiver for continuous tracking and an electrostatic accelerometer to measure in-orbit non-gravitational forces [Reigber *et al.*, 2003]. Different types of non-gravitational forces are explained later in this dissertation. CHAMP was the first satellite geodesy mission that enabled 550 km spatial resolution gravitational field solutions called EIGEN-2. These

CHAMP-only solutions were at least an order of magnitude improvement compared to previous satellite-only solutions [Reigber *et al.*, 2003]. Also, before the CHAMP mission, all the gravity solutions acquired by satellite missions were mostly used to build static models, which means that the solutions represent average gravity potential of the Earth which do not change with time. On the contrary, the gravity potential of the Earth varies with the time due to the mass variations of the Earth. Dynamic gravity solutions represent the variations of the gravity potential with respect to the static potential. Static and dynamic solutions are explained more in the following section of this chapter.

Combination of the data provided by CHAMP and SLR from other five geodetic satellites, Lageos 1 and 2, Stella, Starlette, and Ajisai produced the annual and semiannual dynamic gravity field solutions with high spatial resolution [Moore *et al.*, 2005].

The GRACE Mission

Gravity Recovery and Climate Experiment (GRACE) (2002 ~ present) started a new era of gravity field measurement. GRACE is a mission committed to measuring the Earth's gravity field corresponding to a mass distribution on the surface of the Earth once per month. This mission consists of two identical satellites flying at the initial altitude of around 500 km (currently around 400 km) in nearly circular polar orbits one trailing the other by about 220 km (170 km ~ 270 km). Each satellite is an identical design from the CHAMP mission but GRACE has the updated electrostatic accelerometers and an additional K-Band microwave ranging (KBR) system between the two. This measures the range rate between the satellites [Tapley *et al.*, 2004]. This type of tracking is known as low-low satellite-to-satellite tracking (LL-SST), which is explained more in Chapter 2. The KBR system not only provides additional

measurements from another satellite but also keeps track of range between the pair, which plays an important role in increasing the time and spatial resolution and accuracy of gravity field models [Kim, 2000]. The KBR system provides range measurements with an accuracy of less than 10 μm , which is more accurate by about three orders of magnitude than the range measurement acquired by GPS [Tapley *et al.*, 2004]. GRACE solutions are produced monthly with spatial resolution on the surface of the Earth of ~350 km. With advancements in estimation techniques, the temporal resolution has decreased to as low as one day, although this requires prior information for a hydrological model [Kurtenbach *et al.*, 2009; Sakumura *et al.*, 2016]. Moreover, the accuracy of the monthly solutions were improved at least by 20% over the ocean through numerical modeling of the non-conservative acceleration and attitude errors [Chen *et al.*, 2016]. On the other hand, a new calibration method for the GRACE accelerometer data that considers temperature effects on the measurements, showed an improvement in estimating the C20 spherical harmonic coefficients [Klinger and Mayer-Gürr, 2016]. Apart from these previous research efforts, the most important lesson from GRACE was that accelerometer noise was conjectured to be the dominating uncertainty for measurement frequencies between ~0.2 mHz and 2~3 mHz, and at frequencies above 2~3 mHz, the noise of the microwave ranging system was speculated to be the limiting factor for the gravity field solution [Sheard *et al.*, 2012]. Therefore, a Laser Ranging Interferometer (LRI) was developed, which is expected to reduce the satellite-to-satellite ranging noise by at least factor of 5 compared to the noise of the GRACE microwave ranging system [Sheard *et al.*, 2012]. The LRI is going

to be tested by GRACE Follow-On (GRACE-FO), which is scheduled to be launched in 2017 to continue the work of GRACE [*Flechtner et al.*, 2014].

The GOCE Mission

After GRACE, the Gravity field and steady-state Ocean Circulation Explorer (GOCE) (2009 ~ 2013) was launched [*Floberghazen et al.*, 2011]. The mission's objective was to recover static gravity field and reach geoid accuracy of 1~2 cm with spherical harmonics of degree 200 which is equivalent to spatial resolution of 100 km. In order to reach a high spatial resolution solution, GOCE was flying at the low altitude of 279 km and inclination of 96.7° in near circular orbit [*Floberghazen et al.*, 2011]. GOCE was equipped with an Electrostatic Gravity Gradiometer (EGG) and Drag-free Attitude Control (DFAC) system [*Canuto and Massotti*, 2009]. These two comprised a drag-free system (system that provides satellites to fly in a purely gravitational orbit), which will be explained in Chapter 2. The EGG reduced the acceleration noise down to $2 \times 10^{-12} \text{ ms}^{-2} \text{Hz}^{-1/2}$ for frequency of 5 mHz ~ 0.1 Hz [*Touboul et al.* 2012]. However, the actual residual acceleration noise of this drag-free system was higher due to the actuator performance. Overall, the performance of GOCE drag-free system was better than that of the electrostatic accelerometer used in GRACE.

The GRACE Follow-On Mission

The GRACE Follow-On (GRACE-FO) mission, implemented by a US-German partnership will continue the work of GRACE with minimum gap in the data stream for 5 more years, and it is scheduled to be launched in 2017 [*Flechtner et al.*, 2014]. GRACE-FO will be launched into a circular orbit with 490 km altitude and 89° inclination angle similar to GRACE. There are two main objectives for GRACE-FO. One is to continue

the measurements and observations of the current GRACE mission and another is to demonstrate the performance of a Laser Ranging Interferometer (LRI), which is expected to improve low-low satellite-to-satellite tracking (LL-SST) measurement, and increasing the accuracy of gravity field estimation with the same spatial and time resolution as GRACE [Sheard *et al.*, 2012]. The instrument of GRACE-FO is based on that of GRACE and the major change is having LRI along with KBR (ranging instrument used in GRACE) to guarantee the performance of GRACE. The number of star cameras to measure the attitude of GRACE has been increased from two to three and the configuration of these cameras has been modified to improve attitude determination. SuperSTAR accelerometers used in GRACE are planned to be used in GRACE-FO to measure the effects of non-gravitational forces.

Applications and Resolution Requirements of Gravity Measurements

Applications of Gravity Measurements

Table 1-1. Applications of gravity measurements [Sneeuw *et al.*, 2005].

Science Area	Theme
Solid Earth	glacial isostatic adjustment, co-/post-seismic deformation, slow/silent earthquakes, plate tectonics, mantle convection, volcanos, core motion, seismic normal modes
Hydrology	snow, precipitation, ground water, dams, soil moisture, run-off, evapo-transpiration
Ocean	mean flow, coastal currents along shelf edges, interaction mean and eddy flow, ocean fronts position, bathymetry, basin scale mass change, deep water formation, bottom currents
Sea Level	global sea level change monitoring
Ice	ice mass balance, bottom topography, ice compaction
Geodesy	precise heights for engineering, GNSS levelling, coastal height reference, sea level monitoring, inertial navigation, atmosphere, planets

There has been a great development and improvement in the gravity measurements of the Earth for the past few decades due to the various satellite missions as introduced in previous section. This would not be accomplished if the gravity measurements were not useful. In fact, these measurements are widely used in scientific areas as shown in Table 1-1 [Sneeuw *et al.*, 2005]. The core motivation of these listed scientific areas arises from the idea of observing and studying the planet that we are living in such that we can predict and prepare for the future.

Resolution Requirements

For each scientific themes listed in Table 1-1, there is a resolution requirement for the gravity solution which is quantified by spatial and time (temporal) resolutions. There are limitations on both spatial and time resolutions with current technology and each space mission aims to achieve specific resolutions for different purposes. Resolution requirement for each science theme is shown in Figure 1-1. This figure also shows the targeting resolutions for GRACE and GOCE missions. As explained in a previous section, GOCE focused on increasing the spatial resolution by lowering the altitude with a drag-free system, whereas GRACE was focused more on increasing the time resolution using low-low satellite-to-satellite tracking within a reasonable band of spatial resolution. The actual mission measurements showed that GRACE achieved a spatial resolution of about 350 km with roughly 2 cm geoid accuracy for monthly solutions, which was better than what was expected [Save *et al.*, 2016]. This was due to the advances in the estimation technique and continuously updated a priori information. Also as explained earlier, time resolution can be reduced to daily solutions. However, when daily solutions were computed the spatial resolution was only 500 km [Kurtenbach

et al., 2009]. In sum, there is a tradeoff between the time resolution and the spatial resolution.

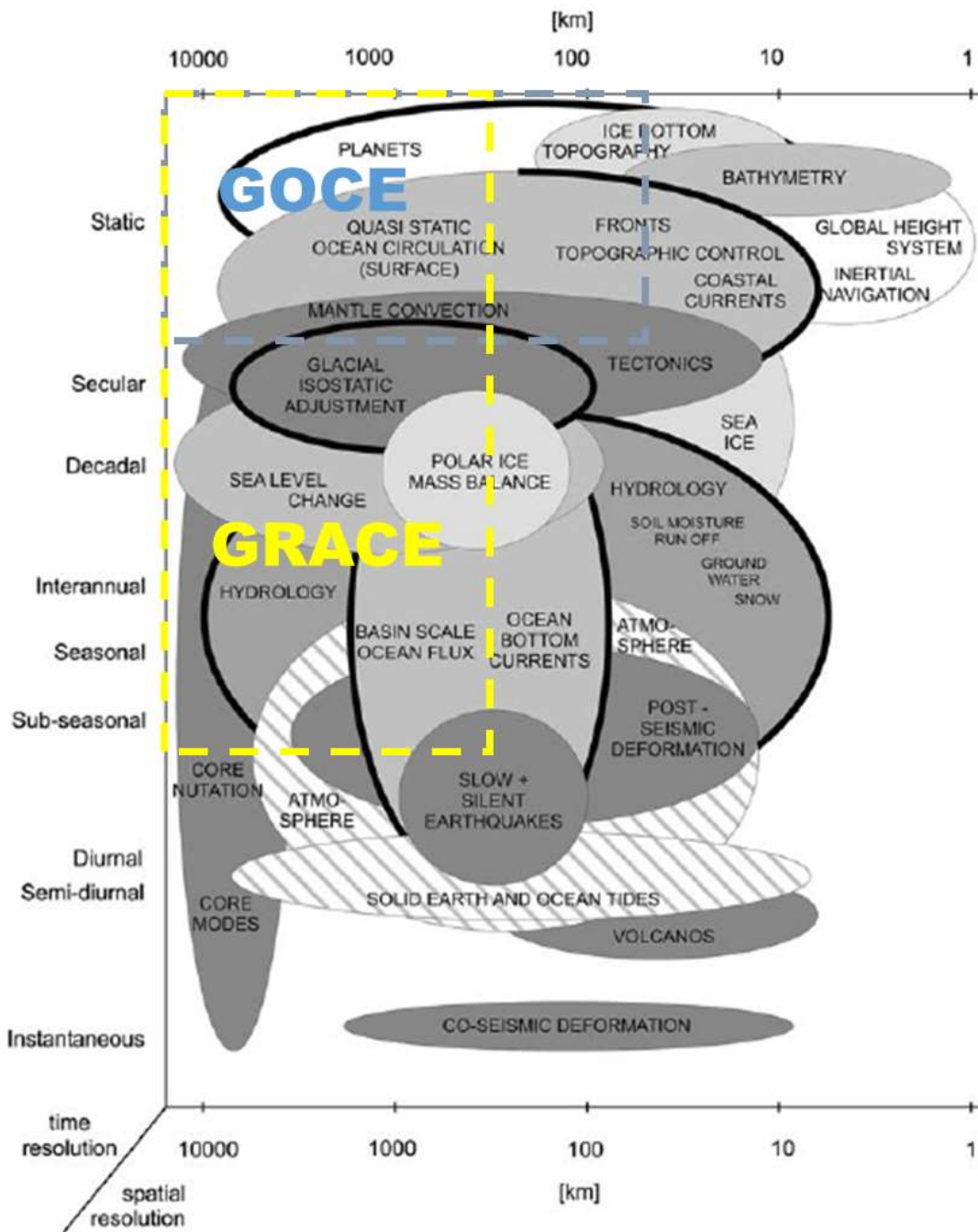


Figure 1-1. Time and spatial resolution requirements [Sneeuw *et al.*, 2005].

It is important to note what limits resolution. The current limit of spatial resolution is about 100 km and the time resolution is semi-diurnal for single pair LL-SST missions.

To achieve higher spatial resolution, satellites must fly at low altitudes of less than 250 km. This is achievable by applying drag-free systems, but it will require a lot of fuel to maintain the orbit and therefore shorten the mission lifetime dramatically. In terms of time resolution, it is difficult to achieve less than semi-diurnal resolution, because to get a full coverage of the Earth with single satellite, requires more than half a day, even when the satellite is in a low altitude polar orbit. Multiple satellites can be used to solve this problem, but it will require a larger amount of cost.

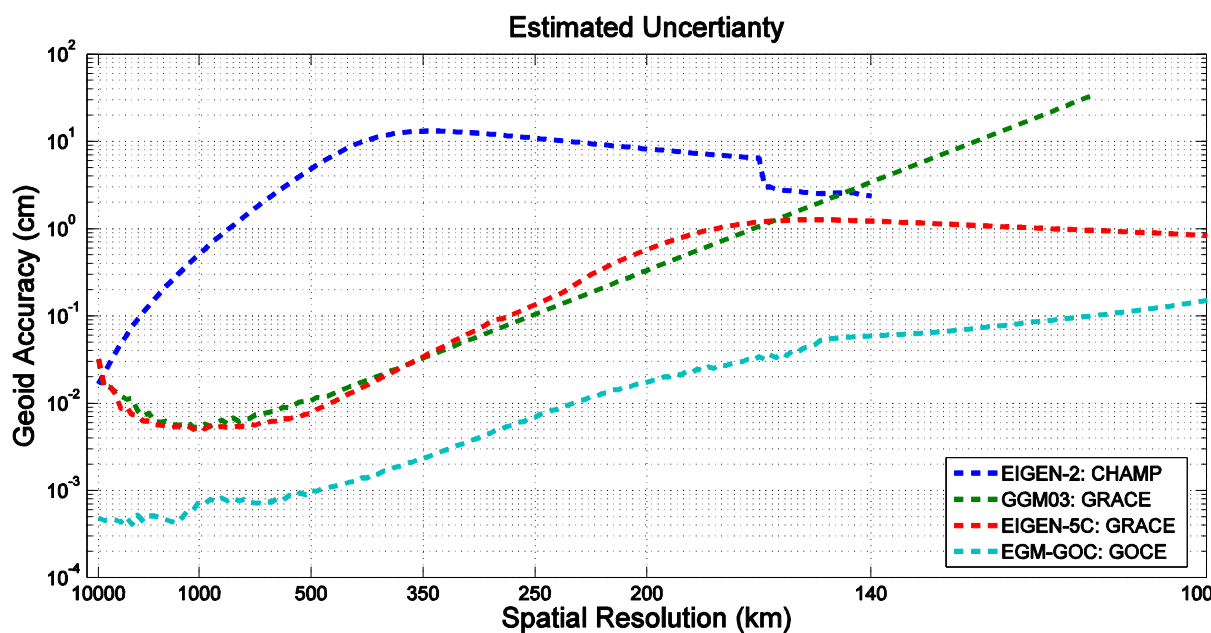


Figure 1-2. Various static gravity solutions in geoid accuracy.

Nevertheless, it is essential to understand that the accuracy of solution is different from the resolutions. Gravity solutions need to achieve certain accuracy with given time and spatial resolutions. Geoid accuracy is often calculated to evaluate the solution. Geoid accuracy simply means the gravity solution expressed in terms of a distance. The definition and details of the geoid calculation will be explained in Chapter 2. Figure 1-2 shows the accuracy of the static gravity solutions, in terms of geoid

accuracy versus spatial resolution, derived from the measurements of different missions or combinations of missions.

The CHAMP-based solution is called EIGEN-2, which has the accuracy below 10 cm [*Reigber et al.*, 2003]. This solution is only based on the measurements taken by CHAMP up to the spatial resolution of 500 km. Solutions beyond this resolution depends on other existing models. GGM03 is the GRACE-based solution, which used four years of accumulated monthly solutions to recover the static gravity field with spatial resolution close to 100 km [*Tapley et al.*, 2007]. EIGEN-5C is a static solution based on combining the data from LAGEOS and GRACE with spatial resolution of less than 100 km [*Foerste et al.*, 2008]. EGM_GOC is a GOCE-based solution, but also used the data from LAGEOS and GRACE [*Bruinsma et al.*, 2013]. This also has the spatial resolution of less than 100 km. Figure 1-2 shows that the GOCE drag-free system which compensates for the effects of non-gravitational forces, provides more accurate gravity solution. Furthermore, this figure shows that the static solution can be recovered by using a combination of data from different missions. This implies that there are already a lot of data collected to recover the static gravity field. Therefore, future gravity missions will focus on precisely recovering dynamic gravity solutions.

Goals for Future Geodesy Missions

Starting from the GRACE mission, the low-low satellite-to-satellite tracking (LL-SST) configuration has become a standard tracking system for satellite geodesy missions aiming for spatial resolutions down to 100 km and time resolution as short as one day. Therefore, the GRACE-FO mission will be launched with same LL-SST system. This GRACE-FO mission will soon represent the state of the art for satellite geodesy missions. It is speculated that the LRI will reduce the high frequency

measurement noise in GRACE-FO, but acceleration noise and aliasing errors will continue to dominate the uncertainty of the solution. It is therefore likely that drag-free systems or more accurate electrostatic accelerometers will be employed with laser ranging interferometry in future missions beyond GRACE-FO. Loomis (2012) already showed, through simulation, that LRI does not improve the solution with the same accelerometers used in GRACE, but modest improvements can be made by applying the LRI with a drag-free system and lowering the altitude. In contrast to this work, a recent simulation done by Flechtner (2016) showed improvements of 23% on a global scale using LRI and GRACE-like accelerometers, although different acceleration noise levels were not considered. Indeed, many other simulation studies for future missions, including those of Wiese (2012) and Elsaka (2014), assume the acceleration noise of the GOCE drag-free system and the accuracy of LRI based on the same speculations regarding the limiting error sources. Moreover, the benefits of multiple pairs of satellite have also been evaluated. These analysis determine design considerations for optimizing gravity recovery missions for two pairs of satellites in in-line configurations, also known as a Bender formation, and this showed a positive result [Wiese *et al.*, 2012]. The main purpose of using multiple pairs of satellites is to increase the sampling frequency to detect changes in the gravity field with higher accuracy. Using multiple pairs of satellites might not be feasible due to its high cost. However, development of small satellites is actively pursued in various groups since small satellites are less expensive, although relatively low accuracy of measurements is still an issue.

Motivation

Given the necessity of gravity solutions in the broad science community, it is required to continue the work of satellite geodesy. For every gravity field recovery, there

are spatial and time resolutions to satisfy and a certain level of accuracy is required for the given resolutions. Consequently, there has been continuous technology development to improve the gravity solutions. In advance of the development of GPS, the estimation of gravity potential was limited by the discontinuous tracking system. When the HL-SST system was established, the gravity solution was limited by the non-gravitational forces. The electrostatic accelerometer was developed to measure the acceleration caused by the non-gravitational forces starting from CHAMP. After CHAMP, GRACE initiated the LL-SST which measured the range between the two satellites. This new type of data played a huge role in increasing the resolutions and accuracies of gravity solutions. However, the microwave ranging system from GRACE is speculated to be the limiting factor for high frequency gravity solutions. Therefore, the Laser Ranging Interferometer (LRI) was introduced, which is expected to operate with noise smaller by at least one order of magnitude compared to the noise of the microwave ranging system. The LRI is soon going to be tested by GRACE-FO, and if it operates as expected, temporal aliasing error and residual acceleration noise are likely to be the limiting factors for the gravity field recovery. Drag-free systems decrease the residual acceleration noise and therefore increase the accuracy of gravity solutions. Consequently, drag-free systems will be required in future geodesy missions and the necessity for drag-free systems was already proved through the GOCE mission. Also, temporal aliasing errors, caused by the under-sampling of the dynamic signals, needs to be dealt with. Numerical filters can be used to remove this temporal aliasing error, but these filters act as a low pass filters and remove the true high frequency gravity signals along with the error. Thus, multiple pairs of satellites or updated de-aliasing models may

be used to decrease the error caused by the under-sampling. Because these new technologies and methods are being considered for missions beyond GRACE-FO, there have been several simulation studies including Wiese (2012) and Elsaka (2013, 2014) to evaluate them. In these simulations, the effects of applying an additional pair of satellites and different configurations were explored. However, there is no study done yet to find the optimal acceleration noise level for the drag-free system, although the GOCE level of acceleration noise was used in many simulations. Therefore, it is necessary to explore the effects of the acceleration noise level of drag-free systems for different magnitudes of aliasing error.

Dissertation Contribution and Outline

Based on the motivation above, there are three main goals for this research. The first is to develop a toolbox to simulate gravity field recovery for satellite geodesy missions. This includes creating satellite data and an estimation routine. We describe this new optimal estimation routine, incorporating several novel features that was developed from the ground up for this study. Second goal is to utilize the actual device noise from UF precision torsion pendulum to validate the performance of the toolbox and observe how these technologies can change the performance of LL-SST missions. The last goal is to find the optimal residual acceleration noise level for future LL-SST missions. Here, we present the results of a new analysis of drag-free LL-SST missions that considers a range of residual acceleration noise levels, where all other mission parameters are held constant, corresponding to the latest measurement technology and optimal orbit configurations. We examine drag-free acceleration noise performance equivalent to that of the GRACE electrostatic accelerometers, the GOCE drag-free system, and the LISA Pathfinder drag-free system. For each, we estimate the Earth's

gravity potential, expanded in spherical harmonics up to degree and order 60, and evaluate the geopotential estimation error as a function of acceleration noise. Both single polar pair (in-line) and two pairs (in-line Bender) optimal configurations are analyzed. Moreover, the cases of having realistic and idealistic de-aliasing models were also explored to observe the cases with different aliasing error levels. Furthermore, estimation routine was improved by considering the correlation of the noise and acceleration noise effects on the measurement data.

There are eight chapters in this dissertation, seven excluding this introduction chapter. Chapter 2 deals with basic theory and previous studies of satellite geodesy and drag-free systems. Chapter 3 presents the mission architecture, which is equivalent to designing a future geodesy mission. Chapter 4 explains the estimation routine and the simulation steps that are developed. Chapter 5 presents the results and analysis. Chapter 6 revisits the estimation routine and shows steps to improve the solution. The UF precision torsion pendulum is introduced in Chapter 7 to validate the toolbox using the actual device noise data. Chapter 8 provides final remarks and recommendations for future research.

CHAPTER 2

BASIC THEORY IN SATELLITE GEODESY AND PREVIOUS STUDIES

Gravity field solutions are often represented in spherical harmonics. This chapter explains the relation between these coefficients and the equation of motion of drag-free satellites. Also, there are descriptions of how the coefficients are evaluated in different ways. Major concepts that are necessary in the field of satellite geodesy, such as satellite configurations, drag-free systems, and major error sources are also explained in this chapter.

Representation of Gravity (or gravitational) Potential

The gravitational potential is a measure of how much work is applied by gravitational force at given distance per unit mass. Figure 2-1 represents the gravitational potential at point P with respect to the unknown mass v [Heiskanen and Moritz, 1967]. The equation for this gravity potential at point P is defined by Equation (2-1) [Heiskanen and Moritz, 1967].

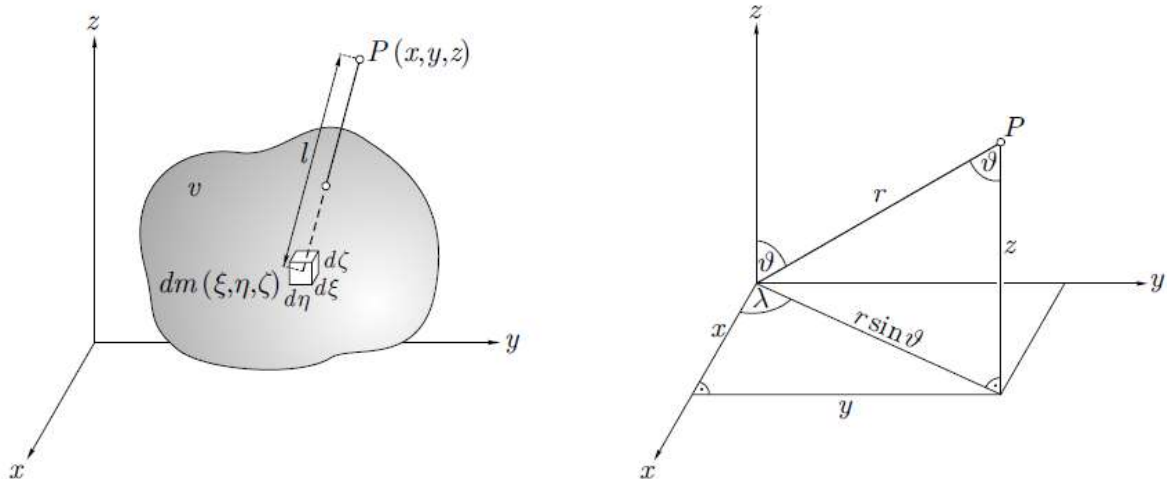


Figure 2-1. Gravitational potential and spherical coordinate system [Heiskanen and Moritz, 1967].

$$U(x, y, z) = G \iiint_v \frac{\rho(\xi, \eta, \zeta)}{\sqrt{(x - \xi)^2 + (y - \eta)^2 + (z - \zeta)^2}} d\xi d\eta d\zeta \quad (2-1)$$

Here, U is the gravitational potential at point P , G is gravitational constant and ρ is density of the unknown mass element. Therefore, if this unknown mass is the mass of the Earth and ρ is the average density of the Earth, then U is the gravitational potential at point P caused by the gravitational force of the Earth. It is easier to analyze the gravitational potential in a spherical coordinate system as shown in Figure 2-1 and the converted equation is shown below [Heiskanen and Moritz, 1967].

$$U(r, \vartheta, \lambda) = \frac{GM_{\oplus}}{r} \sum_{n=0}^{\infty} \sum_{m=0}^n \frac{R_{\oplus}^n}{r^n} P_{nm}(\cos \vartheta)(C_{nm} \cos(m\lambda) + S_{nm} \sin(m\lambda)) \quad (2-2)$$

$$\begin{aligned} P_{nm}(t) &= (1 - t^2)^{m/2} \frac{d^m P_n(t)}{dt^m} \\ P_n(t) &= P_{n0}(t) \end{aligned} \quad (2-3)$$

$$P_0(t) = 1$$

Now, U is expressed in spherical (r, ϑ, λ) coordinates instead of Cartesian (x, y, z) coordinates, where r is the distance between the point P and center of mass of the Earth, ϑ is colatitude and λ is longitude. Unknown constants, M_{\oplus} and R_{\oplus} are the mass and radius of the Earth respectively. Operator, P_{nm} , is the associated Legendre polynomial of degree n and order m . The associated Legendre polynomial, P_{nm} , is defined as shown in Equation (2-3) [Heiskanen and Moritz, 1967]. Most importantly, C_{nm} and S_{nm} are the geopotential spherical harmonic coefficients, which define the magnitude of gravity potential. These coefficients are parameters that need to be estimated and are often referred to as the gravity field solution. The gravity field represents the gravitational force applied per unit mass which is similar to gravitational

potential but it represent the force itself instead of the work done by that force. The degree and order of these coefficients define the number of parameters used to define the gravitational potential of the Earth. Hence, the larger the degree and order of coefficients, the higher the spatial resolution.

The acceleration of point P due to the gravitational force of the Earth can be calculated by taking the gradient of gravitational potential as shown in Equation (2-4) [Heiskanen and Moritz, 1967]. This equation is equivalent to the equation of motion for pure drag-free satellites.

$$\ddot{\vec{r}} = \nabla \frac{GM_{\oplus}}{r} \sum_{n=0}^{\infty} \sum_{m=0}^n \frac{R_{\oplus}^n}{r^n} P_{nm}(\cos \vartheta) (C_{nm} \cos(m\lambda) + S_{nm} \sin(m\lambda)) \quad (2-4)$$

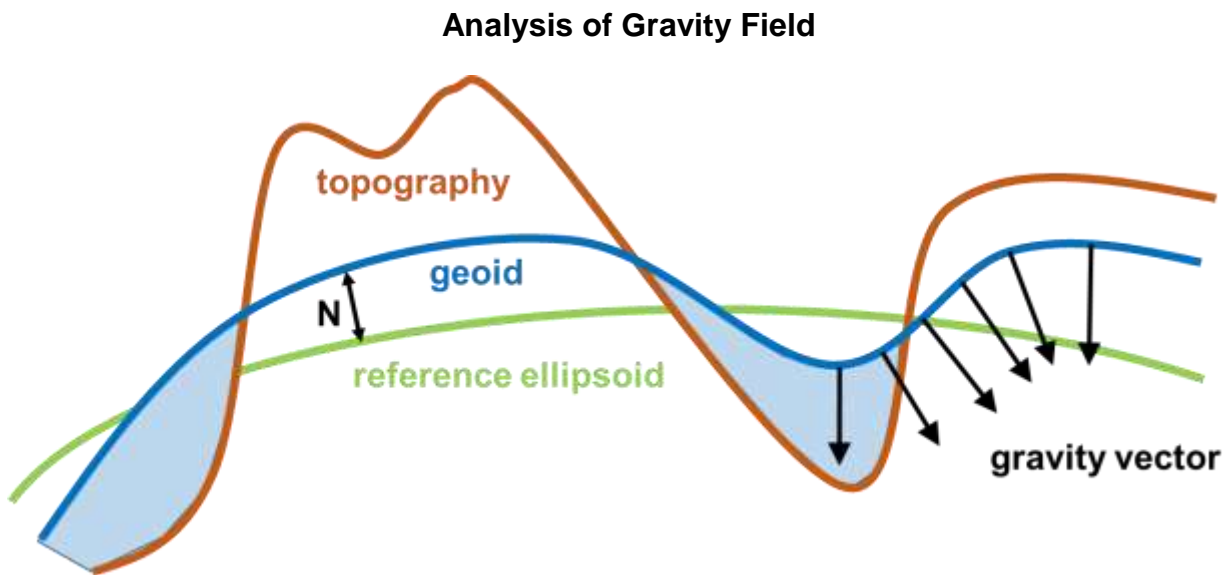


Figure 2-2. Reference ellipsoid, geoid and topography [Barthelmes, 2013].

The definition of the geoid is essential in understanding gravity field solutions, which is represented in Figure 2-2 [Barthelmes, 2013]. The geoid is an equipotential surface that meets the undisturbed surface of the ocean. An equipotential surface is not the surface where the magnitude of gravitational potential is constant. Instead, it means

that all the gravity vectors are orthogonal to the surface. The geoid height is often calculated to evaluate the accuracy of gravity solutions. The geoid height is the height between the geoid and the reference ellipsoid, where the reference ellipsoid is the fixed ellipsoid which best approximates the geoid. The geoid height, $N(\vartheta, \lambda)$, can be calculated by taking the difference between the gravitational potential of geoid and the reference ellipsoid, and then dividing the difference by $\frac{GM_{\oplus}}{R_{\oplus}^2}$. The equation for the geoid height [Barthelmes, 2013] is,

$$N(\vartheta, \lambda) = R_{\oplus} \sum_{n=0}^{\infty} \sum_{m=0}^n P_{nm}(\cos \vartheta) (C_{nm}^T \cos(m\lambda) + S_{nm}^T \sin(m\lambda)) \quad (2-5)$$

$$C_{nm}^T = C_{nm} - C_{nm}^U$$

$$S_{nm}^T = S_{nm} - S_{nm}^U.$$

The coefficients, C_{nm} and S_{nm} are of the geoid and C_{nm}^U and S_{nm}^U are coefficients of reference ellipsoid. Equation (2-5) shows that the geoid height can be computed for all ranges of colatitude and longitude once the spherical harmonic coefficients are computed.

For analyzing dynamic gravity field solutions, the geoid height variation must be calculated, which is similar to the geoid height calculation. Since the dynamic gravity field solution is defined by the magnitude of change from the static model, ΔC_{nm} and ΔS_{nm} represent dynamic solutions as defined in Equation (2-6) [Barthelmes, 2013].

$$\Delta N(\vartheta, \lambda) = R_{\oplus} \sum_{n=0}^{\infty} \sum_{m=0}^n P_{nm}(\cos \vartheta) (\Delta C_{nm} \cos(m\lambda) + \Delta S_{nm} \sin(m\lambda)) \quad (2-6)$$

$$\Delta C_{nm} = C_{nm}^{Total} - C_{nm}^{Static}$$

$$\Delta S_{nm} = S_{nm}^{Total} - S_{nm}^{Static}$$

Here, ΔN is the variation of the geoid height, which represents the geoid height change due to the dynamic solution.

Geoid height and geoid height variations are functions with respect to the colatitude and longitude. In addition to viewing the result in terms of colatitude and longitude, it is also required to view the result in terms of the degree of the coefficients. The geoid degree difference (GDD) can be calculated by taking the root sum square of the dynamic coefficients and multiplying by the radius of the Earth. The geoid degree difference (ΔN_n) provides the result in terms of length (distance) and the equation is provided below [Kim, 2000].

$$\Delta N_n = R_{\oplus} \sqrt{\sum_{m=0}^n (\Delta C_{nm})^2 + (\Delta S_{nm})^2} \quad (2-7)$$

Change in surface mass density and equivalent water height (EWH) are also often used to represent the solutions of the gravity field. The change in surface mass density ($\Delta \alpha(\vartheta, \lambda)$) shows how much the mass has changed over a specified surface area. Equation (2-8) provides the calculation of surface mass density [Wahr et al., 1998].

$$\Delta \alpha(\vartheta, \lambda) = \frac{R_{\oplus} \rho_{ave}}{3} \sum_{n=0}^{\infty} \sum_{m=0}^n \frac{2n+1}{1+k_n} P_{nm}(\cos \vartheta) (\Delta C_{nm} \cos(m\lambda) + \Delta S_{nm} \sin(m\lambda)) \quad (2-8)$$

Here, ρ_{ave} is the average density of the earth and k_n is a load Love number of degree n , which is a defined constant. From here, EWH ($\Delta \beta(\vartheta, \lambda)$) can be simply calculated by dividing the change in surface mass density by density of water (ρ_w) as in Equation 2-9 [Wahr et al., 1998].

$$\Delta\beta(\vartheta, \lambda) = \frac{\Delta\alpha(\vartheta, \lambda)}{\rho_w} \quad (2-9)$$

EWH shows how much the mass has changed in units of water height variations. This computed EWH is usually presented by a color map of the Earth, which directly helps us to visualize the gravity field solution. The same EWH can also be converted to a numerical result by taking the root mean square of the EWH over the entire, or specific area, of the map. However, this is not equally weighted RMS. At high latitudes, surface area of a grid is smaller compared to surface area of a grid at low latitudes. Therefore, when spatial RMS is computed, the appropriate weights must be given according to the surface area of that grid.

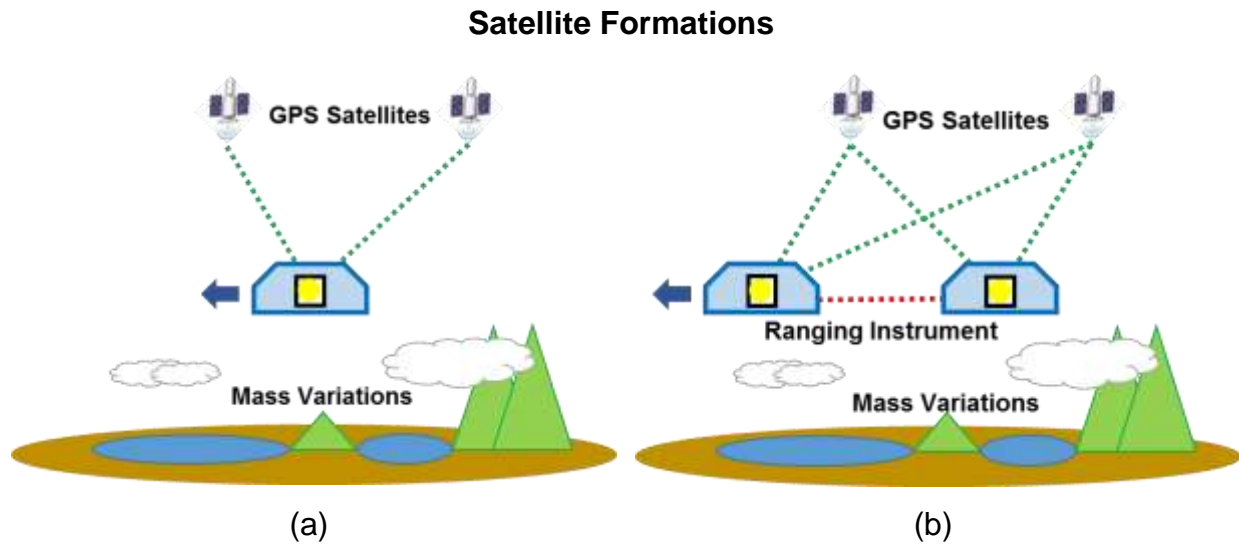


Figure 2-3. (a) High-low satellite-to-satellite tracking and (b) Low-low satellite-to-satellite tracking.

There are different types of satellite formations considered to be used in satellite geodesy. These formations are all based on the continuous tracking system involving GPS satellites. GPS is the most accurate tracking system that exists and provides absolute position measurements. As seen in Figure 2-3, a single satellite using GPS

tracking is called high-low satellite-to-satellite tracking (HL-SST). Low-low satellite-to-satellite tracking (LL-SST) requires additional satellite as seen from Figure 2-3. LL-SST continuously measures the range between the two satellites. This relative position measurement is more precise than the GPS absolute position measurement accuracy. Moreover, the range measurement also provides essential information related to the gravity field of the Earth, since the range is directly affected by the mass variations.

Singe Pair LL-SST

There are numerous types of LL-SST system configurations. One of the important fact about one-pair LL-SST systems is that for any configuration, the satellites must fly in a polar orbit in order to get full coverage of the Earth. The three most common configurations are in-line, pendulum and cartwheel as shown in Figure 2-4 [Elsaka et al., 2013]. The in-line configuration is a satellite pair following one after another, in the same orbit such that the range between the two satellites varies only along the flight direction of the satellites. The GRACE mission uses this in-line configuration. A big disadvantage of the in-line configuration is the lack of East-West sensitivity, which causes error stripes when viewed on the surface of the Earth. Therefore, to overcome this issue, the pendulum configuration was introduced. As seen from the figure, both the pendulum and the cartwheel configurations use two different orbits for each satellite. In the case of the pendulum configuration, the orbit for the following satellite is shifted by the right ascension of the ascending node (RAAN) angle from the orbit of the leading satellite. This pendulum configuration measures the range such that the range measurements are sensitive to both East-West and North-South directions. The cartwheel configuration has two satellites flying in different orbits but

with the same inclination and RAAN angles, such that their flight direction has less effect on the range of the satellites.

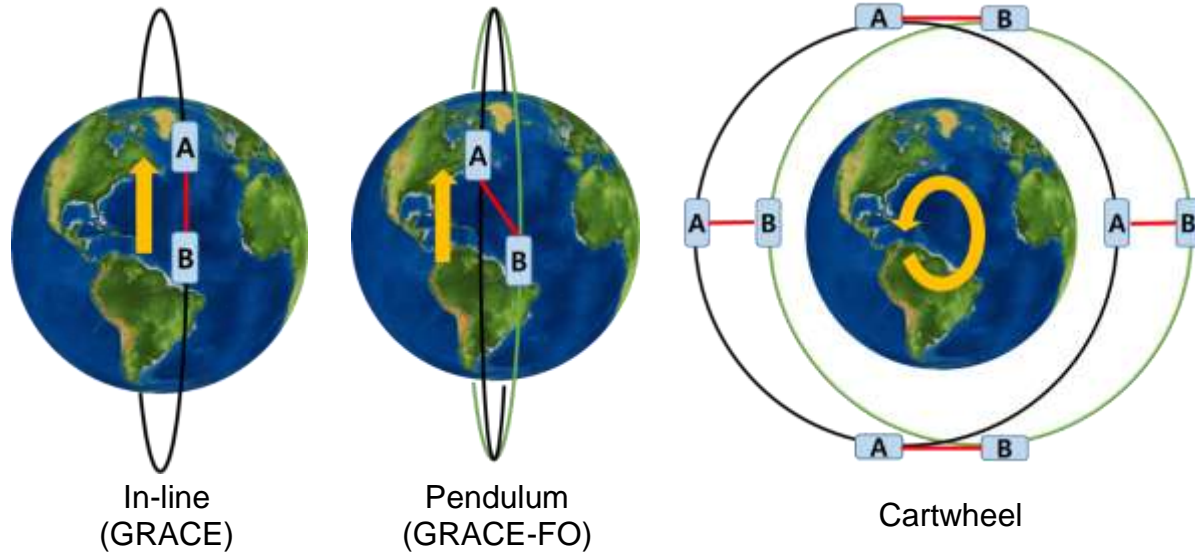


Figure 2-4. Single pair LL-SST configurations [Elsaka et al., 2013].

Double Pair LL-SST

As was introduced earlier, it is likely that future geodesy missions will use two pairs of satellites in an LL-SST configuration. This will increase the sampling frequency such that the aliasing error will be reduced. Also, by using two pairs of satellites, the coverage of the Earth can be completed more thoroughly or in less time, eventually opening the possibility of improving the time and spatial resolutions. Similar to the single pair case, there are numerous double pair LL-SST system configurations, and the most common configurations are shown in Figure 2-5 [Wiese et al., 2012; Elsaka et al., 2013; Elsaka et al., 2014]. Three of these configurations are based on the in-line configuration. Wiese (2012) applied a Monte-Carlo analysis to find the optimal orbit for the second pair of satellites which covered all of the different double in-line configurations. The in-line ΔM configuration is when the two pairs are in the same orbit

but separated from each other by different mean anomaly. Similarly, the in-line $\Delta\Omega$ configuration has two pairs in different orbits that are separated by different RAAN angles. The in-line Bender configuration has an inclined orbit for the second pair along with the polar pair. Lastly, the advanced pendulum configuration is similar to a single pair pendulum configuration but uses pairs of single pair pendulums across from each other as shown from the figure.

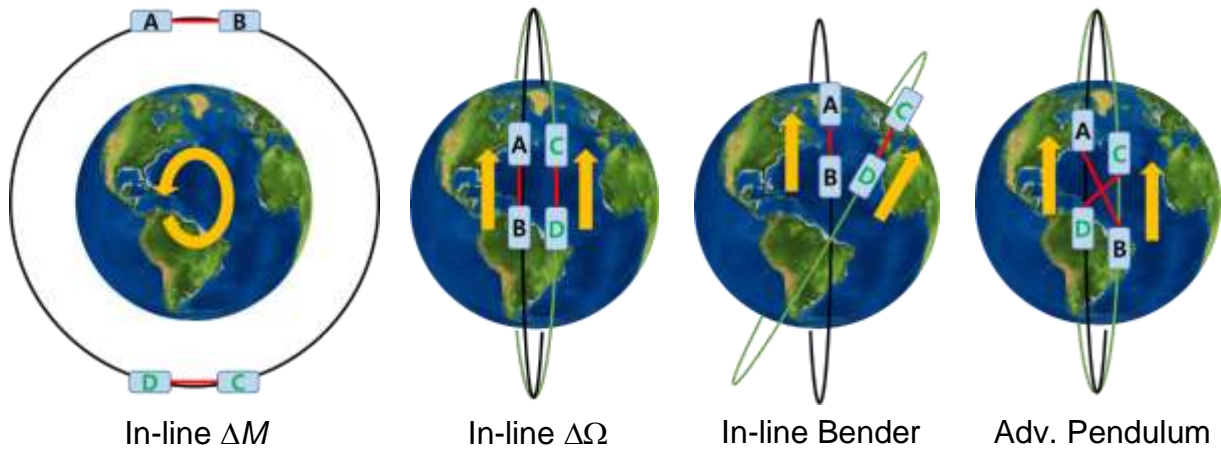


Figure 2-5. Double pair LL-SST configurations [Wiese *et al.*, 2012; Elsaka *et al.*, 2013; Elsaka *et al.*, 2014].

Optimal Configurations

A simulation study was done by Elsaka (2013) to find which of these configurations brings the most accurate solution. It was found that the pendulum configuration is the optimal configuration for a single pair LL-SST. However, a Monte-Carlo analysis must be done for this configuration to find the optimal orbits, similar to how the in-line Bender configuration was optimized by Wiese (2012). For the double pair LL-SST, the in-line Bender configuration was found to be the configuration that results in the least error in the solution.

Although the pendulum configuration was more suitable than the in-line configuration for a single pair LL-SST, this dissertation research used the in-line configuration. First of all, finding the optimal configuration is out of the scope of this research. Second, this work also uses the in-line Bender configuration for the two-pair LL-SST. Therefore, the in-line inclined pair can be added to the in-line polar pair, greatly simplifying the computation. Lastly, in-line configuration is the only configuration tested configuration by the GRACE mission and this research desires to show the effects on the solutions for missions similar to GRACE.

Drag-free Systems

Drag-free systems [*DeBra et al.*, 2011] offer the most promising technique for reducing acceleration noise below the level of accelerometers by eliminating the noisy electrostatic suspension forces applied to the test masses. A micro-propulsion system is used to keep the host satellite centered with respect to its test mass so that the test mass and spacecraft follow a near-perfect gravitational orbit. An example of drag-free system is shown in Figure 2-6 [*Nguyen*, 2016]. The test mass is shielded by a housing from non-gravitational forces and thrusters or a suspension system keeps the test mass centered. A drift mode accelerometer is a new hybrid technology that reduces the acceleration noise by cycling the electrostatic suspension system and uses a laser interferometer to measure the satellite's non-gravitational acceleration without the need for external propulsion or drag-free control [*Conklin*, 2015]. Drag-free technology was used by the Gravity Field and Steady-State Ocean Circulation Explorer (GOCE) (2009 ~ 2013) to reduce the test mass suspension forces required by the mission's electrostatic gravity gradiometer. Since GOCE's drag-free system directly cancels the perturbing effects of atmospheric drag, it was able to fly at a low altitude of about 250 km. The

measured acceleration noise of the drag-free GOCE mission was two orders of magnitude smaller than that of GRACE's electrostatic accelerometers [Touboul *et al.*, 2012]. Advanced drag-free systems with accuracies even better than that of GOCE have been developed for future gravitational wave observatories [Dolesi *et al.*, 2003]. One such system is being tested in 2016 by the LISA Pathfinder mission [Armano *et al.*, 2015]. The first results of the LISA Pathfinder mission showed that the measured acceleration noise was more accurate than the acceleration noise requirement [Armano *et al.*, 2016]. Drag-free small satellite platforms are also being examined, which may reduce the cost of this technology and make multiple satellite pairs more feasible [Nguyen *et al.*, 2015]. In the future, drag-free low-low satellite-to-satellite missions could improve time-varying gravity field estimates beyond those provided by GRACE and GRACE-FO. Consequently, it is important to explore the effects of different drag-free systems on the gravity field solutions to determine the acceleration noise level that is optimal with regard to both performance and cost.

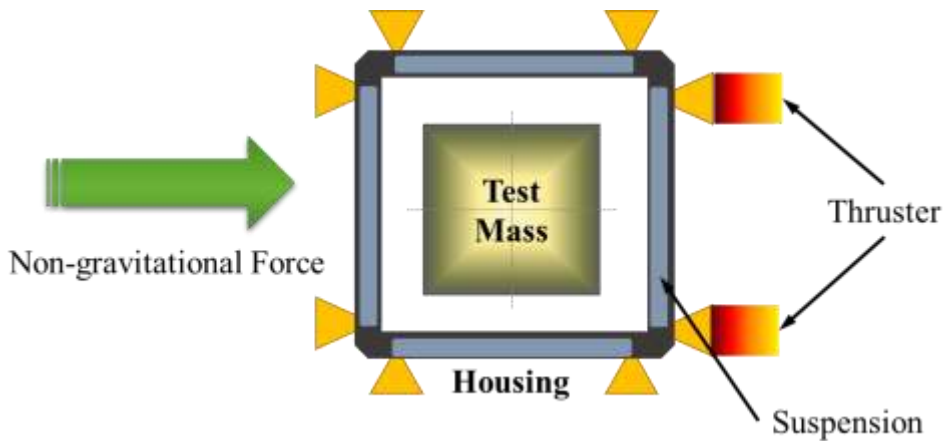


Figure 2-6. Drag-free system [Nguyen, 2016].

Major Source of Errors

There are three major sources of error in gravity field recovery: (1) device measurement noise, (2) temporal aliasing error, and (3) non-gravitational forces. For LL-SST systems, device measurement noise comes from measuring the position and the range of the satellite pair. The GPS tracking of CHAMP, GRACE and GOCE had $1 \text{ cmHz}^{-1/2}$ orbit determination accuracy. The K-Band Microwave Ranging (KBR) system in GRACE had about $1 \mu\text{mHz}^{-1/2}$ range accuracy. The Laser Ranging Interferometer (LRI) is expected to perform with accuracy of about $80 \text{ nmHz}^{-1/2}$. All three numerical values are true for the frequencies between $1 \text{ mHz} \sim 10 \text{ mHz}$.

Temporal aliasing error is caused by under-sampling of an uncertain dynamic model. Since the mass of the Earth is always changing there is no way to avoid this error. There are four possible ways to decrease this error. The first way is to change the configurations of satellites from collinear shape (in-line) to other shapes in a way that it increases East-West sensitivity such as the cartwheel or the pendulum configurations as it was explained in the previous section. A second way is to develop more accurate nominal dynamic models (or a priori information), also known as de-aliasing models. A third way is to increase the sampling frequency by adding more pairs of satellites. There were several analyses including Wiese (2012) and Elsaka (2013), which showed a reduction in the aliasing error by adding another pair of satellites. The last way is to use numerical filters to smooth the solution, such as ‘Gaussian Smoothing’ by Swenson and Wahr (2002). In this dissertation, to decrease the temporal aliasing error, a second pair of satellites will be added and numerical filters will be used. De-aliasing models will also be used and both cases of using realistic and idealistic de-aliasing models are explored.

Developing more accurate de-aliasing models and searching for optimal configurations of satellites are out of the scope of this research.

Non-gravitational forces, also known as acceleration noise, affects the equation of motion of the satellites directly. Three major non-gravitational forces are solar radiation pressure, atmospheric drag and thrust forces. As was explained in earlier section, acceleration noise can be compensated for, by using electrostatic accelerometers or drag-free systems. Even after acceleration error is compensated, a residual noise of the drag-free system persists. This residual noise is caused by the position error of proof mass and noise from the actuators among other sources. Table 2-1 shows the noise levels for each existing drag-free technology.

Table 2-1. Technology and associated residual acceleration noise [Flury *et al.*, 2008; Touboul *et al.*, 2012; Antonucci *et al.*, 2012].

Technology	Residual Acceleration Noise $\text{ms}^{-2}\text{Hz}^{-1/2}$
Electrostatic Accelerometer	$\sim 10^{-9}$ (CHAMP, 2000) $\sim 10^{-10}$ (GRACE, 2002)
Gradiometer drag-free control	$\sim 2 \times 10^{-12}$ (GOCE, 2009)
True drag-free control	$\sim 3 \times 10^{-14}$ (LISA Pathfinder, 2015) <mission requirement>

CHAPTER 3

MISSION ARCHITECTURE

Before we begin the estimation, there are many parameters to decide. Mainly we must choose the orbits of the satellites. They must be chosen to match those considered in future missions. Therefore, previous missions and simulation studies are surveyed to choose such parameters. Also, technology for the mission must be chosen based on the latest existing ones with provided noise magnitudes. The mission design has been motivated throughout this chapter and the method of creating simulation noise will be introduced.

Orbit Selection

Due to GRACE's ability to effectively measure the time-varying gravity field, it is most likely that future Earth geodesy missions will continue to use the low-low satellite-to-satellite tracking approach. We therefore choose to use a measurement scheme similar to that of GRACE and to measure the satellites' orbits using GPS receivers. Since the microwave ranging system will soon be replaced by the LRI of GRACE-FO, we will also assume a satellite-to-satellite ranging system with a measurement noise equal to that expected for the LRI. Moreover, to focus on future missions, gravity field solutions of two pairs of satellites are considered together with the single pair solution to compare the effects of acceleration noise with different magnitudes of temporal aliasing error.

Orbit selection for two pairs of satellites must be chosen for the simulation. There have been simulation studies performed to determine the optimal orbits for two pairs of satellites in gravity field recovery [Wiese *et al.*, 2012]. It was concluded that the inclination angle is the most significant parameter that affects the gravity field solution.

According to this study, if the first pair of satellites is flying in a polar orbit, then the optimal orbit for the second pair is inclined at an angle of 72 degrees. This is based on the fact that both pairs are flying in near circular orbits (eccentricity of 0.001).

The optimal altitude (semi-major axis) is more difficult to choose since there is a tradeoff between mission lifetime and the spatial resolution. Lower altitudes exhibit higher atmospheric drag and therefore require greater fuel consumption to compensate for the drag. At the same time, lower altitudes enable measurements to be made closer to the Earth's surface, making them more sensitive to higher order spherical harmonics of the gravitational potential. Future Earth geodesy missions are likely to focus on spatial resolutions up to 100~200 km, because the needs of different science fields are concentrated in this region [Sneeuw *et al.*, 2005; Pail *et al.*, 2015]. An altitude of 350 km appears to be a good compromise between maximizing the lifetime of the mission and maximizing the resulting spatial resolution. At an altitude of 350 km, the lifetime of the satellites can be over 10 years with the same mass propellant fraction as GRACE [Wiese *et al.*, 2012].

Temporal resolution of GRACE-based gravity field models has been improved up to a single day using a Kalman filter approach, although this requires a priori information derived from geophysical models [Kurtenbach *et al.*, 2009]. Institutions responsible for GRACE solutions; Geo Forschungs Zentrum (GFZ) at Postdam Germany [Dahle, 2013], Center for Space Research (CSR) at Austin Texas [Bettadpur, 2012], and the Jet Propulsion Laboratory (JPL) at Pasadena California [Watkins and Yuan, 2012], compute monthly mass variations but with greater spatial resolution than the daily solutions. Considering the current state of gravity field solutions, it is plausible to think of time

resolutions shorter than one month since we are considering additional pair of satellites, and the science needs of most fields is focused on solutions with time resolutions of two weeks or longer [Sneeuw *et al.* 2005]. Hence, the time resolution (or repeat period) of the gravity field solution, which is equivalent to the accumulated data length used to recover the gravity model, is chosen to be two weeks (half a month) for this simulation.

Other orbital parameters such as Right Ascension of the Ascending Node (RAAN) and argument of perigee do not have much effect on the solution [Wiese *et al.*, 2012] and therefore they are chosen to be similar to those of the actual GRACE mission as seen from the Table 3-1.

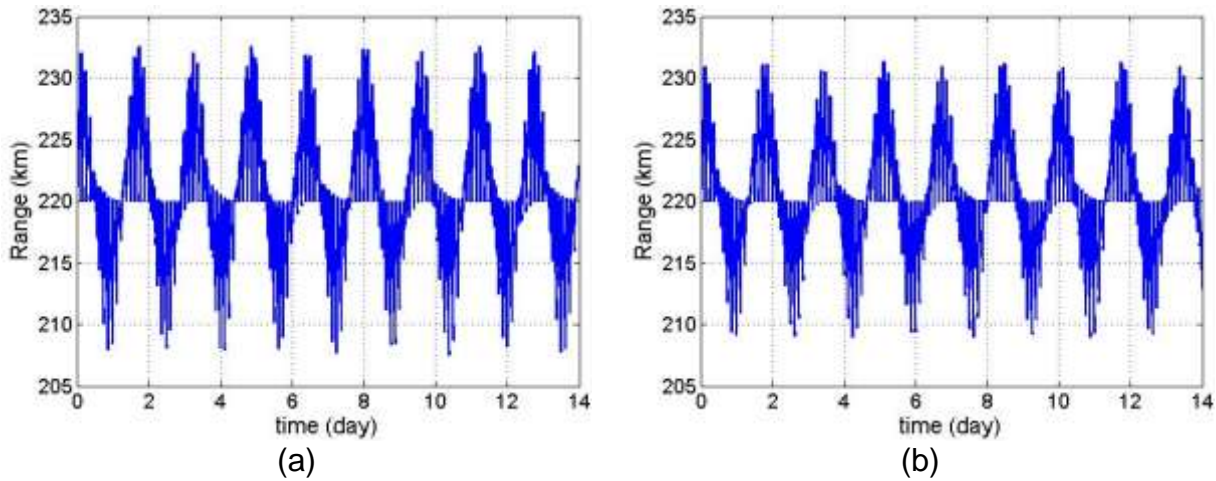


Figure 3-1. Separation distance between the leading and trailing satellites as a function of time for (a) the polar pair and (b) for the inclined pair.

The separation distance between the two satellites is another parameter that must be chosen. The two GRACE satellites are separated by a distance of 220 km on average. For this simulation work, we assume that the separation distance is periodically corrected to keep a separation distance of 220 km equivalent to GRACE. The separation distance of both pairs of satellites are shown in Figure 3-1. The graphs show the separation distance between polar and inclined pairs of simulation satellites

for the research, and the range varies from 210 km to 230 km. In average, the range variation is 16.7 m at frequency of 100 mHz and 729.1 m at frequency of 0.1 mHz.

Ground Track Patterns

It is important to make sure that the ground track patterns of satellites have the desired repeat period. This type of ground track is known as a repeating ground track [Wiese *et al.*, 2012]. This way the data will not have a bias towards any specific region of the Earth. Repeating ground tracks are defined by over the surface of the Earth inclination, eccentricity, and semi-major axis, as well as with the targeting repeat period in sidereal days, which is slightly shorter than the repeat period in calendar days. Vtipil and Newman (2012) discussed several methods to modify the ground tracks using the above parameters, and the method chosen for this analysis among the discussed methods is called the Flower Constellation. This is a simple method that considers only the Earth's mass and its oblateness (J_2 term) in a two-body (Earth and satellite) approximation. This method computes the semi-major axis, when the desired inclination, eccentricity and repeat period are provided. The semi-major axis can be computed by solving the following equation [Vtipil and Newman, 2012].

$$4\mu\phi a^2 y(a)^2 x(a) = [\omega_E^2 a^3 x(a)^4 - \phi a^2 x(a) - \mu y(a)^2]^2$$

$$\delta = \frac{3R_E^2 J_2}{4}$$

$$\tau = \frac{N_d}{N_p} \quad (3-1)$$

$$\beta = 2 - 3 \sin^2 i$$

$$\gamma = 4 - 5 \sin^2 i$$

$$\phi = \mu \tau^2 \delta^2 \beta^2$$

$$x(a) = 2a(R_E + h_p) - (R_E + h_p)^2$$

$$y(a) = \tau[x(a)^2 + \delta\gamma a^2] - 2\delta a^2 \cos i$$

Here, μ is the Earth's gravitational constant, a is the semi-major axis, i is the inclination angle, ω_E is the Earth's rotation, R_E is the Earth radius, J_2 is the second-order zonal effects, N_d is the number of sidereal days the Earth completes during the period of repetition, N_p is the number of revolutions along the orbit in one period of repetition, and h_p is the perigee height above Earth's surface. x and y are intermediate variables.

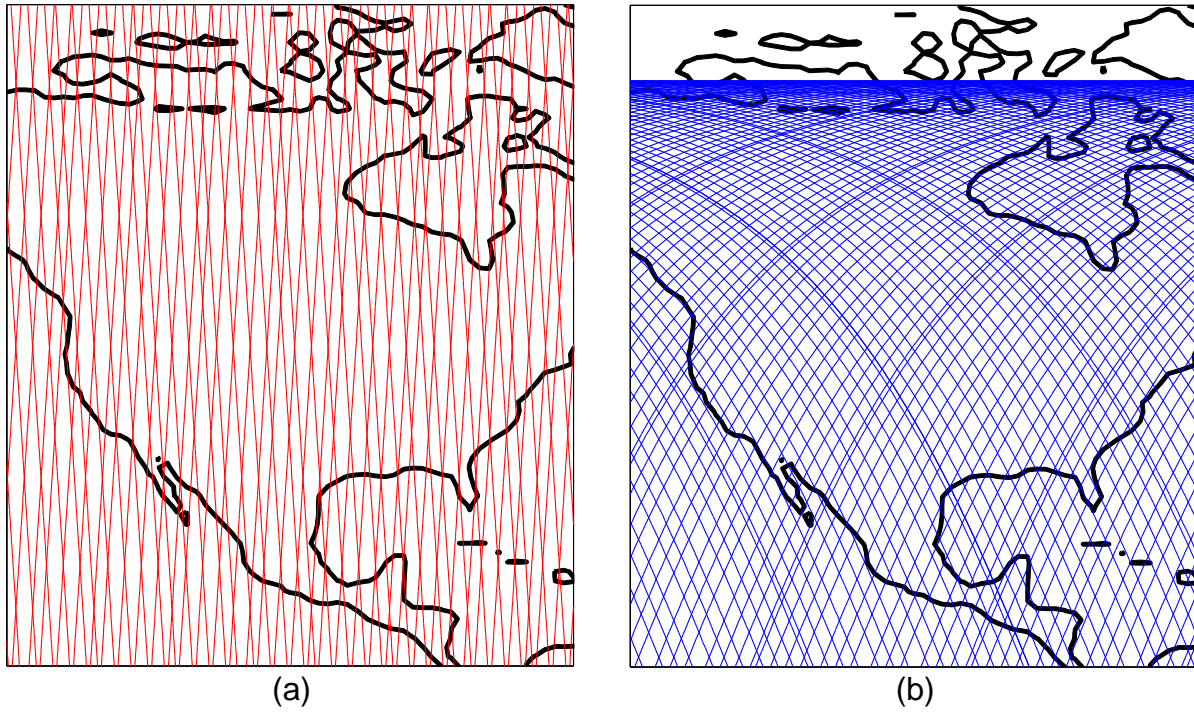


Figure 3-2. Ground tracks of (a) polar pair and (b) inclined pairs of satellites.

As seen from the Equation (3-1), this is a nonlinear problem. Therefore, an initial value for the semi-major axis is required. Appropriate values for inclination, eccentricity and repeat period are discussed in the previous section. The rest of the parameters are well known constants. Since this method is an approximation, the resulting semi-major axis might not provide the exact repeating ground track. The most accurate repeating

ground track was selected empirically by varying the semi-major axis, calculated using Equation (3-1), in increments of 2 km and actually computing the positions of satellite with full spherical harmonic coefficients. The ground track patterns found are shown in Figure 3-2, and from this figure, it can be seen that they have repeat periods close to 14 days. The final set of orbit parameters used in this analysis is summarized in Table 3-1, including the altitudes calculated by ground track adjustment.

It is worth noting that a Modified Flower Constellation method that considers the additional J_4 term, also exists [*Vtipil and Newman, 2012*]. However, this modified method is more complex in terms of computation and produces a semi-major axis that is only different by few meters compared to the result from the standard Flower Constellation method. Consequently, the modified approach was not used in this analysis.

Table 3-1. Summary of orbit parameters used for both the polar pair and inclined pair of satellites.

Parameters	Values
Semi-major Axis of Pair 1 (average altitude)	6734.58 km (356.45 km)
Semi-major Axis of Pair 2 (average altitude)	6732.69 km (354.56 km)
Eccentricity	0.001
Inclination of Pair 1	90°
Inclination of Pair 2	72°
Argument of Perigee	133°
Right Ascension of the Ascending Node (RAAN)	155.8°
Separation Distance	220 km
Repeat Period (Temporal Resolution)	14 days

Technology and Associated Noise

The analysis presented here assumes that state of the art measurement technologies will be used in future geodesy missions. Since this analysis is based on a simulation, appropriate noise models for each measurement technology are required. Table 3-2 lists the three measurements required for low-low satellite-to-satellite tracking missions and the technologies that are assumed for each measurement in the simulation. Attitude measurements and associated noise are neglected for this research.

Table 3-2. Measurement technologies used in this analysis.

Measurement	Technology
Satellite position	Global Positioning System (GPS)
Satellite-to-satellite range	Laser Ranging Interferometer (LRI)
Spacecraft non-gravitational acceleration	Drag-free System

Position and Range Noise Models

GPS is the most accurate continuous position tracking system available, and it is the most widely used technology to track positions of satellites. The orbit determination accuracy for CHAMP, GRACE and GOCE was computed to be close to 1 cm [Kang *et al.*, 2006]. Accordingly, we modeled GPS position measurement noise simply as white (Gaussian) noise with a standard deviation of 1 cm Hz^{-1/2}. This noise is added to the simulated spacecraft positions, to all three directions; along track, radial and cross track.

The microwave ranging system used in GRACE has an accuracy of ~5 μm Hz^{-1/2} for frequencies between 1 and 10 mHz [Sheard *et al.*, 2012]. The measurement noise of the LRI is expected to be ~80 nm Hz^{-1/2} for frequencies between 2 and 10 mHz [Heinzel

et al., 2012]. The official noise requirement which is used as the LRI noise in this simulation is shown in Table 3-3. As shown in Table 3-3, the model was assumed to be true for larger band of frequencies and also we are assuming that the LRI performance reaches its requirement. The method used to generate colored noise will be discussed in the following section.

Acceleration Noise Models

Table 3-3. LRI and Acceleration noise models used in this analysis.

Technology	Noise Accuracy ($0.1 \text{ mHz} < f < 100 \text{ mHz}$)
Laser Ranging Interferometer	$\sqrt{1 + \left(\frac{0.003}{f}\right)^2} \times \sqrt{1 + \left(\frac{0.01}{f}\right)^2} \times \frac{80 \text{ nm}}{\text{Hz}^{1/2}}$ $\left(1 + \frac{0.005}{f}\right)^{1/2} \times 10^{-10} \frac{\text{m/s}^2}{\text{Hz}^{1/2}}$
GRACE electrostatic accelerometer	(along track and radial directions) $\left(1 + \frac{0.1}{f}\right)^{1/2} \times 10^{-9} \frac{\text{m/s}^2}{\text{Hz}^{1/2}}$ (cross track direction)
GOCE drag-free system	$\left(1 + \frac{0.001}{f}\right)^{1/2} \times 2 \times 10^{-12} \frac{\text{m/s}^2}{\text{Hz}^{1/2}}$ (all directions)
LISA Pathfinder drag-free system	$\left(1 + \frac{0.001}{f}\right)^{1/2} \times 3 \times 10^{-14} \frac{\text{m/s}^2}{\text{Hz}^{1/2}}$ (all directions)

Two major non-gravitational forces acting on low Earth orbiting satellites are solar radiation pressure and atmospheric drag. These forces must be measured by accelerometers or directly compensated for with drag-free systems. When accelerometers are used, acceleration noise is caused by the uncertainties in measuring these non-gravitational forces acting on the spacecraft. However, when a drag-free system is employed, the acceleration noise is caused by residual forces acting on the test mass. This residual noise is caused by residual coupling to the relative

motion of the spacecraft and test mass (stiffness), by noise from the test mass actuators, and by temperature, pressure, and electric and magnetic field fluctuations. To examine the effects of different drag-free residual acceleration noise levels, we apply three spectra of acceleration noise, each representing a distinct, existing technology. The technologies evaluated are, the electrostatic accelerometer used in GRACE, the drag-free system used in GOCE, and the LISA Pathfinder drag-free system.

The noise levels used in the simulation for the electrostatic accelerometer [*Flury et al.*, 2008] and the two different drag-free systems [*Touboul et al.*, 2012; *Antonucci et al.*, 2012] are shown in the Table 3-3. The drag-free system with an acceleration noise equivalent to that of the GRACE electrostatic accelerometers, which has an accuracy of $10^{-9} \text{ ms}^{-2}\text{Hz}^{-1/2}$ in cross-track direction and $10^{-10} \text{ ms}^{-2}\text{Hz}^{-1/2}$ in along-track and radial directions, was applied in the simulation. The GOCE drag-free system was applied only on the along track direction. The acceleration measurement from GOCE had the accuracy of $2 \times 10^{-12} \text{ ms}^{-2}\text{Hz}^{-1/2}$ with a frequency bandwidth from 5 to 100 mHz [*Touboul et al.*, 2012]. However, the residual acceleration noise of the drag-free system was larger. Nevertheless for this simulation, the GOCE drag-free system was applied with the accuracy of acceleration measurement on all directions. For LISA Pathfinder drag-free system, a requirement for the noise magnitude was $3 \times 10^{-14} \text{ ms}^{-2}\text{Hz}^{-1/2}$ over a frequency range of 1 to 100 mHz [*Antonucci et al.*, 2012]. Although the actual residual acceleration noise was found to be smaller, this noise level requirement was used in the simulation. Since the noise spectra is not provided for other frequencies, it was assumed for both drag-free systems that the noise magnitude slightly increases for frequencies less than 1 mHz. For each simulation, we considered a frequency band that

ranges from 0.1 to 100 mHz. The lower bound limited by the size of the data segments and the higher bound is set by the sampling rate. All the acceleration noise models used in this simulation are shown in Table 3-3.

Generating Colored Noise

Most measurement noise spectra can be modeled as $\frac{1}{f^\alpha}$, where $0 \leq \alpha \leq 2$. GPS, LRI, and accelerometer noises can be modeled accurately with linear combinations of such curves. Kasdin (1995) and Stoyanov (2011) have provided useful methods to create colored noise of the form $\frac{1}{f^\alpha}$. This method is described by Equations (3-2) through (3-3) [Kasdin, 1995; Stoyanov et al., 2011].

$$\xi(x; \omega) = \int_0^x h(x-y)w(y; \omega)dy \quad (3-2)$$

$$\begin{aligned} \xi_i(\omega) &= \sum_{k=0}^i h_{i-k} w_k(\omega) \text{ for } i = 0, \dots, \infty \\ h_0 &= 1 \end{aligned} \quad (3-3)$$

$$h_k = (\frac{\alpha}{2} + k - 1) \frac{h_{k-1}}{k}$$

Here, $h(x)$ is the impulse response function, $w(y; \omega)$ is the white noise random field, $\xi(x; \omega)$ is the resulting random field, $x, y \in \mathbb{R}$ are continuous independent variables, and ω is the frequency.

Equation (3-3) is the discrete form of Equation (3-2), which is the discrete convolution. The discrete convolution can be easily computed by taking the fast Fourier transform (FFT), multiplying the impulse response function and the white noise random field in the frequency domain, and finally transferring the product back to the time domain using the inverse fast Fourier transform (IFFT). The simulated noises using this approach and the associated models for the LRI and drag-free systems are shown in

Figure 3-3. We tried to make the noise that accurately represents the model using the method explained in this section. However, there are some discrepancies especially at low frequencies for the LRI noise, where the slope is $\frac{1}{f^2}$. The generated LRI noise is about one order of magnitude smaller than the provided model at low frequencies.

Summary of the Simulation Design

There have been developments in various technologies and methods that were mentioned above. Since the main objective of this research is to explore the effects of different acceleration noise levels and hence find the optimal acceleration noise level for future LL-SST geodesy missions, it is required to set other technologies in the simulation as the most appropriate ones. Furthermore, the optimal orbit and configuration must be chosen to reduce the error as much as possible. GPS is the most accurate continuous position tracking system available and this was used in recent missions such as GRACE and GOCE. For range measurements, the microwave ranging system was used in GRACE. However, the laser ranging interferometer (LRI) known to be more accurate and soon will be tested in GRACE-FO. In order to reduce the temporal aliasing error, additional in-line pair will be simulated in an in-line Bender configuration and be compared with a single in-line pair. Also, both realistic and idealistic de-aliasing models will be used to explore the effects of acceleration noise for both cases. A drag-free system was used in GOCE but it had only 1 degree of freedom (DOF). This simulation will consider 3-DOF drag-free systems with different levels of acceleration noise. Table 3-4 summarizes the simulation design with respect to the error sources and launched satellite geodesy missions.

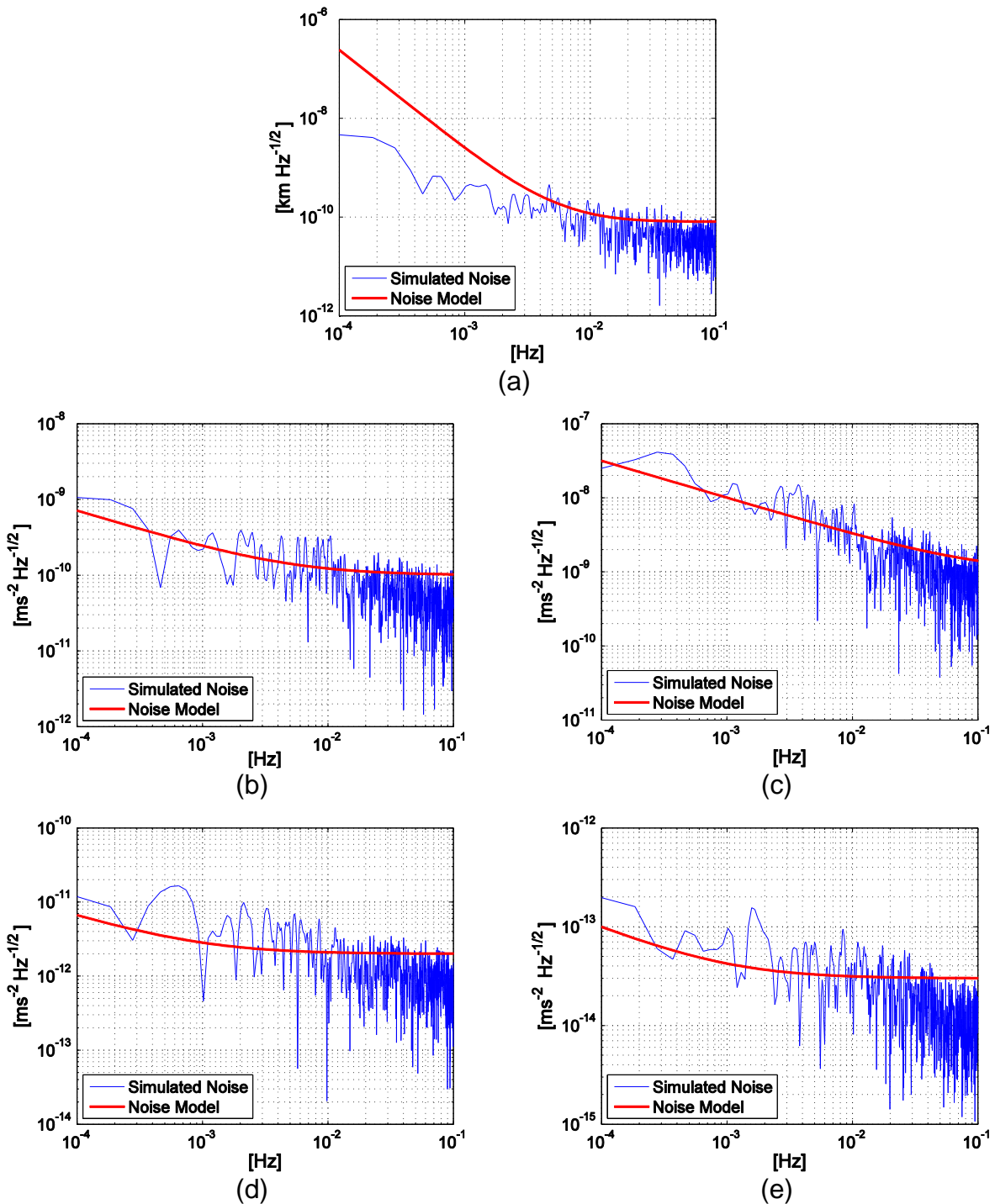


Figure 3-3. The noise model and numerically generated noise for (a) LRI, (b) GRACE along track and radial acceleration noise, (c) GRACE cross track acceleration noise, (d) GOCE acceleration noise, and (e) LISA Pathfinder acceleration noise.

Table 3-4. Summary of simulation design with respect to error sources and launched missions.

Error Source	Launched Missions	Simulation
Device measurement	<ul style="list-style-type: none"> · GPS · K-Band Ranging 	<ul style="list-style-type: none"> · GPS · LRI
Temporal aliasing	<ul style="list-style-type: none"> · In-line configuration · Realistic de-aliasing model 	<ul style="list-style-type: none"> · In-line & in-line Bender configurations · Realistic & idealistic de-aliasing models
Acceleration	<ul style="list-style-type: none"> · Electrostatic accelerometer · Drag-free system (1-DOF) 	<ul style="list-style-type: none"> · Drag-free system (3-DOF)

CHAPTER 4

ESTIMATION AND SIMULATION PROCEDURE

A toolbox to simulate satellite tracking for geodesy missions was created that can compute measurement data of the satellites, and also estimate the gravity field of the Earth using these measurements. We followed classical approaches that exist in several text books and journal articles that fit into our research environment. This kind of toolbox already exists in other institutions where they have been working on satellite geodesy for decades. However, to understand the full view of this field, and also to bring unique research in the future, this toolbox was created. Gravity models used in this simulation are explained. The methods of creating data and the estimation process are presented throughout the chapter.

Gravity Model Selection

Since this analysis is based on simulation rather than actual mission data, we must generate “truth data” that resembles the data we expect to measure in a future mission. Nominal data is also required, which is the initial approximation of the actual data based on a priori information, which also serve as de-aliasing models. As mentioned earlier, both static and dynamic gravity field solutions exist. Typically, five independent dynamic models comprise the major sources of mass variations of the Earth. They are the ocean tide, ocean, atmosphere, hydrology and ice models. Ocean tide is the ocean variation mainly caused by the Moon and the Sun. The ocean and atmosphere models represent mass variations of the ocean and atmosphere respectively. Hydrology and ice models refer to the water variations over the land that include soil moisture, groundwater, rivers, reservoirs, snow, etc.

Fortunately, there are several different sources for each of the five dynamic gravity field models, some of which are generated by independent research groups. This allows us to use one such source as the true model and another for the nominal model. The models chosen to create true and nominal data are shown in Table 4-1.

Table 4-1. Static and dynamic gravity models used in this analysis.

		True-A	True-B	Nominal
Dynamic	Static	EIGEN-5C	EIGEN-5C	EIGEN-5C
	Ocean Tide	EOT11a	FES2004	FES2004
	Ocean	AOD1B-05 (OMCT)	AOD1B-01 (PPHA)	AOD1B-01 (PPHA)
	Atmosphere	AOD1B-05 (ECMWF)	AOD1B-01 (ECMWF)	AOD1B-01 (ECMWF)
	Hydrology	Updated ESA	Updated ESA	None
	Ice	Updated ESA	Updated ESA	None

The static gravity field model, EIGEN-5C is produced by Geo Forschungs Zentrum at Potsdam (GFZ) in 2008 [Foerste et al., 2008], and EIGEN-5C is derived from a combination of GRACE and LAGEOS mission data with 0.5×0.5 deg gravimetry and altimetry surface data [Foerste et al., 2008]. The ocean tide model EOT11a is derived from an empirical harmonic analysis based on multi-mission satellite altimetry data and published by Technische Universität München (TUM) [Savcenko and Bosch, 2012; Rieser et al., 2012], and FES2004 is derived by a modeling approach based on hydrodynamic and assimilation models and published by French Tidal Group (FTG) [Lyard et al., 2006]. The atmosphere and ocean de-aliasing product AOD1B is used for the GRACE data analysis. This model consists of the gravity variations over six hour

periods in atmosphere and ocean with respect to the mean gravitational field. The AOD1B Release 1 product (AOD1B-01) used the ocean model called Pacanowski, Ponte, Hirose and Ali (PPHA) to obtain the ocean variations and European Center for Medium-range Weather Forecast (ECMWF) to obtain the atmosphere variations [Flechtner, 2007]. The AOD1B Release 5 product (AOD1B-05) used the ocean model called Ocean Model for Circulation and Tides (OMCT) to obtain the ocean variations and ECMWF data to derive the atmosphere variations [Dobslaw et al., 2013; Flechtner et al., 2014]. Both AOD1B-01 and AOD1B-05 used ECMWF to obtain the atmosphere variations, but ECMWF was updated between the two releases and some unknown changes were made, resulting in different atmosphere models. The AOD1B-05 is the product of five generations of model improvements from the AOD1B-01. The AOD1B product is provided in spherical harmonic coefficients up to degree and order 100. Hydrology and Ice models are provided by the European Space Agency (ESA) [Gruber et al., 2011; Dobslaw et al., 2015]. They created their first version of simulated time-variable gravity field with a period of 6 hours that includes atmosphere, ocean, hydrology, ice and solid-earth components. This data is provided in spherical harmonic coefficients up to degree and order 180. In 2014, ESA generated an updated version of their time-variable gravity field models. The hydrology and ice models used were extracted from this updated ESA model.

We also use two sets of true models, denoted A and B. The True-A set represents the realistic case where we assume that de-aliasing models have the accuracy of existing products. The True-B set of models were used to generate measurements, assuming that the de-aliasing models are more accurate such that the

aliasing error is only caused by the dynamics of the hydrology and ice signals. The accuracy of these idealistic de-aliasing models is difficult to achieve in practice, but such models have continued to improve over the past several years. It is therefore enlightening to examine solutions where there are less aliasing errors caused by the inaccuracy of these de-aliasing products. Hydrology and ice models are not used as a part of the de-aliasing product, because this research evaluates the accuracy in estimating the true hydrology and ice signals and we want to remove any bias that comes from pre-knowledge of the solution.

Creating Measurement Data

There are six orbital elements; semi-major axis, eccentricity, mean anomaly, RAAN, inclination and argument of perigee. These orbital elements are chosen according to the mission architecture from Chapter 3 and they can be used to compute the initial position and velocity vectors. Therefore, starting from this initial position and velocity, satellite measurements can be obtained.

First, acceleration caused by the gravitational field of the Earth can be computed for given position and velocity vectors by applying the following equations [Montenbruck and Gill, 2005].

$$\begin{aligned}
 \ddot{x} &= \sum_{n,m} \ddot{x}_{nm}, \quad \ddot{y} = \sum_{n,m} \ddot{y}_{nm}, \quad \ddot{z} = \sum_{n,m} \ddot{z}_{nm} \\
 \ddot{x}_{nm} &= \frac{GM}{R_\oplus^2} \left\{ -C_{n0} V_{n+1,1} \right\}, \text{ for } (m=0) \\
 \ddot{x}_{nm} &= \frac{GM}{R_\oplus^2} \frac{1}{2} \left\{ \left(-C_{nm} V_{n+1,m+1} - S_{nm} W_{n+1,m+1} \right) + \frac{(n-m+2)!}{(n-m)!} \left(C_{nm} V_{n+1,m-1} + \right. \right. \\
 &\quad \left. \left. S_{nm} W_{n+1,m-1} \right) \right\} \\
 \ddot{y}_{nm} &= \frac{GM}{R_\oplus^2} \left\{ -C_{n0} W_{n+1,1} \right\}, \text{ for } (m=0)
 \end{aligned} \tag{4-1}$$

$$\ddot{y}_{nm} = \frac{GM}{R_{\oplus}^2} \frac{1}{2} \left\{ \left(-C_{nm} W_{n+1,m+1} + S_{nm} V_{n+1,m+1} \right) + \frac{(n-m+2)!}{(n-m)!} \left(-C_{nm} V_{n+1,m-1} + S_{nm} W_{n+1,m-1} \right) \right\}$$

$$\ddot{z}_{nm} = \frac{GM}{R_{\oplus}^2} \left\{ (n-m+1) (-C_{nm} V_{n+1,m} - S_{nm} W_{n+1,m}) \right\}$$

$$V_{mm} = (2m-1) \left\{ \frac{x R_{\oplus}}{r^2} V_{m-1,m-1} - \frac{y R_{\oplus}}{r^2} W_{m-1,m-1} \right\}$$

$$V_{nm} = \left(\frac{2n-1}{n-m} \right) \frac{z R_{\oplus}}{r^2} V_{n-1,m} - \left(\frac{n+m-1}{n-m} \right) \frac{R_{\oplus}^2}{r^2} V_{n-2,m}$$

$$W_{mm} = (2m-1) \left\{ \frac{x R_{\oplus}}{r^2} W_{m-1,m-1} - \frac{y R_{\oplus}}{r^2} V_{m-1,m-1} \right\}$$

$$W_{nm} = \left(\frac{2n-1}{n-m} \right) \frac{z R_{\oplus}}{r^2} W_{n-1,m} - \left(\frac{n+m-1}{n-m} \right) \frac{R_{\oplus}^2}{r^2} W_{n-2,m}$$

$$V_{00} = \frac{R_{\oplus}}{r}, W_{00} = 0$$

Once the acceleration is computed, this acceleration is integrated using Runga-Kutta 4th order (RK4) method to compute the position and velocity vectors of the next epoch. This procedure is repeated until all the measurements are computed.

Estimation Method

The most standard estimation technique to apply is the best linear unbiased estimator (BLUE) which, uses equations equivalent to the weighted least squares estimation. However, considering the size of the data and the estimating parameters, it is not possible to perform the estimation with a single block of data and Jacobian (transformation) matrix. This would require a large amount of RAM space and will require a long computation time. Accordingly, the partitioned BLUE is a viable candidate. Using the partitioned BLUE, we can avoid the lengthy computation of large matrices by simply dividing the data and Jacobian matrices into smaller blocks, and

parallel computing the estimation process using these smaller blocks. This reduces, not just the computation time for the estimation, but also the computation time needed to create Jacobian matrices. For this simulation, each block was chosen to span 3 hours of data. In other words, the arc length was chosen to be 3 hours. Different institutions depending on their estimation method use various arc lengths. JPL, CSR and GFZ institutions use daily arc lengths. We decided to use a shorter arc length because, we estimate fewer parameters compared to the institutions mentioned above. We have reduced the arc length up to the point where the data size for each arc still exceeds the number of parameters and still allows the satellites to complete more than one orbit so that this will not affect the low degree coefficients.

There are two types of measurement data as discussed from previous section, inter-satellite range and position. The sampling time is chosen to be 10 seconds, which provides a valid frequency for recovering the solution given the desired spatial resolution. During each time step, seven measurements are made, denoted as vector $c(t)$.

$$c(t) = \begin{bmatrix} \rho(t) \\ x_1(t) \\ y_1(t) \\ z_1(t) \\ x_2(t) \\ y_2(t) \\ z_2(t) \end{bmatrix} \quad (4-2)$$

Here, $\rho(t)$ is the inter-satellite range, and $(x_1(t), y_1(t), z_1(t))$ and $(x_2(t), y_2(t), z_2(t))$ are the positions of the following and the leading satellites respectively. The interferometer only measures the relative range, so GPS data must be used to provide absolute positions of the satellites. As mentioned above, the measurement data is divided into 3-

hour arcs (batches). This leads to 112 batches of data for the entire 14-day repeat period. The measurement equation is shown in Equation (4-3).

$$c = A\Phi\Theta_0 + \epsilon \quad (4-3)$$

$$\Theta = \begin{bmatrix} u \\ p \end{bmatrix}$$

Here, c is the measurement data vector, A is the Jacobian (state-to-measurement transformation matrix), Θ_0 is the state vector (estimating parameters) at the initial epoch t_0 . The variable u represents the initial state of the satellites and p represents the spherical harmonic coefficients. The state transition matrix is Φ , which converts the static state vector at epoch t_0 to the current time t . Lastly, ϵ is the measurement noise vector. These equations show that even though the gravity field is time-varying, we are estimating the best average approximation over a given 14-day period.

The variational equations are used to create the state transition matrix. This method is highly computational but it is known to be straight forward and accurate. The general form of the variational equations are as follows [Montenbruck and Gill, 2005].

$$\Phi(t, t_0) = \begin{bmatrix} \Phi_u(t, t_0) & S(t) & 0 \\ 0 & I & 0 \\ 0 & 0 & I \end{bmatrix}$$

$$\Phi_u = \begin{pmatrix} \Phi_r \\ \Phi_v \end{pmatrix} = \begin{pmatrix} \frac{\partial r(t)}{\partial(r(t_0), v(t_0))} \\ \frac{\partial v(t)}{\partial(r(t_0), v(t_0))} \end{pmatrix} \quad (4-4)$$

$$S = \begin{pmatrix} S_r \\ S_v \end{pmatrix} = \begin{pmatrix} \frac{\partial r(t)}{\partial p} \\ \frac{\partial v(t)}{\partial p} \end{pmatrix}$$

$$\frac{d}{dt}(\Phi_u, S) = \begin{pmatrix} 0_{3 \times 3} & I_{3 \times 3} \\ \frac{\partial a}{\partial r} & \frac{\partial a}{\partial v} \end{pmatrix} (\Phi_u, S) + \begin{pmatrix} 0_{3 \times 6} & 0_{3 \times n_p} \\ 0_{3 \times 6} & \frac{\partial a}{\partial p} \end{pmatrix} \quad (4-5)$$

Here, I is the identity matrix, r , v , and α are the position, velocity and total acceleration of the satellite respectively, and n_p is the number of spherical harmonic coefficients.

Subscript u refers to the portion of the state transition matrix associated with position and velocity. We let $H = A\Phi$, and since the problem is nonlinear, we solve it using the Gauss-Newton method. The estimation equation then becomes

$$c - c_{ref} = H(\Theta - \Theta_0) + \epsilon \quad (4-6)$$

or more compactly,

$$\Delta c = H\Delta\Theta + \epsilon$$

$$\begin{bmatrix} \Delta c_1 \\ \Delta c_2 \\ \vdots \\ \Delta c_n \end{bmatrix} = \begin{bmatrix} H_1 \\ H_2 \\ \vdots \\ H_n \end{bmatrix} \Delta\Theta + \begin{bmatrix} \epsilon_1 \\ \epsilon_2 \\ \vdots \\ \epsilon_n \end{bmatrix}. \quad (4-7)$$

Here, c_{ref} represents the measurements created by a priori information and $n = 112$ for 14 days of analysis.

The measurement noise model is provided by the GPS and LRI instrument performance given in previous sections. The measurement noise covariance matrix used in the estimation process was computed based on these noise models. On the other hand, the non-gravitational acceleration of the spacecraft is not measured directly by drag-free satellites. Instead, disturbance accelerations are compensated by thrusters that keep the position of the spacecraft centered with respect to a proof mass. Therefore, the acceleration noise is not a measurement noise for drag-free systems. This is in contrast to GRACE or GOCE where the spacecraft acceleration is measured by the on-board accelerometers where acceleration noise was measurement noise. In addition to measurement noise, the estimation process also uses state noise to account for the uncertainty of the state equation. For GRACE and GOCE data analysis,

empirical or geophysical models were used to estimate the state noise [*Kurtenbach et al.*, 2009]. In this analysis, an appropriate uncorrelated state noise covariance matrix, P_v , was computed by first averaging the nominal set of dynamic models from Table 4-1 for a time span of two weeks and then scaling this value empirically, such that the estimation process was stable. All parameters were given the same weights to avoid any bias. The term $\Delta\tilde{\Theta}$, which is the initial guess of the parameters, also known as a priori information, is set equal to zero for all arcs. Now Equation (4-7) can be modified as follows,

$$\begin{bmatrix} \Delta\tilde{\Theta} \\ \Delta c \end{bmatrix} = \begin{bmatrix} I \\ H \end{bmatrix} \Delta\Theta + \begin{bmatrix} v \\ \epsilon \end{bmatrix} \quad (4-8)$$

Here, $\Delta\tilde{\Theta}$ is a priori information of the parameter vector with the state noise v .

Creating the measurement covariance matrix, P_ϵ , that accurately represent the measurement variation is challenging due to the noise correlation. Two approaches were considered to compute these covariance matrices. The first was to choose a white noise covariance that bounds the appropriate colored noise. The second was to use a filter to convert a white noise covariance into the appropriate colored noise covariance. Adding a filter will produce more accurate estimates and the resulting posteriori statistical error will be more representative of the true estimation error [*Petovello et al.*, 2008]. On the other hand, a filter will require extra computations. Since this will increase the computation time and cost, a bounding white noise covariance was used. A filter is considered in later chapter of this dissertation.

Equations (4-9) and (4-10) are the BLUE solutions with a priori information. They are equivalent, but Equation (4-10) is used to perform the estimation.

$$\Delta\widehat{\Theta} = (P_v^{-1} + H^T P_\epsilon^{-1} H)^{-1} (P_v^{-1} \Delta\widetilde{\Theta} + H^T P_\epsilon^{-1} \Delta c) \quad (4-9)$$

$$\Delta\widehat{\Theta} = (\begin{bmatrix} F \\ EH \end{bmatrix}^T \begin{bmatrix} F \\ EH \end{bmatrix})^{-1} (\begin{bmatrix} F \\ EH \end{bmatrix}^T \begin{bmatrix} F\Delta\widetilde{\Theta} \\ E\Delta c \end{bmatrix})$$

$$P_v^{-1} = F^T F \quad (4-10)$$

$$P_\epsilon^{-1} = E^T E$$

From this point, the best linear unbiased estimation can be performed simply by using each set of matrices to perform the estimation and then combining the result using the posterior covariance matrices and estimates to compute the final solution. In this combining process, it was assumed that the each estimates are correlated only for one day period. This is to mimic the daily solutions computed by the other groups as mentioned above. Ideally, this result is equivalent to performing a single best linear unbiased estimation using the whole concatenated matrices.

There were two different ways applied to compute the BLUE. First is the well-known QR factorization method. Second is the preconditioned conjugate gradient (PCCG) method introduced by Klees (2003). Equation (4-11) presents QR factorization, where Q is the orthonormal matrix and R is the upper triangular matrix.

$$\tilde{H}_{i \times j} = Q_{i \times i} \begin{bmatrix} R_{j \times j} \\ 0_{(i-j) \times j} \end{bmatrix} \quad (4-11)$$

$$\tilde{H} = \begin{bmatrix} F \\ EH \end{bmatrix}$$

When QR factorization is applied to BLUE, the estimation equation reduces to as follows.

$$\Delta\widehat{\Theta} = R^{-1} b$$

$$\begin{bmatrix} b_{j \times 1} \\ r_{(i-j) \times i} \end{bmatrix} = Q^T \begin{bmatrix} F\Delta\widetilde{\Theta} \\ E\Delta c \end{bmatrix} \quad (4-12)$$

The advantage of QR factorization is that the complexity of computation reduces dramatically and since R is an upper triangular matrix, taking an inverse is avoided. Another big advantage is that the size of matrix reduces from number of rows to columns. In most cases, there are more rows than columns, meaning that there are more observations than the parameters need to be estimated. Reducing the matrix size is essential when dealing with a large amount of data.

The PCCG method is an iterative process which is presented below with series of equations [Klees et al., 2003].

$$r_0 = H^T P_\epsilon^{-1} \Delta c$$

$$w_0 = N_{pre}^{-1} r_0$$

$$\rho_0 = r_0^T w_0$$

$$d_0 = w_0$$

For $i = 0, 1, 2, \dots$ until $r_i^T r_i < \epsilon$

$$q_i = H^T P_\epsilon^{-1} H d_i \quad (4-13)$$

$$\alpha_i = \frac{\rho_i}{d_i^T \cdot q_i}$$

$$x_{i+1} = x_i + \alpha_i d_i$$

$$r_{i+1} = r_i - \alpha_i q_i$$

$$w_{i+1} = N_{pre}^{-1} r_{i+1}$$

$$\rho_{i+1} = r_{i+1}^T \cdot w_{i+1}$$

$$d_{i+1} = w_{i+1} + \frac{\rho_{i+1}}{\rho_i} d_i$$

Here, N_{pre} is an approximation of the matrix $H^T P_\epsilon^{-1} H$. This iterative process is truncated while $r_i^T r_i < \epsilon$ and ϵ is chosen empirically. A big advantage of PCCG over QR factorization is that it uses less RAM space since all the terms being iterated are vectors, not matrices. Large data computation such as gravity field estimation, requires a lot of RAM space, so PCCG becomes a very efficient method.

The two different approaches produced equivalent results with similar computation time. However, we chose to use, QR factorization since it is easier to implement and modify. Also, since the computation was not limited by the RAM space there was no need for the use of the PCCG method. This does not mean that the PCCG method is less efficient than QR factorization. The number of iterations we chose empirically took same time as the QR factorization method, but there is a possibility that PCCG can be more time efficient with the same accuracy if it were tuned properly.

Simulation Procedure

The entire simulation procedure is shown in Figure 4-1. There are four parts in this simulation work. The first part creates the measurement data using true set of gravity models. There are seven parameters to generate, the inter-satellite range and the positions of two satellites. These measurement data can be computed simply by integrating the equation of motion of pure drag-free satellites and adding GPS, LRI and acceleration noise as explained thoroughly in previous sections. This part must be computed in a sequence, but it does not require a lot of memory. The second part of the simulation is creating the transformation matrices and reference measurements using nominal gravity models. The reference data is created in a same manner as the measurement data. However, computing transformation matrices requires a lot of

memory and takes long time, requiring as many CPUs as available. Fortunately, this part can be computed in parallel and therefore, the University of Florida HiPerGator supercomputer was used to implement this part. Third part of the simulation is the estimation. The BLUE is applied to find the gravity solution. Daily solutions were computed first, and then these daily solutions were used to estimate the final biweekly solution. There are two parts to the estimated solution. One is the orbital elements, which is equivalent to the initial positions and velocities of satellites. Another is the spherical harmonic coefficients, which represents the size of the gravitational potential. In total, 120,960 observation sets were used to estimate 3,729 parameters. Finally, the last part is to evaluate the solution using techniques brought up in Chapter 2.

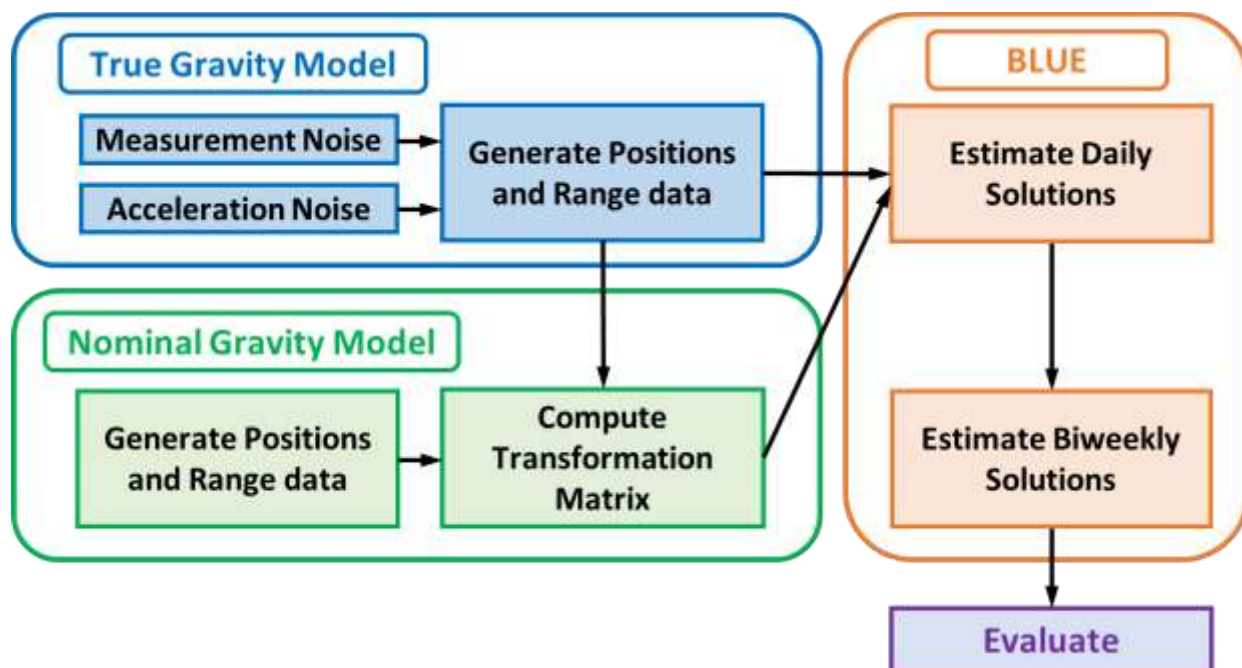


Figure 4-1. Block diagram of the simulation procedure.

CHAPTER 5 RESULT AND ANALYSIS

Representation of Solutions

The solutions were estimated in terms of spherical harmonics up to degree and order 60 using the steps provided in the previous section. The most common way to show such results is by plotting the geoid degree difference (GDD) error and the equivalent water height (EWH). The GDD error is the empirical error between the true and estimated coefficients. It is the root sum square of the difference with respect to each degree of coefficients, such that it shows the error of the result in terms of geoid height for every degree of the spherical harmonic coefficients [Wiese, 2011]. Equivalent water height is a physical quantity that shows the mass variations over the entire globe in terms of water height difference [Wahr et al., 1998]. Spatial root mean square (RMS) error of the EWH solution can also be calculated by subtracting true EWH from the estimated EWH, and then taking the root mean square of the entire set with appropriate weights based on the surface area of each grid. For all solutions, a numerical filter called, ‘Gaussian Smoothing’ (GS) by Swenson and Wahr (2002), was applied with radius of 300 km or less (depending on the solutions), to remove the aliasing error in the spherical harmonic coefficient estimates. Both non-filtered and filtered results are presented throughout the section.

Gravity field solutions were computed for the low-low satellite-to-satellite tracking system for three different cases. Case 1, 2, and 3 refers to GRACE, GOCE and LISA Pathfinder residual acceleration noise levels respectively, which is shown in Figure 3-3 and Table 3-3. As described in Table 4-1, there are two different sets of true models, A and B, to apply different levels of aliasing errors. From this point we will present results

using two different sets of true models for all three cases mentioned above and denote them as (A1, A2, A3) and (B1, B2, B3), where A and B refer to the different sets of true models and 1, 2, and 3 refer to different acceleration noise levels.

Geoid Degree Difference Error

Figure 5-1 shows the errors in geoid degree difference for Cases A1, A2 and A3. The true signal in Figure 5-1 is the true hydrology and ice mass variations converted to geoid height. Here, only hydrology and ice signals were drawn as the true signal since the goal of simulation is to recover hydrology and ice signals among all dynamic signals. As seen from this figure, all the estimated errors are below the true signal for the low degree coefficients. This is not a new finding, but it shows that the solutions from this simulation are reliable. We can see the increase in error towards the high degree coefficients, which is caused by various error sources including aliasing error, measurement noise and residual acceleration noise. By applying Gaussian smoothing (GS), this error can be reduced, resulting in more accurate solutions throughout the entire range of coefficients as shown by the dashed lines in the figure. A 300 km radius was applied to all single pair solutions. For two pair solutions, same 300 km radius was applied to Case A1, but both 200 and 300 km radii were applied to Cases A2 and A3 to find the radius that minimizes the error. GS between these two radii produced similar results, however 300 km radius had smaller error and so this radius was chosen. Applying the same GS radius for all three cases, allows us to compare the effects of GS. However, it is true that this radius does not provide best solutions for all cases.

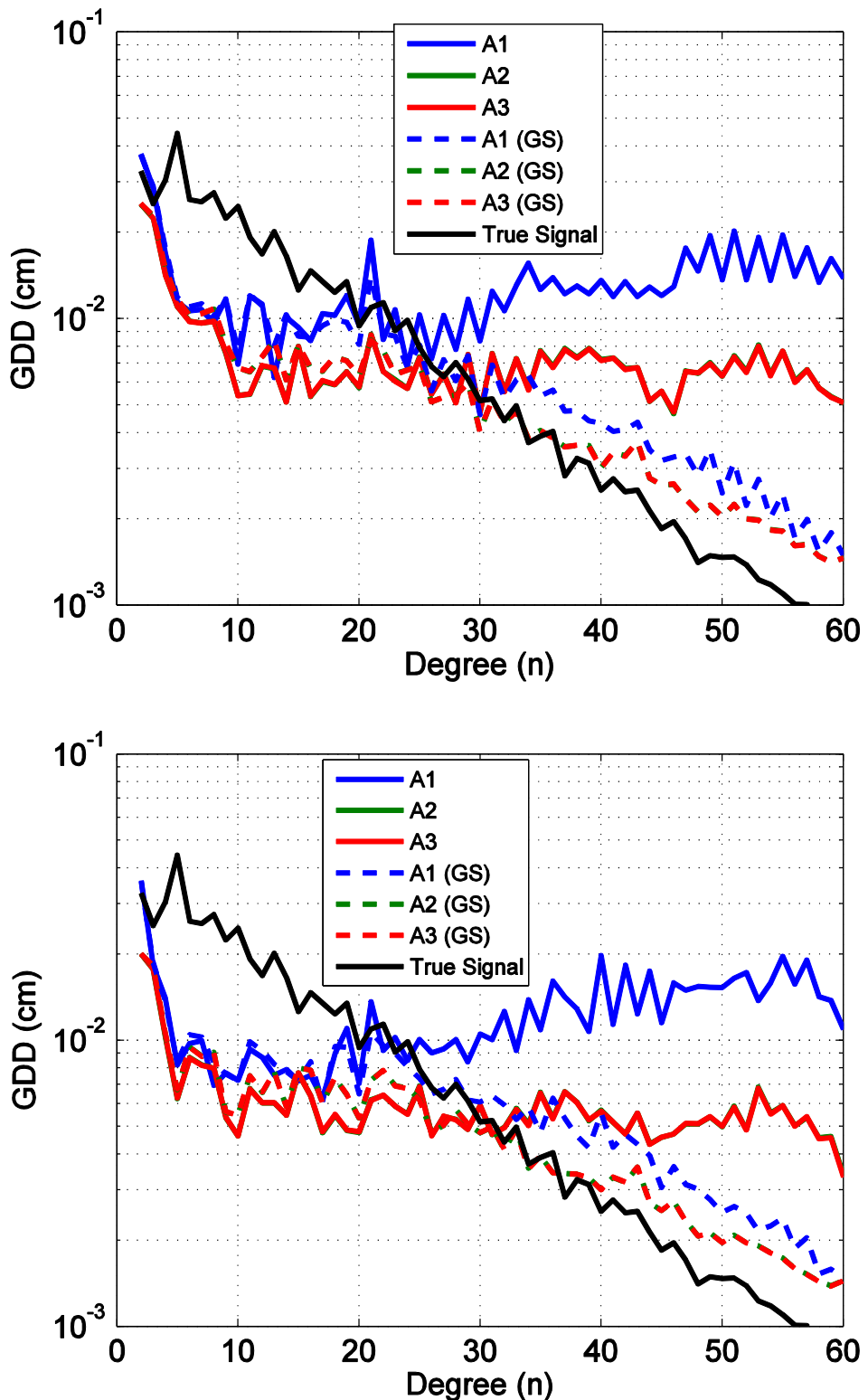


Figure 5-1. Errors and Gaussian smoothed (GS) errors expressed as GDD for one pair (top) and two pairs (bottom) using set 'A' true models.

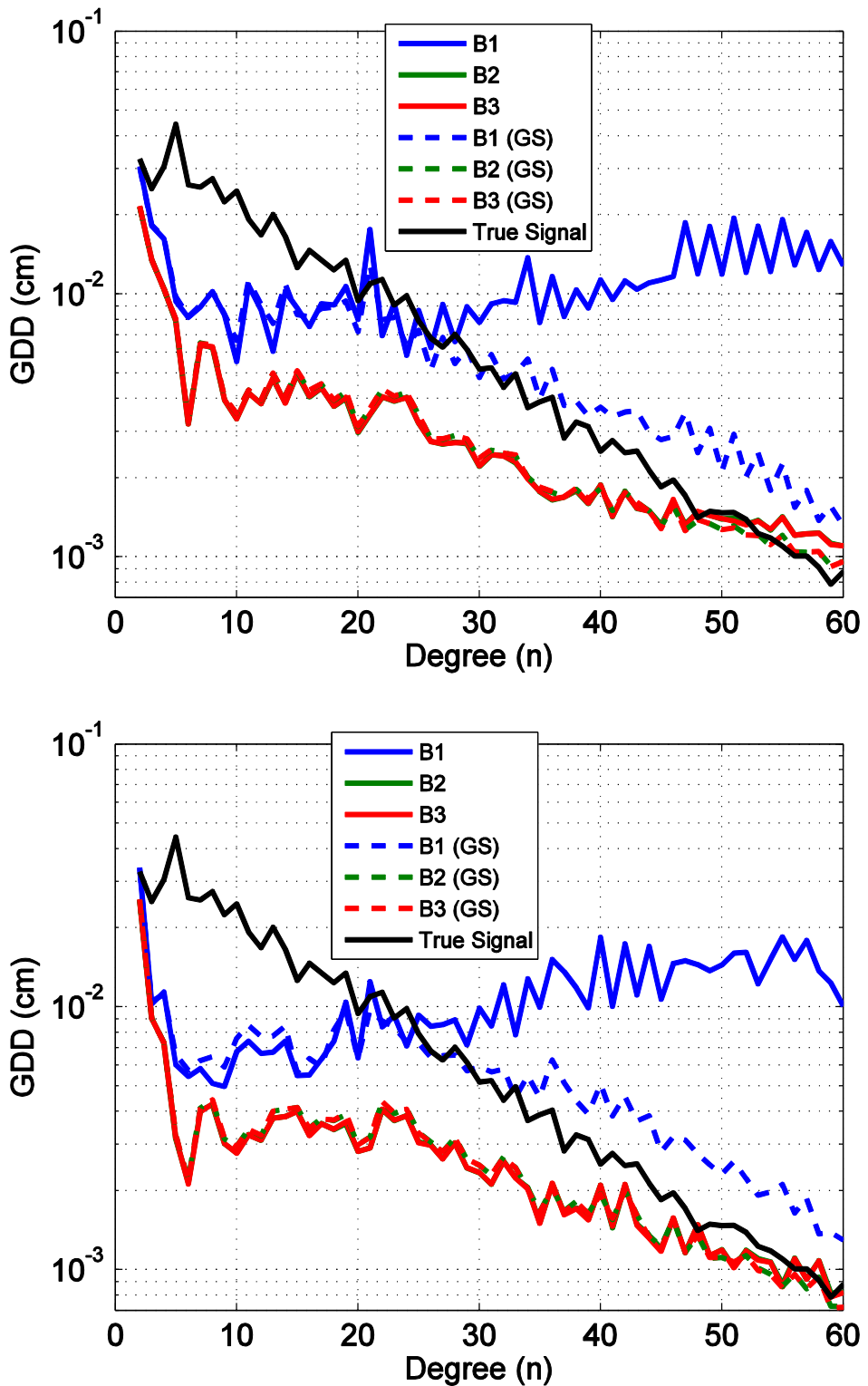


Figure 5-2. Errors and Gaussian smoothed (GS) errors expressed as GDD for one pair (top) and two pairs (bottom) using set 'B' true models.

From Figure 5-1, it can be seen that the high degree errors are greatly reduced when GS is applied. On the other hand, by applying GS, errors were increased for some low degrees. This is expected since GS removes some of the true signals along with the errors. Also, the solid curves for the single pair solutions on the left have greater magnitudes than the solid curves for the two pair solutions on the right. This indicates that adding a second pair of satellites reduces errors. In order to quantitatively determine the magnitude of the error reduction, the spatial RMS error is computed later in this chapter. Most importantly, Figure 5-1 shows that the error for Case A1 (GRACE acceleration noise), whether it is filtered or not, is always higher than the errors associated with the other two cases. This shows that by reducing the residual acceleration noise level from the GRACE to the GOCE level, the solution is improved. Moreover, Cases A2 and A3 (GOCE and LISA Pathfinder acceleration noise) solutions overlap almost exactly, indicating that there is not much improvement in the solution when the acceleration noise is reduced to below the GOCE level.

Figure 5-2 shows the estimation errors in terms of GDD for Cases B1, B2 and B3, as well as the true signal. The true signal in Figures 5-1 and 5-2 are the same, since the same hydrology and ice models are being estimated. Figure 5-2 shows the results of applying the idealistic de-aliasing models. By reducing the aliasing error with the idealistic de-aliasing models, the contributions of the aliasing error at different acceleration noise levels were revealed. Compared to Figure 5-1, Case B1 does not show an improvement, whereas the other two cases show a large reduction of the error. This means that at the GRACE acceleration noise level, reducing the aliasing error does not improve the solution, indicating that the acceleration noise is dominating. On the

other hand, at the GOCE acceleration noise level, applying idealistic de-aliasing models removes a significant amount of the error. This reveals that at GOCE acceleration noise level, the aliasing error is one of the dominating error sources. When acceleration noise is further reduced to the LISA Pathfinder level, the solution did not show significant improvement. This means that the Case B3 solution is limited by either the measurement noise from LRI and GPS tracking or the aliasing error caused by the hydrology and ice signals. Gaussian Smoothing with a 300 km radius was applied for Case B1. For Cases B2 and B3, a 100 km radius was applied since the estimated results seem to have very small errors based on the fact that the estimated signal is only slightly above the true signal beyond degree 50. In other words, GS was almost unnecessary, since the error curves were below the true signal for most of the degree range. Figure 5-2 also shows that when the in-line Bender configuration was applied, the solutions were improved for all three cases. This further reduction of the aliasing error does not change the general conclusion that was drawn for a single pair of satellites. Even when an additional pair of satellites and idealistic de-aliasing models were used to reduce the aliasing error, acceleration noise is still not a dominating source of error at GOCE acceleration noise level or below.

Equivalent Water Height

The geoid degree difference error (or geoid height error) shows the global result in a single one-dimensional curve, and therefore it is difficult to draw a complete conclusion from it. To obtain a deeper insight into the estimation errors, we visualize the solution by drawing global equivalent water height (EWH) maps. The EWH graphs for the solutions discussed above are shown in Figures 5-3 and 5-5. Table 5-1 shows the

respective spatial root mean square error of the EWH, which we use to quantify the magnitude of the error reduction.

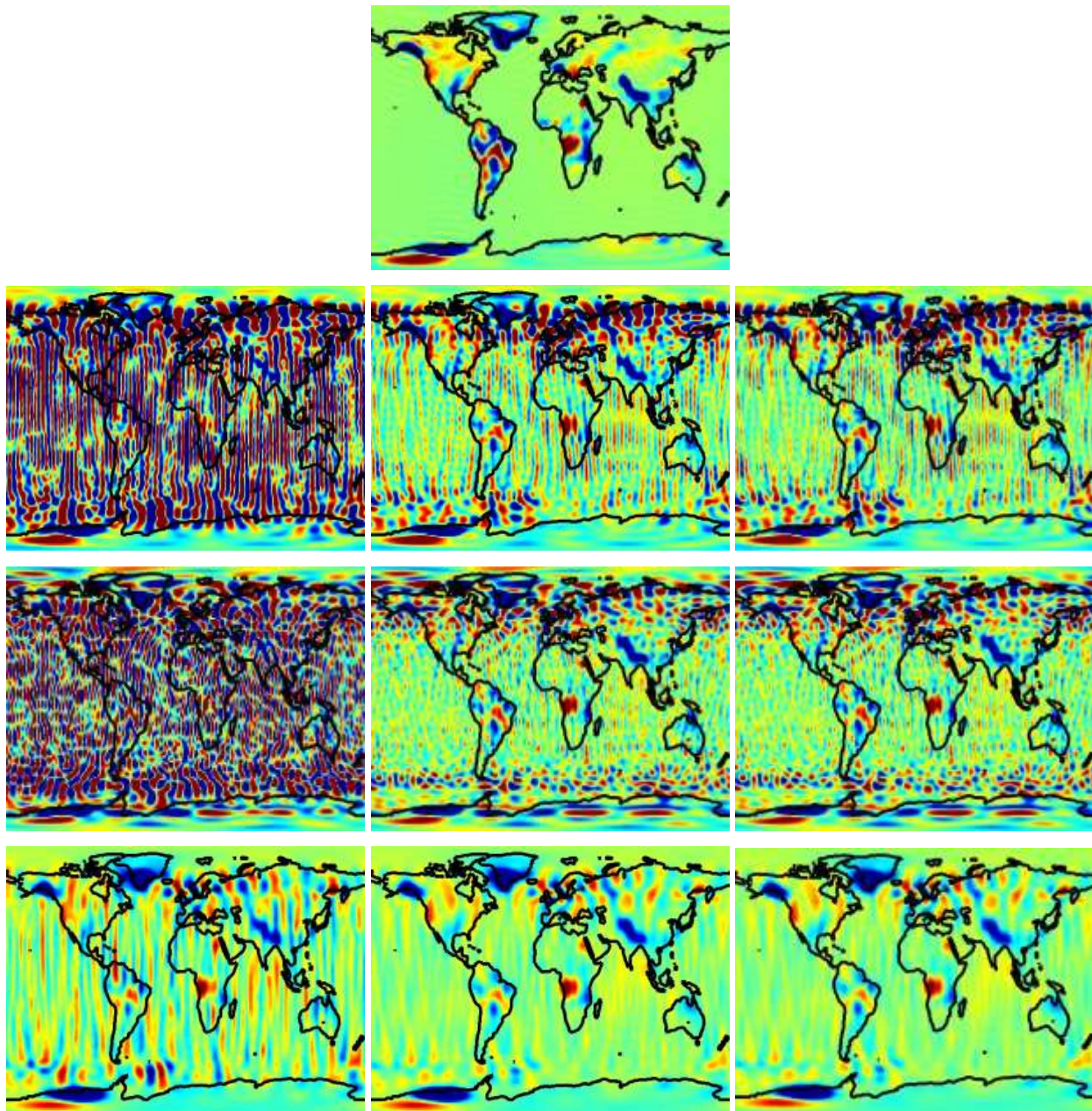


Figure 5-3. Estimated solutions using the set 'A' true models. True signal (row 1), single pair solution (row 2), double pair solution (row 3), single pair solution with GS (row 4) and double pair solution with GS (row 5). From row 2 to row 5, Case A1 (left), Case A2 (center) and Case A3 (right). Units are in cm of EWH and the figure includes hydrology and ice mass variations.

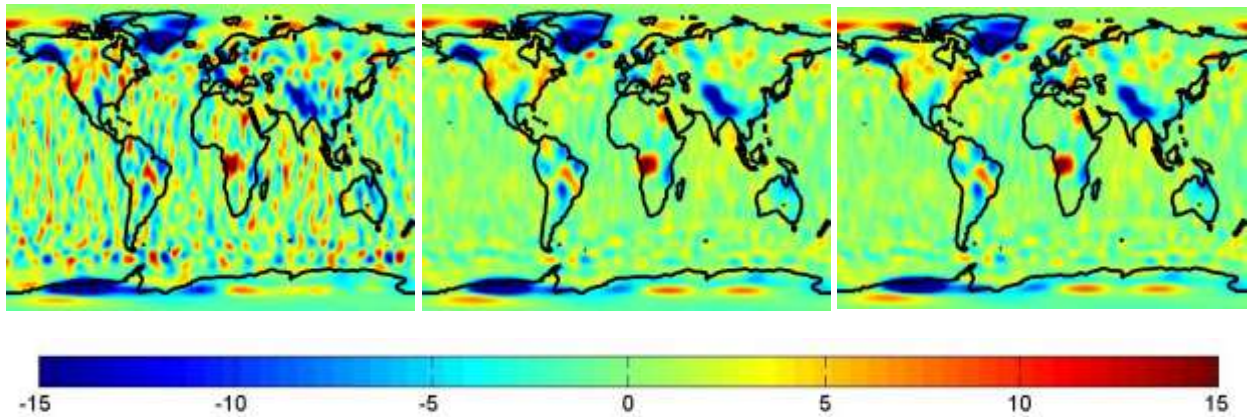


Figure 5-3. Continued.

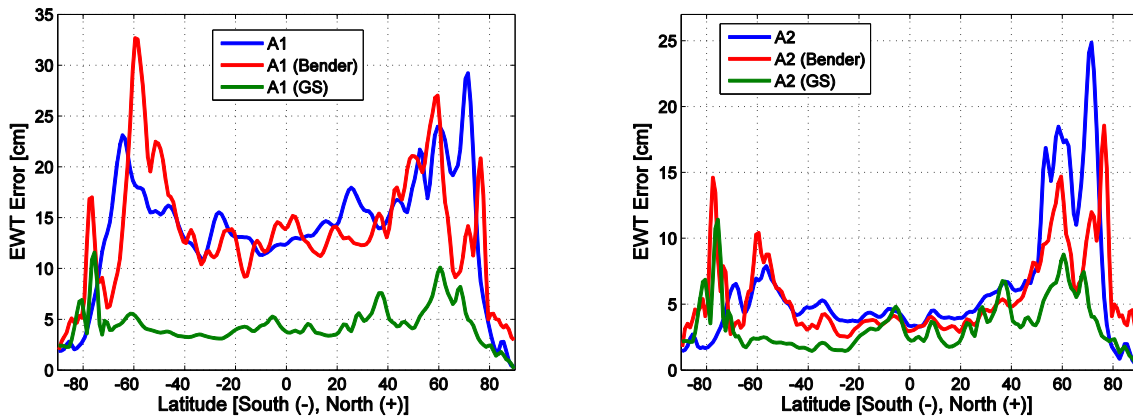


Figure 5-4. EWH error versus latitude plots; Case A1 on left and Case A2 on right.

Figure 5-3 shows the EWH solutions using the set 'A' true models, which include Cases A1, A2 and A3. These color-maps are drawn with a range of ± 15 cm. Row 1 is the true hydrology and ice mass variation in terms of EWH. The goal of the estimation process is to recover these signals with minimum error. Rows 2 through 5 in Figure 5-3 have three columns each. Left, center, and right each refers to Cases A1, A2 and A3 respectively. Row 2 is the estimated solutions for a single pair of satellites and row 3 shows the solutions for two pairs. Row 4 shows the GS-applied result for a single pair of satellites and row 5 shows the GS-applied result for two pairs. Both single and double pair solutions for Case A1 show discrepancies compared to the solutions for the other

two cases. The solutions for Cases A2 and A3 are almost identical even when a second pair of satellites is used. This result remains true even after applying GS. When compared with the true data (Row 1), we see that true signals are recovered for all cases. However, for Case A1, errors mask most of the true signal. The recovered signals become more pronounced and much of the aliasing error stripes are removed when an additional pair of satellites is used. However, this addition increases the errors at very high latitudes (both North and South) for all cases, which is shown by the red and blue regions in Figure 5-3. To show this affect more clearly in Figure 5-4 we plot the average EWH errors versus latitude for Cases A1 and A2. Case A3 is omitted because this result is almost identical to Case A2. From the figure, for both cases, when latitudes are greater than 70, the error increased when the second pair of satellites were added. This is because the inclined pair does not cover the high latitudes. Nonetheless, for most other latitudes, the error decreases when applying the Bender formation, because these latitudes are covered by both pairs of satellites. In addition, Figure 5-4 shows that the effects of GS are greater for Case A1 compared to other two cases even when the same radius is used. Overall, with these EWH results, we are able to observe the amount of error reduction when the acceleration noise is reduced from the GRACE (Case A1) to the GOCE (Case A2) level. Moreover, the solution with LISA Pathfinder (Case A3) noise, did not show further reduction of the error anywhere in the map.

There is one additional comment on GS. Rows 4 and 5 of Figure 5-3 show that GS eliminates most of the errors although it also diminishes the actual signal. For example, in the center of Greenland, there is an increase in the EWH (red color) over a relatively small area. This signal was recovered in the unfiltered solutions, but it was

removed when GS is applied, because of averaging with the nearby surface. This shows that there is a tradeoff between reducing the aliasing errors and reducing the true signals when applying Gaussian Smoothing. This tradeoff motivated the use of the in-line Bender formation and idealistic de-aliasing models in this study. They allow the influence of acceleration noise on the solution to be clearly observed without needing to use GS, which reduces the true signal.

Similar to Figure 5-3, Figure 5-5 shows the EWH solutions but using set 'B' true models, which are Cases B1, B2 and B3. The arrangement of Figure 5-5 is the same as that of Figure 5-3. Compared to set 'A' solutions, the overall results using set 'B' true models appear to be more accurate (less discrepancies compared to the true EWH), which is expected since there are less errors caused by the imperfection of de-aliasing models. However, Case B1 and Case A1 results appear to be very similar, indicating that the solution did not improve by applying idealistic de-aliasing models at GRACE acceleration noise level. On the other hand, the solutions for Cases B2 and B3 improved compared to Cases A2 and A3 where realistic de-aliasing models were applied. This implies that for acceleration noise levels smaller than that of GOCE, the acceleration noise is not a dominating source of error, but the aliasing error is at least one of the dominating sources. As with the results using the set 'A' true models, applying the in-line Bender formation improved all the solutions. However, this improvement is seemingly negligible for Cases B2 and B3, because the single pair solutions exhibit very little errors. Spatial RMS EWH errors can be computed to see if this is actually true. Similar to Figure 5-4, Figure 5-6 shows the average EWH errors for Cases B1 and B2 versus latitude. Case B3 is omitted for the same reason as that for

Case A3. Applying the Bender formation again increased the error at high latitudes (70 or above) but decreased the error at mid-low latitudes. Also according to the same figure, GS generally improved the solution for Case B1 but not for Case B2, because some of the true signals were filtered. However, this may not be a good comparison since different radii were used when applying GS.

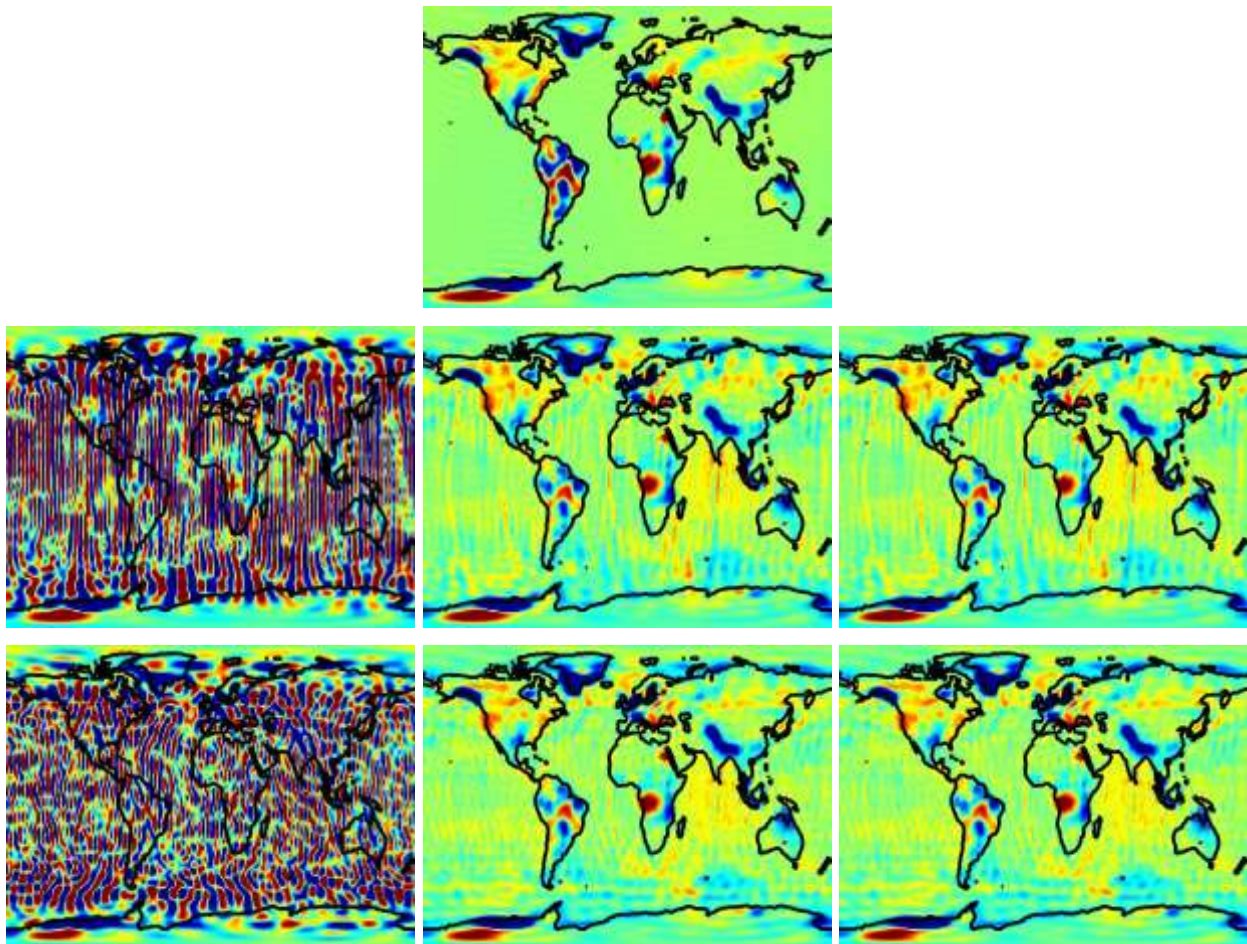


Figure 5-5. Estimated solutions using the set 'B' true models. True signal (row 1), single pair solution (row 2), double pair solution (row 3), single pair solution with GS (row 4) and double pair solution with GS (row 5). From row 2 to row 5, Case B1 (left), Case B2 (center) and Case B3 (right). Units are in cm of EWH and the figure includes hydrology and ice mass variations.

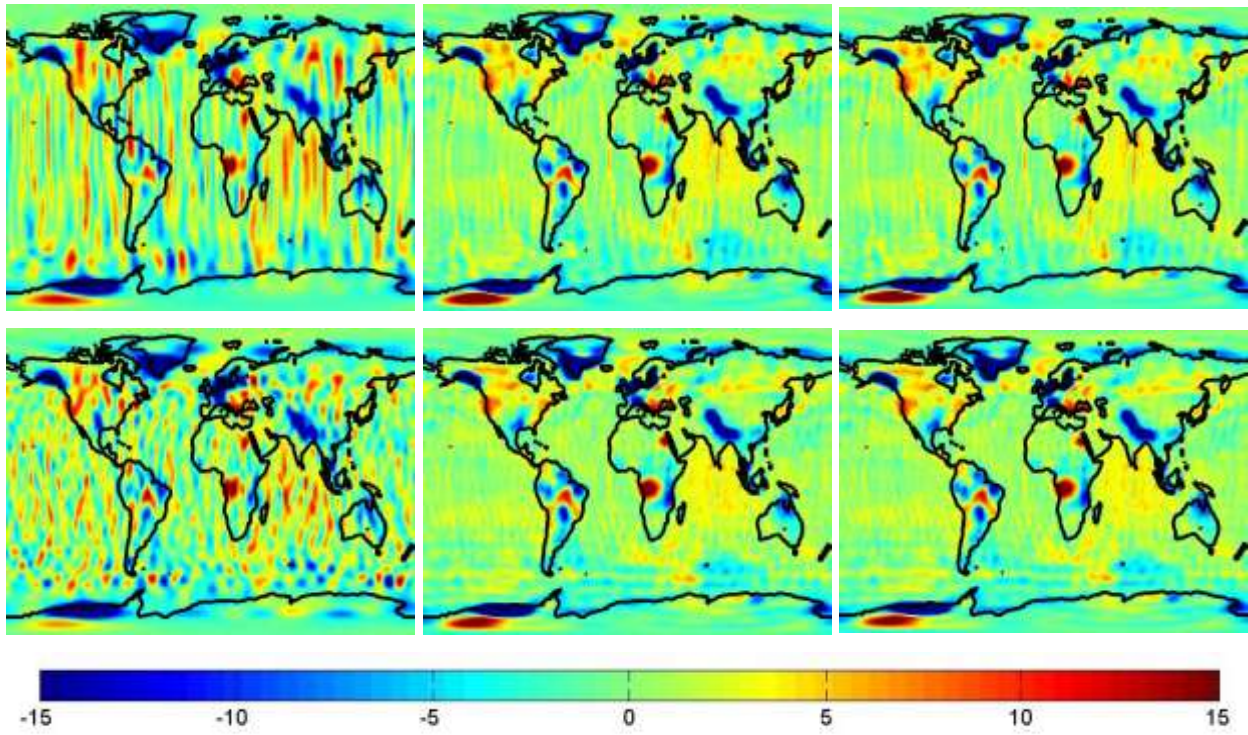


Figure 5-5. Continued.

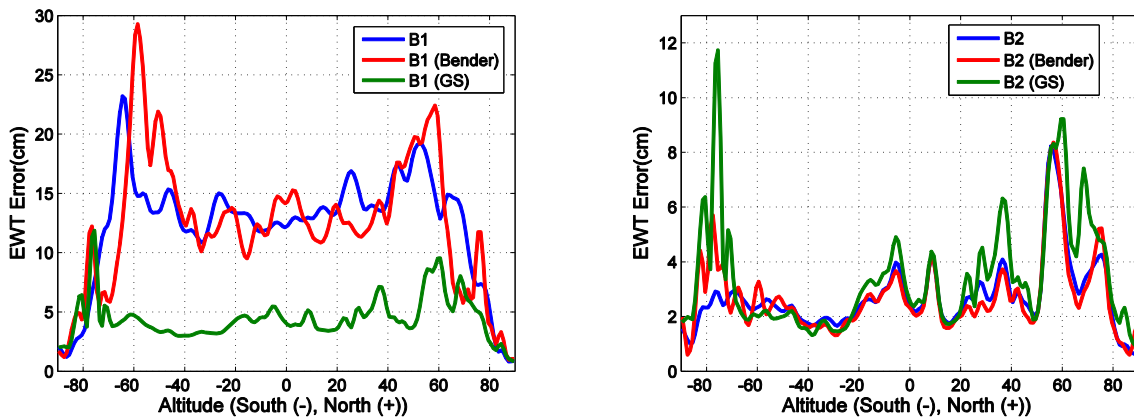


Figure 5-6. EWH error versus latitude plots; Case B1 on left and Case B2 on right.

Figures 5-3 and 5-5 clearly help to visualize the solutions. However, numerical values are needed to quantitatively assess these solutions. Table 5-1 shows the spatial root mean square (RMS) error of the EWH solution, shown graphically in Figures 5-3 and 5-5. The hydrology and ice (HI) error represents the error over the land and total error is the error over the entire map. According to the table, the total error is smaller

than HI error for most cases, which was not visible from the EWH maps. This is because the nominal models for the atmosphere and ocean bottom pressure were used to compensate for the variations over the ocean, but no nominal models were used to compensate for the HI variations. However, this may not always be true because the error of ocean and atmosphere models may still be greater than the HI variations. Even though the goal of this simulation is to estimate HI signals, it is suitable to look at the total errors because estimation errors can occur over both the land and the oceans.

Table 5-1. Spatial RMS errors for all cases in units of cm of EWH.

		HI Error (True: 12.44)		Total Error (True: 7.85)		Max. Error	
		Raw	GS	Raw	GS	Raw	GS
Case A1	1 Pair	11.72	4.50	11.85	3.30	83.15	55.96
	2 Pairs	11.90	4.32	11.58	3.19	97.66	57.96
Case A2	1 Pair	5.47	3.59	4.45	2.11	82.93	52.70
	2 Pairs	4.62	3.39	3.86	1.97	46.59	40.88
Case A3	1 Pair	5.45	3.58	4.44	2.10	82.46	52.75
	2 Pairs	4.62	3.39	3.84	1.97	44.84	40.84
Case B1	1 Pair	10.32	4.02	10.88	2.92	67.33	52.32
	2 Pairs	10.73	3.97	10.75	2.93	91.87	55.70
Case B2	1 Pair	1.97	1.99	1.29	1.21	31.55	49.85
	2 Pairs	1.87	1.91	1.18	1.13	28.26	31.56
Case B3	1 Pair	1.97	1.99	1.29	1.21	31.71	49.86
	2 Pairs	1.87	1.91	1.18	1.13	28.21	31.54

The numerical values in Table 5-1 show that the errors for Case A1 are larger than for Cases A2 and A3 in all categories. Focusing on the total errors, Case A1 error is more than 7 cm (59%) larger than Case A2. Moreover, Case A2 error is only 0.1 mm (0.2%) larger than Case A3 error. From this we can state that reducing the acceleration

noise level from the GRACE level to the GOCE level improves the solution and furthermore, reducing the acceleration noise level from the GOCE level to the LISA Pathfinder level improves the solution by only a negligible amount. The Bender formation improved the solutions for all three acceleration noise cases. However, Case A1 did not improve as much as Cases A2 and A3. To be more specific, Case A1 improved by ~3 mm and the other two cases improved by ~6 mm. This implies that the Bender formation has a larger impact when the solution is less dominated by the acceleration noise.

The spatial RMS errors for Cases B1, B2 and B3 show that by applying idealistic de-aliasing models, the errors are reduced. In addition, by applying Bender configuration, this aliasing error was further reduced for all three cases by ~1 mm. Reduction of these errors is expected since improved de-aliasing models were used. Again, looking at the numerical results and only focusing on the total errors, the Case B1 error is only 1 cm (8%) smaller than the Case A1 error. For other two cases, the errors were reduced more than 3 cm (67%) by applying idealistic de-aliasing models and an inclined pair of satellites. This enhances the conclusion that was made previously, which is that at the GRACE acceleration noise level, acceleration noise is a dominating source of error and when acceleration noise is below the level of GOCE, it is no longer a dominating source of error. Hence, we have determined that the aliasing error becomes one of the dominating sources once the acceleration noise is reduced to the GOCE level. In addition, even when the idealistic de-aliasing models are applied and an inclined pair of satellites is added, the acceleration noise still appears to be non-dominating, because the Case B3 solution showed no improvement compared to the

Case B2 solution. It is also interesting to compare raw and GS-applied solutions. Errors for Cases A2 and A3 with GS are less than 1 cm larger than the unfiltered solutions for Cases B2 and B3. This indicates the importance of GS, even though the effects of GS is limited by the magnitude of the original errors.

Discussion

We examined the results of a new low-low satellite-to-satellite tracking mission simulation using a range of residual acceleration noise levels and single and double pairs of satellites (in-line and in-line Bender formations). All other measurements noise and orbit parameters are kept constant so that the results reflect only the effects of acceleration noise. These residual acceleration noise levels were applied to find the suitable drag-free system accuracy for future gravity missions. To determine if acceleration noise levels below that of GOCE would be of value, the optimal in-line Bender formation by Wiese (2012) and idealistic de-aliasing models were used at the same time to reduce aliasing errors. By observing all the results above, including geoid degree difference (GDD) error curves, equivalent water height (EWH) graphs and associated spatial root mean square (RMS) error values, we could draw several conclusions.

First, it is clear that residual acceleration noise for drag-free systems in future geodesy missions should be lower than that of the electrostatic accelerometers used in GRACE, which is close to $1 \times 10^{-10} \text{ ms}^{-2} \text{ Hz}^{-1/2}$. The results above show that with this acceleration noise level, there are larger errors compared to other solutions. Moreover, when the additional pair of satellites and the idealistic de-aliasing models were used,

the solution only improved by 8%. This indicates that acceleration noise is the dominating source of error when it is equivalent to that of the GRACE accelerometers.

Using the GOCE and LISA Pathfinder drag-free residual acceleration noise levels improved the solutions, indicating that, as expected, such drag-free systems should be employed for future geodesy missions to increase the accuracy of the solution. However, the GDD error curves and the EWH plots for these two cases were nearly identical. Even though the spatial RMS error values indicated that the error for the LISA Pathfinder case was actually smaller than the error for the GOCE case, the difference between the two cases is less than 1%. This means that, it is unnecessary to further reduce the acceleration noise below that of the GOCE level.

Furthermore, when the acceleration noise is equivalent to that of the GOCE drag-free system, reducing the aliasing error by applying idealistic de-aliasing models and the Bender configuration improves the solution by 67%. This shows that at this acceleration noise level, aliasing is one of the dominating source of error, whereas acceleration noise is no longer a limiting one.

In addition, at this low level of aliasing error, further reduction of the acceleration noise down to the level of the LISA Pathfinder drag-free system did not improve the solution. This indicates that the acceleration noise remains non-limiting even when the aliasing error is reduced. Therefore, when aliasing error is reduced and the acceleration noise is below the level of the GOCE drag-free system, the solution is limited by the measurement noise and the variations in the hydrology and ice signals.

In sum, these results indicate that residual acceleration noise lower than the level of GOCE ($2 \times 10^{-12} \text{ ms}^{-2} \text{ Hz}^{-1/2}$) is not yet necessary with the simulated technology. In

other words, residual acceleration noise is no longer the limiting factor once it is near the level of the GOCE drag-free system for low-low satellite-to-satellite tracking with LRI, even when the aliasing errors are reduced using the optimal in-line Bender formation and idealistic de-aliasing models. However, the EWH spatial RMS errors indicate that when the overall error drops below 0.1 mm, there might be a need for a lower residual acceleration noise.

This conclusion may be related to the conclusion of Loomis (2012). Loomis showed from his simulation that reducing the acceleration noise level from GRACE to the drag-free system, the solution was improved although applying LRI instead of the microwave ranging interferometer (MRI) did not show any improvements. However, one cannot make direct comparisons with this work, since the acceleration noise magnitude for the drag-free system that was used in Loomis' work was not clearly provided in terms of acceleration noise. However, it is clear that the same acceleration noise models were used for the case of the GRACE electrostatic accelerometers. But the conclusion that reducing the residual acceleration noise improves the solution is consistent with this conclusion, even though the altitude and range between the two satellites were varied along with the acceleration noise in Loomis' work.

Another conclusion that can be drawn from this analysis is that adding a second pair of satellites only modestly improved the estimation results. Moreover, when idealistic de-aliasing models were applied, second pair only improved the result by 1 mm for all cases. Also, it was shown that adding an inclined pair of satellites, increased error at latitudes above 70 degrees. Overall, this might be in contrast to the work of Wiese (2012), which showed significant improvements to the single polar pair solutions

when an inclined pair of satellites was added. However, there are significant differences between the mission architecture analyzed here and that of Wiese (2012), which is listed in Table 5-2.

Table 5-2. Differences between current and Wiese simulations.

	Current	Wiese
Batch Size	3 hours	1 day
Estimated Coefficients	degree and order 60	degree and order 100
Altitude	~350 km	290~300 km
Separation Distance	220 km	100 km
Repeat Period	14 days	13 days
LRI noise	$80 \text{ nm Hz}^{-1/2}$	$5 \text{ nm Hz}^{-1/2}$
GOCE Drag-free noise	$2 \times 10^{-12} \text{ ms}^{-2} \text{ Hz}^{-1/2}$	$10 \times 10^{-12} \text{ ms}^{-2} \text{ Hz}^{-1/2}$

In general, our gravity field estimates are better than those of Wiese (2012) for the single pair case. However, the opposite is true for the double pair case. In Wiese's analysis the second pair of satellites reduced the error by ~50%, whereas, for this analysis, the second pair reduced the error by only ~16% (~1 cm EWH). From Table 5-2, it is clear that the biggest differences between the two simulations are the size of the data batch, number of estimating parameters, and the noise levels. Increasing from degree and order 60 to 100 is equivalent to estimating more than double the number of parameters. Estimating more parameters would cause greater uncertainty in the estimates of each parameter, especially since there are more aliasing errors at higher degree coefficients. Moreover, the LRI noise and altitude would tend to reduce the accuracy of this analysis, but the acceleration noise is higher for Wiese's analysis. As a

consequence, for the single pair result, it is possible that Wiese's solutions had greater error caused by the higher acceleration noise. There are several explanations for the discrepancy of the results for the double pair case. One of them is that since the LRI noise used in this analysis was more than factor of 10 times higher than that used in Wiese (2012), our solution may have been limited by the LRI noise, such that the second pair could not further improve the solution. Another possible explanation is the difference in the batch size. Reducing the batch size from 1 day to 3 hours may have a large effect on the solution, since having a smaller batch size would make the estimation process more sensitive to the high frequency signals. This may reduce the aliasing error, which appears mostly in high degree coefficients. However, the repeat periods used in two simulations are roughly the same, so if the batch size is influencing the result, it would be due to the nonlinear nature of the model or numerical issues. In addition, smaller arc length allow less temporal aliasing errors since the orbits are readjusted every 3 hours. These explanations may obfuscate the benefit of the second pair of satellites. This explanation is consistent with the phenomenon of having lower single pair solution error and higher double pair solution error, compared with Wiese (2012).

Flechtner (2016) applied acceleration noise equivalent to that of the GRACE accelerometers to simulate the expectations of GRACE-FO mission. Comparing his result with Case A1 single pair solution from Table 5-1, we find that there is a significant difference between the two results. There are many variables that define the two simulations, but clearly there are several factors that can explain the large discrepancy between the two results. First, altitude for the GRACE-FO dedicated simulation was

more than 100 km higher than the altitude used for this research. The repeat period was kept constant only for this research, which is another advantage of drag-free systems compared with accelerometer in addition to having lower acceleration noise. Also, similar to the analysis of Wiese (2012), there were more parameters estimated for the GRACE-FO simulation compared to this work. The plots of EWH error verses spherical harmonic degrees in Flechtner's work show that the error level increases excessively as the degree of the coefficients increases. Therefore, it is likely that if the solution was computed only up to degree and order of 60, as was done in this research, the total average error would decrease compared to the Case A1 solution. Moreover, having different de-aliasing models and forward models would also cause discrepancies between the two analyses.

Finally, we conclude that for low-low satellite-to-satellite tracking with LRI, the suitable residual acceleration noise for the drag-free system is found to be around $2 \times 10^{-12} \text{ ms}^{-2} \text{ Hz}^{-1/2}$, which is equivalent to the drag-free system used in the GOCE mission. Further simulation analysis is recommended to determine the exact upper and lower bounds of the residual acceleration noise that can maintain the solution errors within say a few percent, as well as whether or not a non-drag-free electrostatic accelerometer with this level of performance would provide similar results.

CHAPTER 6

IMPROVEMENTS IN ESTIMATION

State and Measurement Uncertainty

It was brought up in Chapter 4, that the state uncertainty was bounded by the number found empirically, which is applied to all parameters equivalently. This is because most of the state uncertainty is caused by the unknown uncertainty of de-aliasing models and the actual Hydrology and Ice signal. Therefore, it is impossible to design the state noise covariance matrix that accurately represents the state uncertainty unless there exists a model that precisely represents this true signal. This is why the state noise covariance is designed such that the estimation depends mostly on the measurement data, rather than a priori information, which is actually set equal to zero for all arcs. Also, it seems plausible to repeat the entire estimation process using the state noise covariance matrix computed by the previously estimated result. However, since the estimated solution is not perfect, the errors will restrict the solution from recovering the true signals. Therefore, it is better to allow the estimator to depend mostly on the measurements.

On the other hand, knowledge of measurement uncertainty is known. This allows the computation of the precise measurement noise covariance (MNC) matrix. However, in Chapter 4, there were two assumptions made to simplify the process. These assumptions are (a) considering measurement noise as white and (b) assuming that acceleration noise has no effect on the measurement data. In this chapter, these assumptions are removed to make a more precise MNC matrix and so improve the estimation. At first, auto-regressive moving-average (ARMA) filter is designed and used to consider the correlation of the noise, which

was previously ignored. Moreover, the known acceleration noise spectrum is used to modify the measurement covariance matrix to account for the unmeasured acceleration noise that actually caused additional uncertainty to the measurements. Methods and results of this improved estimation routine are presented in this chapter.

ARMA Filter

As seen from Table 3-3 and Figure 3-3, the LRI and acceleration noises are colored, although up to this point all the noise covariance were considered as white in the estimation routine. This is because of the complexity that arises when dealing with correlation of the noise. This noise correlation can be applied in the estimation using an auto-regressive moving-average (ARMA) filter and Toeplitz systems with the same noise power spectral density (PSD) that were used to generate the measurements [Klees *et al.*, 2003]. In other words, if the colored noise and the PSD of the noise model are provided, an ARMA filter can be designed that can filter white noise into colored noise.

The ARMA filter is given in Equations (6-1), where $y(t)$ is the filtered output and $e(t)$ is the white noise with variance σ^2 [Stoica and Moses, 1997].

$$\begin{aligned} A(q)y(t) &= B(q)e(t) \\ q^{-k}y(t) &= y(t - k) \end{aligned} \tag{6-1}$$

Equation (6-1) can be rewritten as Equation (6-2), where $\{a_i\}_{i=1}^n$ and $\{b_i\}_{i=1}^m$ are parameters of the filter [Stoica and Moses, 1997]. Once we find these parameters, then we use these values to compute the correlated measurement covariance matrix. There are two special cases. The filter is called auto-

regressive (AR) when $m = 0$ and when $n = 0$, the filter is called moving-average (MA).

$$y(t) + \sum_{i=1}^n a_i y(t-i) = \sum_{j=0}^m b_j e(t-j), \quad (b_0 = 1) \quad (6-2)$$

Before estimating the filter parameters, the auto-covariance sequence (ACS) of the signal must be calculated. This can be done by applying the inverse Fourier transform to the sampled power spectral density (PSD) of the correlated noise. The equation for the ACS computation is provided below [Klees et al., 2003].

$$r_n = \Delta f \sum_{k=0}^{N_f-1} P_k \exp(i2\pi kn/N_f), \quad 0 \leq n \leq L \quad (6-3)$$

$$\Delta f = 1/N_f \Delta t$$

Here, r_n is the auto-covariance of lag n , P_k is the sampled PSD noise function with frequency $f_k = k\Delta f$, N_f is the length of the noise samples in the time domain used to estimate the PSD, Δt is the sampling time, and L is the maximum lag, which cannot exceed $N_f/2$.

Now, an assumption is made that an AR filter with very large n , $C(q)$, is equivalent to an ARMA filter as shown in Equation (6-4) [Stoica and Moses, 1997]. With this idea, parameters $\{c_i\}_{i=1}^{n'}$ will be estimated, and then these estimates will be used to estimate the ARMA parameters $\{a_i\}_{i=1}^n$ and $\{b_i\}_{i=1}^m$.

$$y(t) = \frac{B(q)}{A(q)} e(t) \approx \frac{1}{C(q)} e(t) \quad (6-4)$$

This AR filter with large n is also known as a ‘long AR’ filter and its parameters can be computed by applying the Yule-Walker method using the ACS computed

previously. The relation between the ACS and AR filter parameters is shown in Equation (6-5) [Stoica and Moses, 1997].

$$\begin{bmatrix} r_0 & r_1^* & \dots & r_n^* \\ r_1 & r_0 & & \vdots \\ \vdots & \ddots & r_1^* & \\ r_n & \dots & r_0 & \end{bmatrix} \begin{bmatrix} 1 \\ c_1 \\ \vdots \\ c_n \end{bmatrix} = \begin{bmatrix} \sigma^2 \\ 0 \\ \vdots \\ 0 \end{bmatrix} \quad (6-5)$$

Using Equation (6-5), $\{c_i\}_{i=1}^{n'}$ and σ^2 are computed using a least squares estimation.

The ARMA filter parameters can be computed by the following steps.

Equation (6-2) can be rearranged as follows [Stoica and Moses, 1997].

$$\begin{aligned} y(t) + \varphi^T(t)\theta &= e(t) \\ \varphi^T(t) &= [y(t-1), \dots, y(t-n) | -e(t-1), \dots, -e(t-m)] \\ \theta &= [a_1, \dots, a_n | b_1, \dots, b_m]^T \end{aligned} \quad (6-6)$$

If we let $t = L+1, \dots, N$, then Equation (6-6) can be written as [Stoica and Moses, 1997],

$$\begin{aligned} z + Z\theta &= e \\ Z &= \left\{ \begin{array}{ccc|ccc} y(L) & \cdots & y(L-n+1) & -e(L) & \cdots & -e(L-m+1) \\ y(L+1) & \cdots & y(L-n+2) & -e(L+1) & \cdots & -e(L-m+2) \\ \vdots & \ddots & \vdots & \vdots & \ddots & \vdots \\ y(N-1) & \cdots & y(N-n) & -e(N-1) & \cdots & -e(N-m) \end{array} \right\} \\ z &= [y(L+1), y(L+2), \dots, y(N)]^T \\ e &= [e(L+1), e(L+2), \dots, e(N)]^T. \end{aligned} \quad (6-7)$$

In Equation (6-7), z is the provided colored noise vector, and e is the approximated white noise vector, which was computed by the long AR filter from Equation (6-4). Then, by applying least squares estimation of the above equation, θ can be estimated, which is denoted as $\hat{\theta}$. Finally, white noise variance is estimated as shown in Equation (6-8) [Stoica and Moses, 1997].

$$\hat{\sigma}^2 = \frac{1}{N-L} \tilde{e}^* \tilde{e}$$

$$\tilde{e} = z + Z|_{y,\hat{\theta}} \hat{\theta}$$

$$\hat{e} = z + Z|_{y,e} \hat{\theta}$$
(6-8)

Now the ARMA filter parameters are computed by applying Toeplitz systems, to create a well-defined measurement covariance. Two Toeplitz matrices are defined as follows [Klees et al., 2003],

$$A = \text{toeplitz}(1, a_{p,1}, a_{p,2}, \dots, a_{p,p}, 0, \dots, 0)$$

$$B = \text{toeplitz}(1, b_{q,1}, b_{q,2}, \dots, b_{q,q}, 0, \dots, 0).$$
(6-9)

These defined Toeplitz matrices can represent the filter that takes white noise (ε) as an input and colored noise (ξ) as an output, which is shown below [Klees et al., 2003].

$$\xi = G\varepsilon$$

$$G = A^{-1}B$$
(6-10)

Lastly, the MNC matrix is computed as presented below.

$$P_\varepsilon^{ARMA} = \text{cov}(\xi, \xi) = \text{cov}(G\varepsilon, G\varepsilon) = G\{\text{cov}(\varepsilon, \varepsilon)\}G^T = \hat{\sigma}^2 GG^T$$
(6-11)

It is important to make sure that P_ε^{ARMA} is a positive definite symmetric matrix for estimation to work without numerical error.

Before applying the above covariance matrix in the estimation process, the designed ARMA filter was tested. The generated noise shown in Figure 3-3, was used to design the ARMA filter through the process explained in this section. Once the ARMA filter is designed, the white noise is created using the variance found during the process. This white noise is passed through the ARMA filter to create the colored noise. This ARMA filtered noise is compared with the

simulated noise from the previous chapter. Figure 6-1 shows the ASD of generated and ARMA filtered LRI noise with the noise model. The figure shows that the ARMA filtered noise ASD resembles the generated noise. This confirms that the ARMA filter was designed well enough to be applied in the estimation routine.

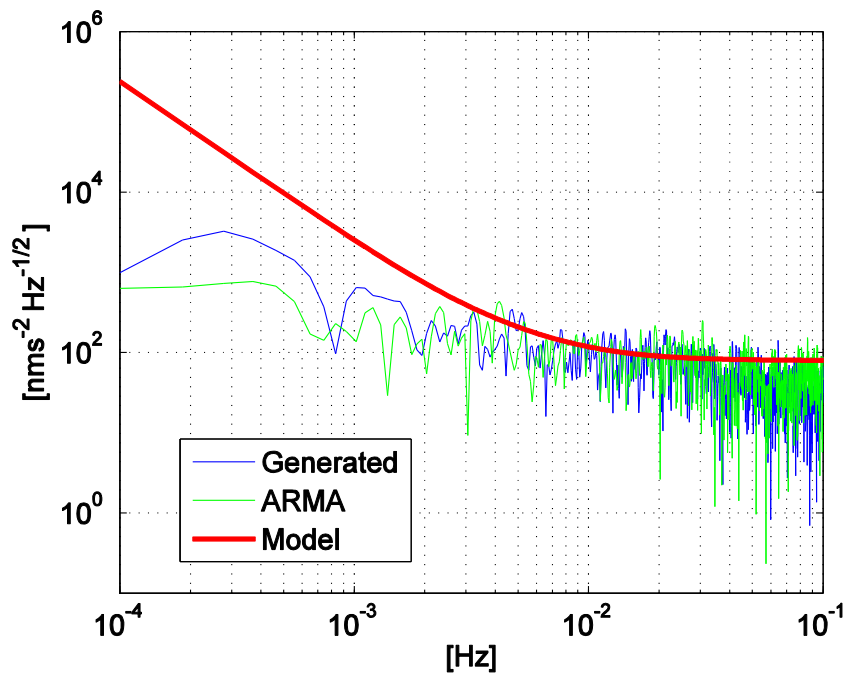


Figure 6-1. ASD of the LRI generated noise, the ARMA filtered noise, and the noise model.

Accounting for Acceleration Noise in the Estimation Routine

During the simulation process, several different acceleration noise levels were used, each representing a specific case. However, since acceleration is not part of the measurement vector, the information about the acceleration noise was not included when creating the covariance of the measurement uncertainty, even though the acceleration noise actually affects the measurements. Therefore, it is worth exploring the effects of building an MNC matrix that accounts for the acceleration noise.

The first task is to create the transformation matrix, D , that relates the acceleration and the measurement data. It is difficult to create a transformation matrix that performs double integration such that the acceleration can be converted to positions and range measurements. Instead, the transformation matrix is computed in two steps. First, using Equation (4-1), the transformation matrix that relates acceleration and the spherical harmonic coefficients is computed. Once this matrix is created, it is multiplied by the Jacobian matrix, which transfers the state parameters to the measurements. From this point, acceleration noise covariance (ANC) matrix, P_a , is computed as shown in Equation (6-12) and the resulting new MNC matrix, P_ϵ' , is simply computed by the summation presented in Equation (6-13).

$$P_a = \text{cov}(D\vec{v}, D\vec{v}) = E[(D\vec{v} - E(D\vec{v}))(D\vec{v} - E(D\vec{v}))^T] = D\{\text{cov}(\vec{v}, \vec{v})\}D^T \quad (6-12)$$

$$P_\epsilon' = P_\epsilon + P_a \quad (6-13)$$

Applying both the ARMA Approximation and the ANC

In the previous two sections, the ARMA approximation and the ANC were explained. Each of these methods are independent approaches to improving the model of measurement covariance matrix. The ARMA approximation considers the correlation of the LRI noise and the ANC accounts for the acceleration noise's influence on the measurements. These two methods can be applied together. Moreover, all generated acceleration noise are colored noise as shown in Figure 3-3. Therefore, the same ARMA approximation can be applied to create the ANC matrix, P_a^{ARMA} , and this ANC can be added to the ARMA approximated measurement noise as shown in Equation (6-14).

$$P'_\epsilon = P_\epsilon^{ARMA} + P_a^{ARMA} \quad (6-14)$$

To verify that the ARMA approximation of the acceleration colored noise is correct, the ASD of filtered noise was drawn with the generated noise in Figure 6-2. This figure shows that both the filtered and generated noises have the same amplitude over the entire spectrum. This means that the ARMA filter was designed well and converts white noise to the colored noise that is similar to the actual noise.

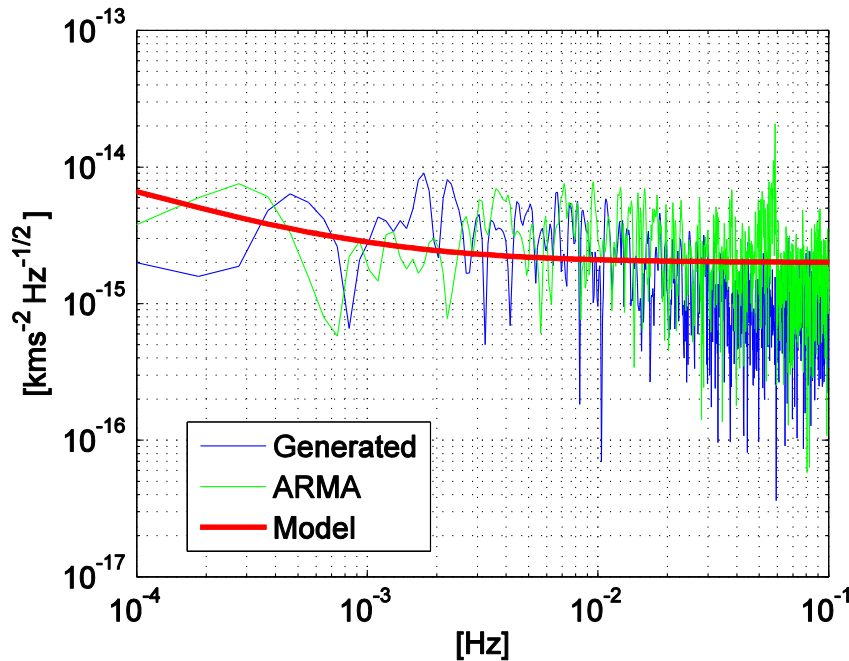


Figure 6-2. ASD of the GOCE-level drag-free acceleration generated noise, the ARMA filtered noise, and the noise model.

Result

Case A2 was recomputed three times in the same manner as explained in Chapter 4 to see how the solution was affected by different modified MNC matrices. At first, the ARMA approximation method was applied. Then, the ANC was added to MNC without the ARMA approximation. Lastly, both the ARMA approximation and the ANC were used to estimate the solution. The new

solutions are analyzed and compared with the previous solution from Chapter 5.

It is important to make sure that MNC matrices are always positive definite.

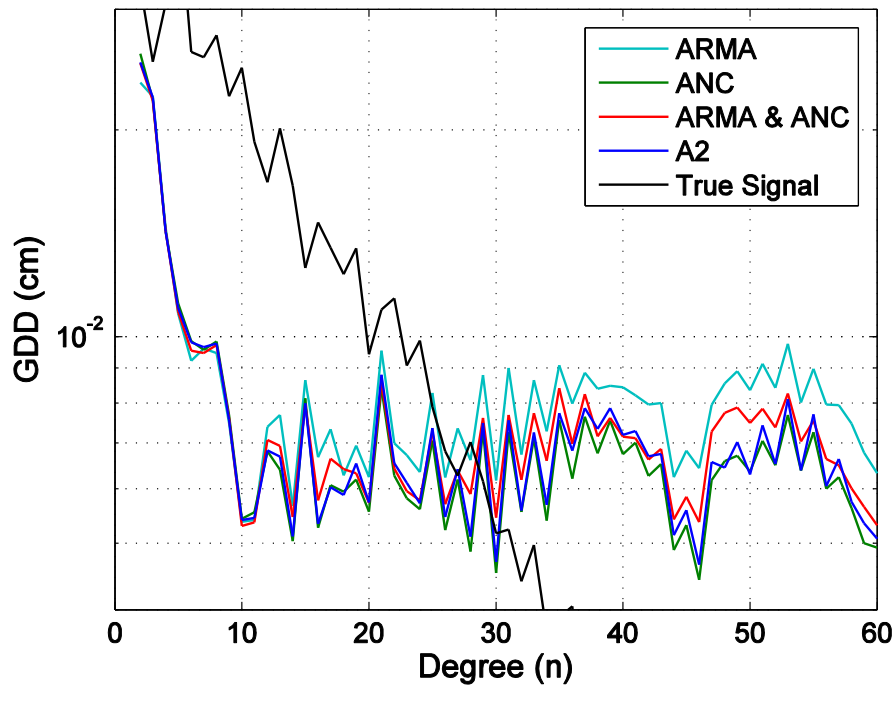
Fortunately, all the MNC matrices created were positive definite, and so the estimation was performed without running into any numerical issues.

The GDD error curves for the different solutions are drawn in Figure 6-3.

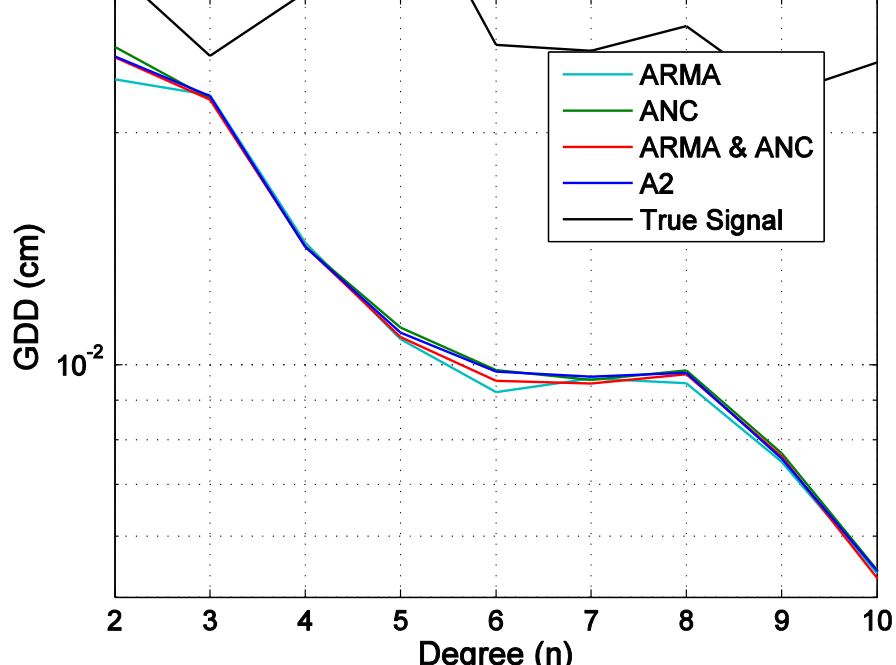
From the figure, it can be seen that geopotential coefficients beyond degree 10, show comparably larger differences than those below degree 10. It is clear that, the ARMA approximated solution has largest error and the ANC applied solution has the smallest error for coefficients greater than degree 10. When both the ARMA and the ANC were applied, the error level was between the ARMA only and the ANC only levels, but almost always higher than the previous solution.

The result for coefficients below degree 10 need to be looked more closely to observe which solution is more accurate. Figure 6-3-b shows the zoomed in view of Figure 6-3-a for degrees below 10. It can be seen from this zoomed in view, that the ARMA approximation improves the solution for degrees less than 10, although it makes the solution worse for coefficients greater than this degree.

GS-applied GDD errors are shown in Figure 6-3-c. A radius of 300 km was applied to all GS solutions. Since the radius was 300 km, GS does not affect solutions below degree 20 and therefore the conclusion for low degree terms remains constant. Even for higher degrees, the conclusion that the ARMA approximation increases error, is still applicable to filtered solutions. When GS is applied, the ANC error is almost identical to the initial error.

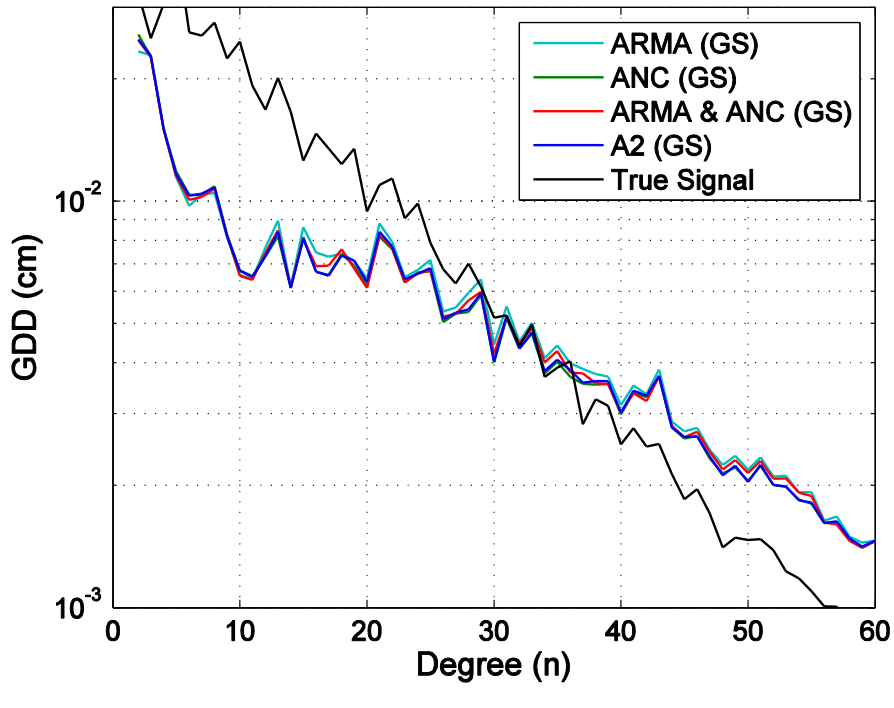


(a)



(b)

Figure 6-3. Errors of the ARMA and the ANC applied single pair solutions for Case A2 expressed as GDD; (a) raw errors, (b) raw errors for low degrees, and (c) GS-applied errors.



(c)

Figure 6-3. Continued.

In addition to the GDD error curves, EWH plots are drawn for each estimation method and they are shown in Figures 6-4 and 6-5. The corresponding spatial RMS values are shown in Table 6-1. Figure 6-4 shows different EWH plots that represent raw estimated solutions and Figure 6-5 include EWH plots that are filtered by GS with a 300 km radius. For both figures, the top-left panel is the initial solution, the top-right panel is the ARMA approximated solution, the bottom-left panel is the ANC applied solution and the bottom-right panel is the both ARMA approximated and ANC applied solution. From the figures, it can be clearly observed that when ARMA approximation is applied with or without ANC, more error stripes appear. Other than this, it is difficult to tell the difference between the plots. When GS is applied, all four solutions look alike. From Table 6-1, it is clear that the ARMA approximation

increases the error by ~ 1 cm compared to the initial solution. On the other hand, the ANC improves the initial solution by 1~2 mm. When both methods are used at the same time, the error increased but not as much as the ARMA case. When GS is applied to the solutions, the magnitude of the changes are decreased but the general trends remain constant.

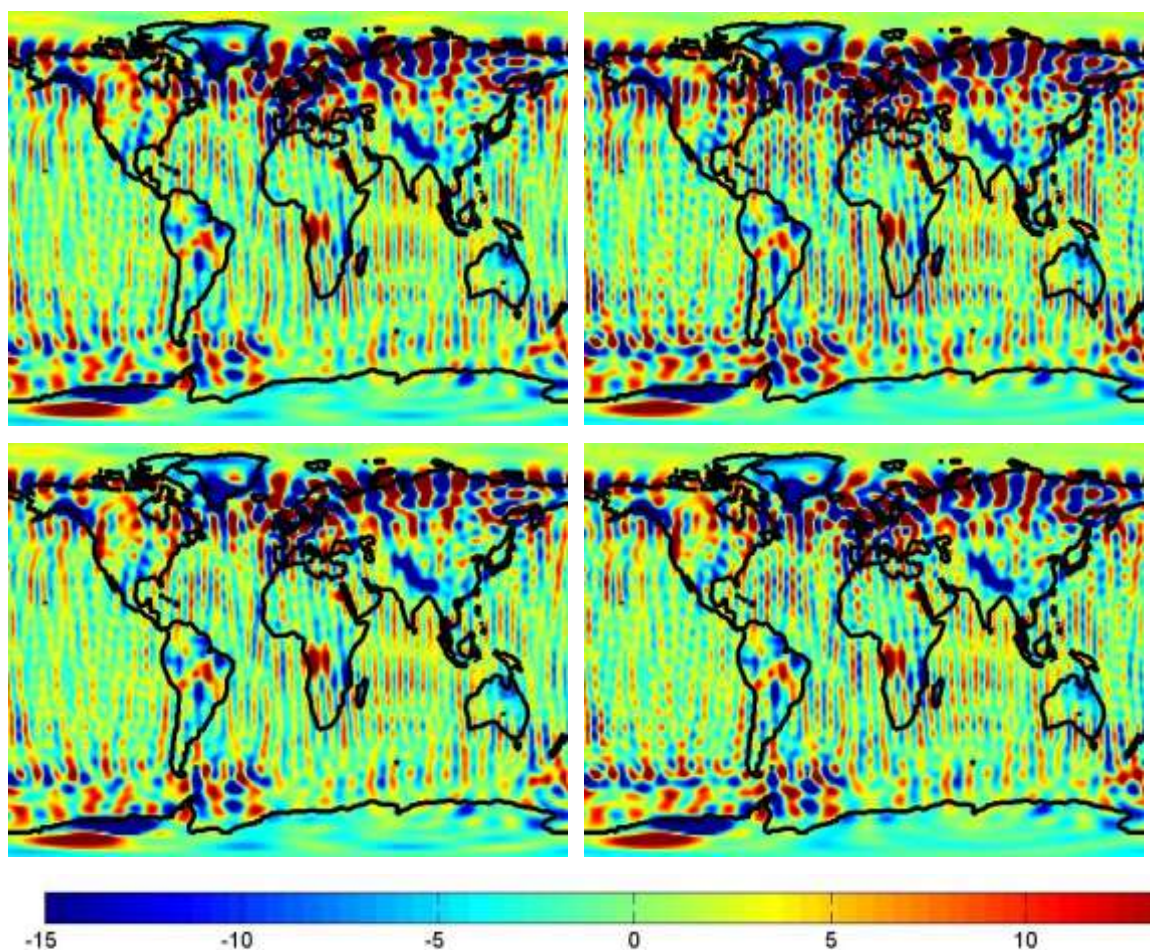


Figure 6-4. Estimated single pair solutions for Case A2 in units of cm of EWH with various MNC matrices. Initial (top-left), ARMA approximation (top-right), ANC (bottom-left) and ARMA approximation & ANC (bottom-right).

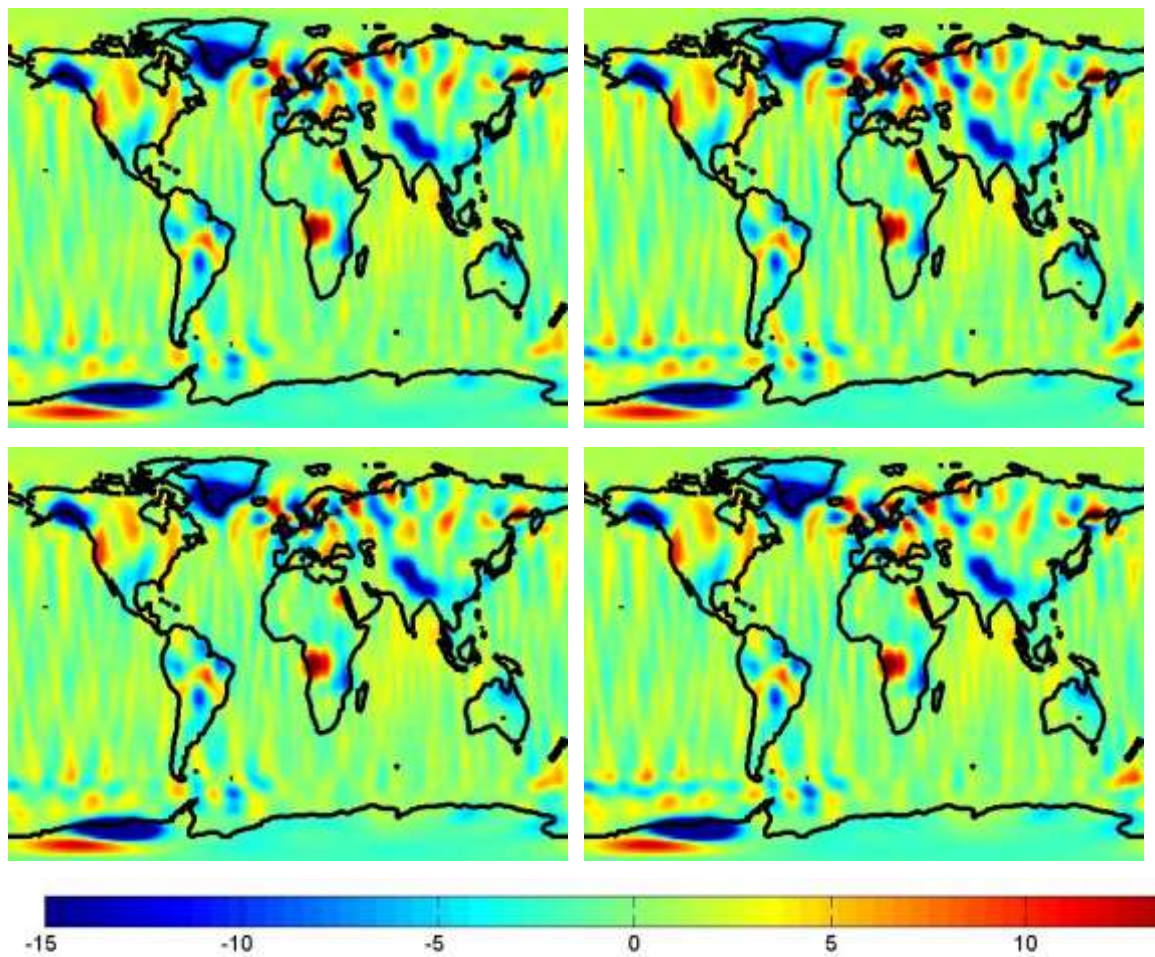


Figure 6-5. GS-applied single pair solutions for Case A2 in units of cm of EWH with various MNC matrices. Initial (top-left), ARMA approximation (top-right), ANC (bottom-left) and ARMA approximation & ANC (bottom-right).

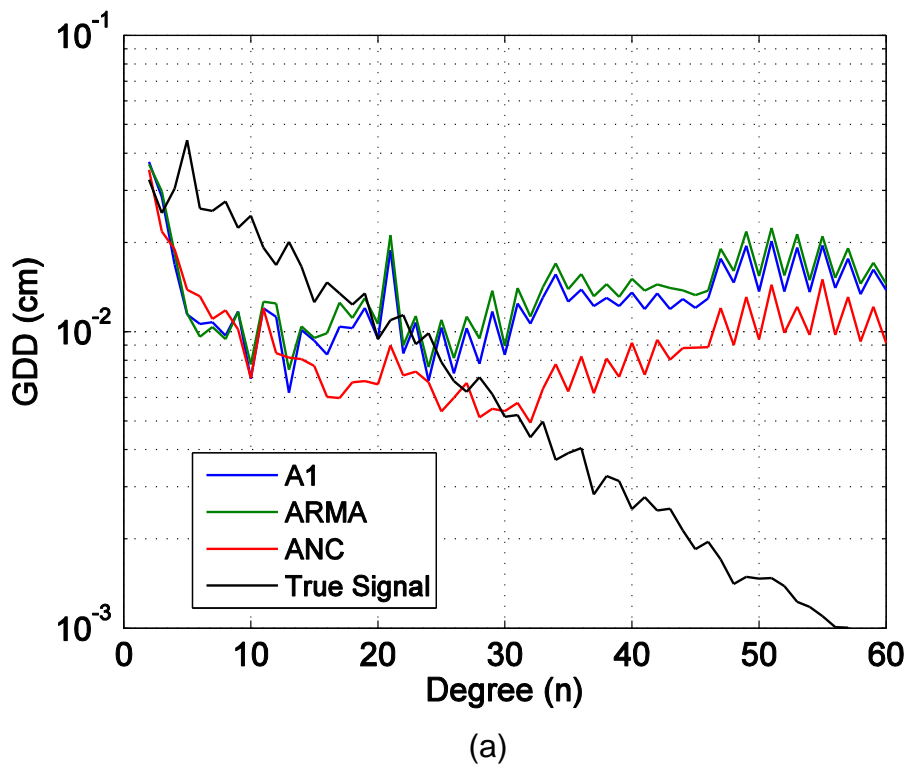
Table 6-1. Spatial RMS error for Case A2 in units of cm of EWH with various MNC matrices.

	HI Error (True: 12.44)		Total Error (True: 7.85)		Max. Error	
	Raw	GS	Raw	GS	Raw	GS
Initial	5.47	3.59	4.45	2.11	82.93	52.70
ARMA	6.49	3.72	5.34	2.26	115.81	52.39
ANC	5.31	3.55	4.27	2.08	82.39	52.36
ARMA & ANC	5.63	3.58	4.61	2.13	115.2	51.72

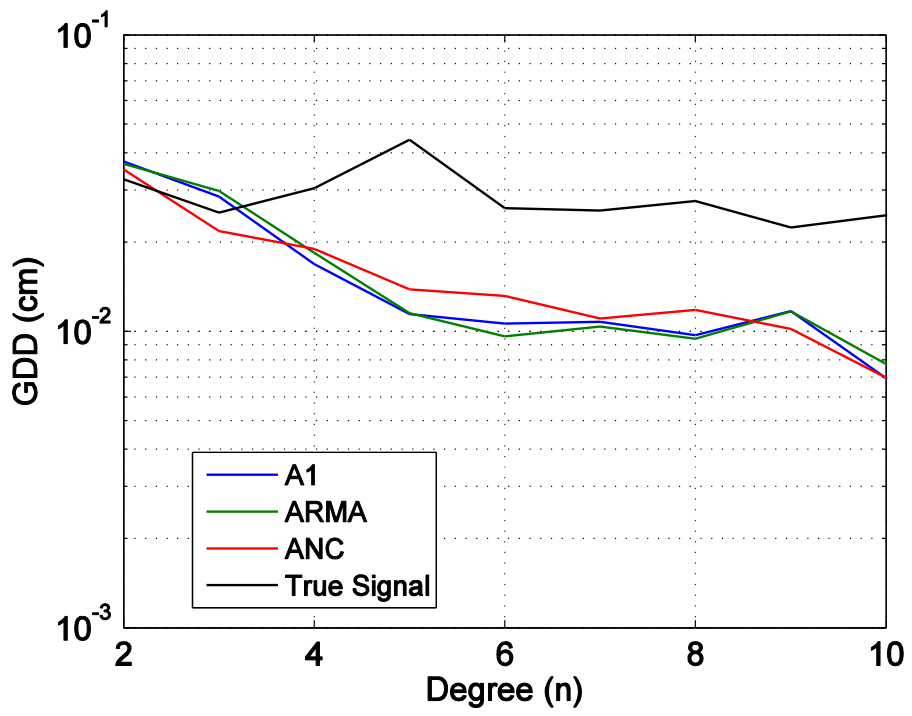
Applying the ARMA Approximation and the ANC for Higher Acceleration Noise Level Mission

In the previous section, the result of applying the ANC showed small improvements for the case of using the GOCE level residual acceleration noise (Case A2). We have seen from Chapter 5 that at this noise level, the residual acceleration noise probably has a small effect compared to other error sources, since decreasing the noise beyond this level did not change the solution. However, applying the ANC still improved the solution, which indicates that for higher acceleration noise levels, the ANC will be more effective. Therefore, in this section, the estimation is repeated for Case A1 with the ARMA approximation and the ANC. It can be expected that the ARMA approximation will not have large impact on the solution, since the overall error is large for Case A1. However, a big improvement is expected by applying the ANC.

The results are shown in a similar manner as was done previously starting with the GDD errors in Figure 6-6. It is very clear from the figure that the ANC improved the general solution. In fact, beyond degree 13, the ANC based errors are always smaller than the initial solution. However, for low degrees, it is difficult to tell which solution is the best one. Figure 6-6-b shows a closer view near low degree coefficients and the ARMA and initial solutions are better than the ANC solution. This is consistent with the result for Case A2. Nevertheless, unlike Case A2, the ARMA approximation does not improve the solution for low degree coefficients. The GS-applied GDD errors are shown in Figure 6-6-c. The ANC solutions are still distinctively better than the other two solutions for degrees beyond 10. For degrees below 10, the ARMA approximation seems to be slightly better than the initial solution.

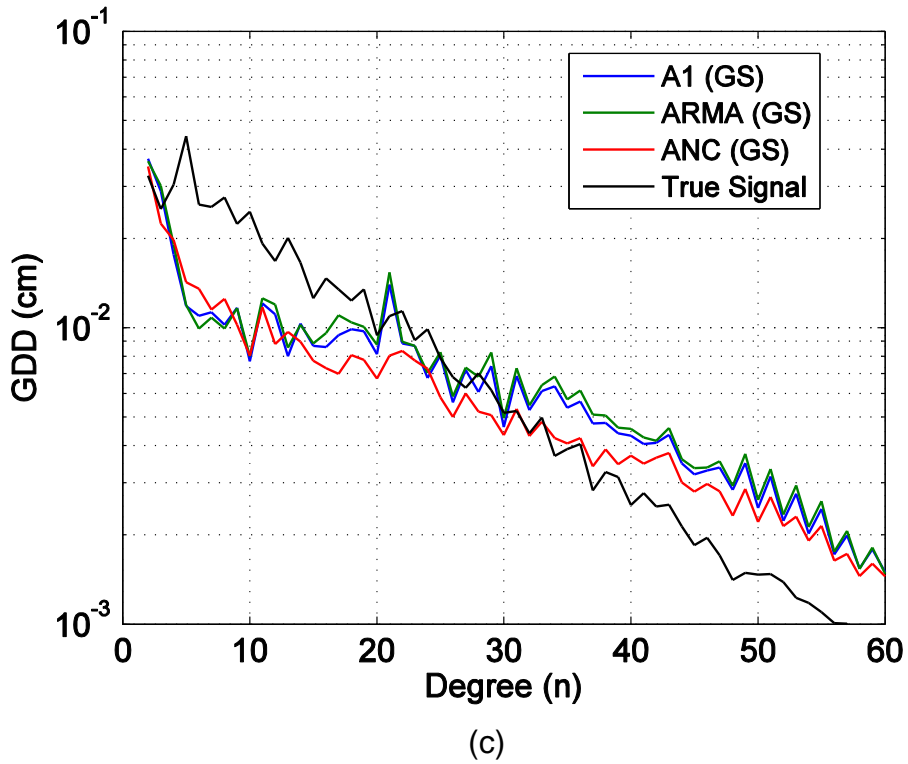


(a)



(b)

Figure 6-6. Errors of the ARMA and the ANC applied single pair solutions for Case A1 expressed as GDD; (a) raw errors, (b) raw errors for low degrees, and (c) GS-applied errors.



(c)

Figure 6-6. Continued.

The EWH color maps for the different methods of Case A1 are shown in Figure 6-7. The first row shows the initial solutions, the second row is the ARMA approximated solutions and the third row shows the ANC applied solutions. The solutions on the left column are the raw and the right column are the GS-applied solutions. From this figure, it is somewhat difficult to notice the difference between the initial solutions and the ARMA approximated solutions. Nonetheless, it is readily seen that the ANC applied solutions have less error stripes for both the filtered and the non-filtered solutions. Table 6-2 shows the corresponding spatial RMS errors. These numerical values show that the ARMA approximation increased the error about 1 cm, whereas the ANC decreased the error by almost 4 cm. Even when GS is applied, the ANC showed 1 cm improvement.

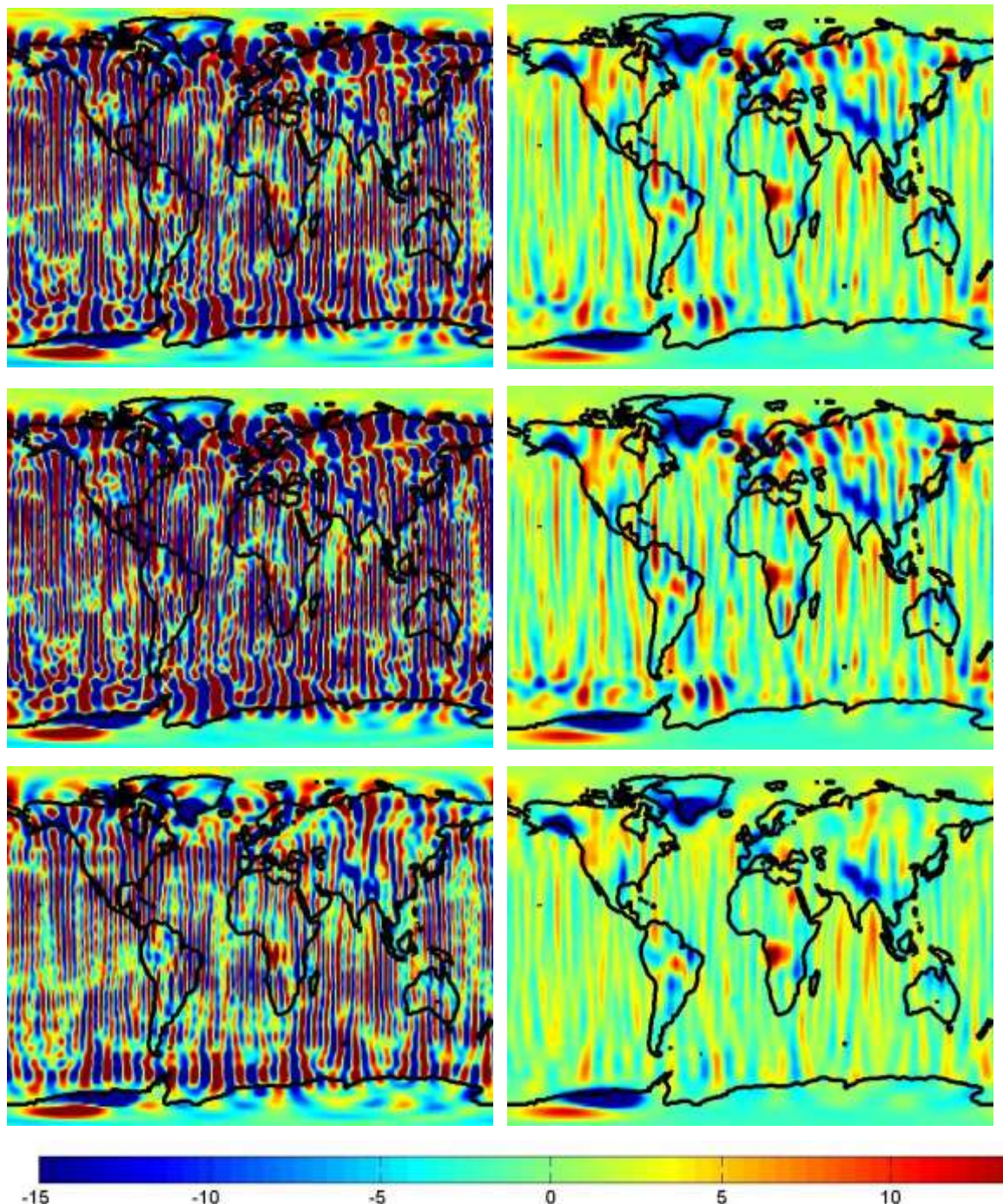


Figure 6-7. Estimated single pair solutions for Case A1 in units of cm of EWH
with various MNC matrices. Initial (row 1), ARMA approximated (row 2)
and ANC (row 3), non-filtered (left), and filtered (right) solutions.

Table 6-2. Spatial RMS error for Case A1 in units of cm of EWH with various MNC matrices.

	HI Error (True: 12.44)		Total Error (True: 7.85)		Max. Error	
	Raw	GS	Raw	GS	Raw	GS
Initial	11.72	4.50	11.85	3.30	83.15	55.96
ARMA	12.91	4.71	12.85	3.51	106.58	55.97
ANC	7.78	3.71	8.11	2.52	46.48	54.67

Discussion

In this chapter, the estimation routine was modified by removing some of the simplifying assumptions that were made regarding the measurement noise in the previous chapter. These assumptions were (a) having no correlation on the measurement noise and (b) no effects of acceleration noise accounted for the measurement noise. By applying the ARMA approximation, the measurement noise was considered to be correlated and by adding the ANC to the MNC, the effect of acceleration noise on the measurement data was included. This was first applied to Case A2, where the residual acceleration noise is equivalent to the GOCE drag-free system. The result showed that the ANC generally improved the solution by 1~2 mm (3%) and the ARMA increased the overall error by ~1 cm (18%). However, when the errors were observed closely, it was seen that the ARMA improved the solution for low degree coefficients (less than 10) and ANC improve the solution for high degree coefficients (greater than 10). These modified estimation methods were also tried for Case A1, GRACE-level residual acceleration noise. As expected from the results of Case A2, the ANC improved the initial solution dramatically by 3~4 cm (30%) and ARMA approximation again increased the error by ~1 cm (8.5%). Even for Case A1, the ANC improved the

solution for high degree coefficients (greater than 10), but the ARMA showed improvement in low degree coefficients (less than 10) only for the GS-applied solution. However, for both cases, it was clear that the ARMA approximated solutions were better than the ANC solutions at low degrees and vice versa for high degrees.

When the ARMA approximation was applied, the knowledge on the correlation of the noise informed the estimator that the noise actually has larger errors for lower spatial frequencies. This additional information about the low frequency noise allowed the estimator to estimate the low degree coefficients more accurately, although the improvement was small. The results for Case A1 showed a larger improvement compared to Case A2 when the ANC was applied. This is because based on the result from Chapter 5, it is clear that Case A1 was dominated by the acceleration noise.

In order to make the best use of the ARMA approximation and the ANC, the solutions from the two methods were combined. The GDD error curves showed that the ARMA approximation improved the solution for degrees below 10, whereas the ANC decreased the error for degrees above 10 for both cases. Therefore, the results from the ARMA approximation and the ANC were combined to see how much the solutions are improved. For up to degree 10, the ARMA approximation solution and for higher degrees, the ANC solution were taken. The EWH for these combined solutions were computed and the corresponding spatial RMS is shown in Table 6-3. The GDD error curves and EWH color maps are neglected here. According to the table, the combined solution has the minimum error for Case A2, even smaller than the ANC only

solution, but the difference is small enough to be negligible. For Case A1, the combined solution did not show any improvements over the ANC solution. Hence, the ARMA approximation is not necessary for gravity estimation, but acceleration noise should be considered in the MNC, especially when the residual acceleration noise is large.

Table 6-3. Spatial RMS error for Cases A1 and A2 in units of cm of EWH.

		HI Error (True: 12.44)		Total Error (True: 7.85)		Max. Error	
		Raw	GS	Raw	GS	Raw	GS
Case A1	Initial	11.72	4.50	11.85	3.30	83.15	55.96
	ANC	7.78	3.71	8.11	2.52	46.48	54.67
	Combined	7.78	3.71	8.11	2.53	46.73	54.82
Case A2	Initial	5.47	3.59	4.45	2.11	82.93	52.70
	ANC	5.31	3.55	4.27	2.08	82.39	52.36
	Combined	5.30	3.55	4.26	2.07	82.42	52.34

CHAPTER 7

TOOLBOX VALIDATION USING THE UF PRECISION TORSION PENDULUM

Although instrument noise can be created with given models and be used in simulations as demonstrated in previous chapters, this simulated noise is only a representation of the actual noise. Measurement noise from actual instruments are often far richer and more complex than the noise models used in previous chapters. Therefore, it is desirable to test the toolbox and run the simulation with the actual noise from the existing instruments. The residual acceleration noise of a drag-free system can be obtained from UF precision torsion pendulum, which simulates free-fall of a drag-free test mass in the laboratory environment. This chapter introduces the UF precision torsion pendulum and compares the gravity solutions estimated using noise data taken from the pendulum and the simulated noise.

UF Precision Torsion Pendulum

Cooperative work between the Physics and Aerospace Engineering departments at the University of Florida (UF) is currently developing a facility that is designed to test new technologies for the upcoming Laser Interferometer Space Antenna (LISA) mission, a dedicated space mission aimed to detect gravitational waves in space [Ciani et al., 2017]. Figure 7-1 shows the CAD model and the actual apparatus of the torsion pendulum. As seen from the figure, the system is placed inside the vacuum chamber and the entire system is enclosed in a thermal room to mitigate disturbances due to air currents and thermal fluctuations.

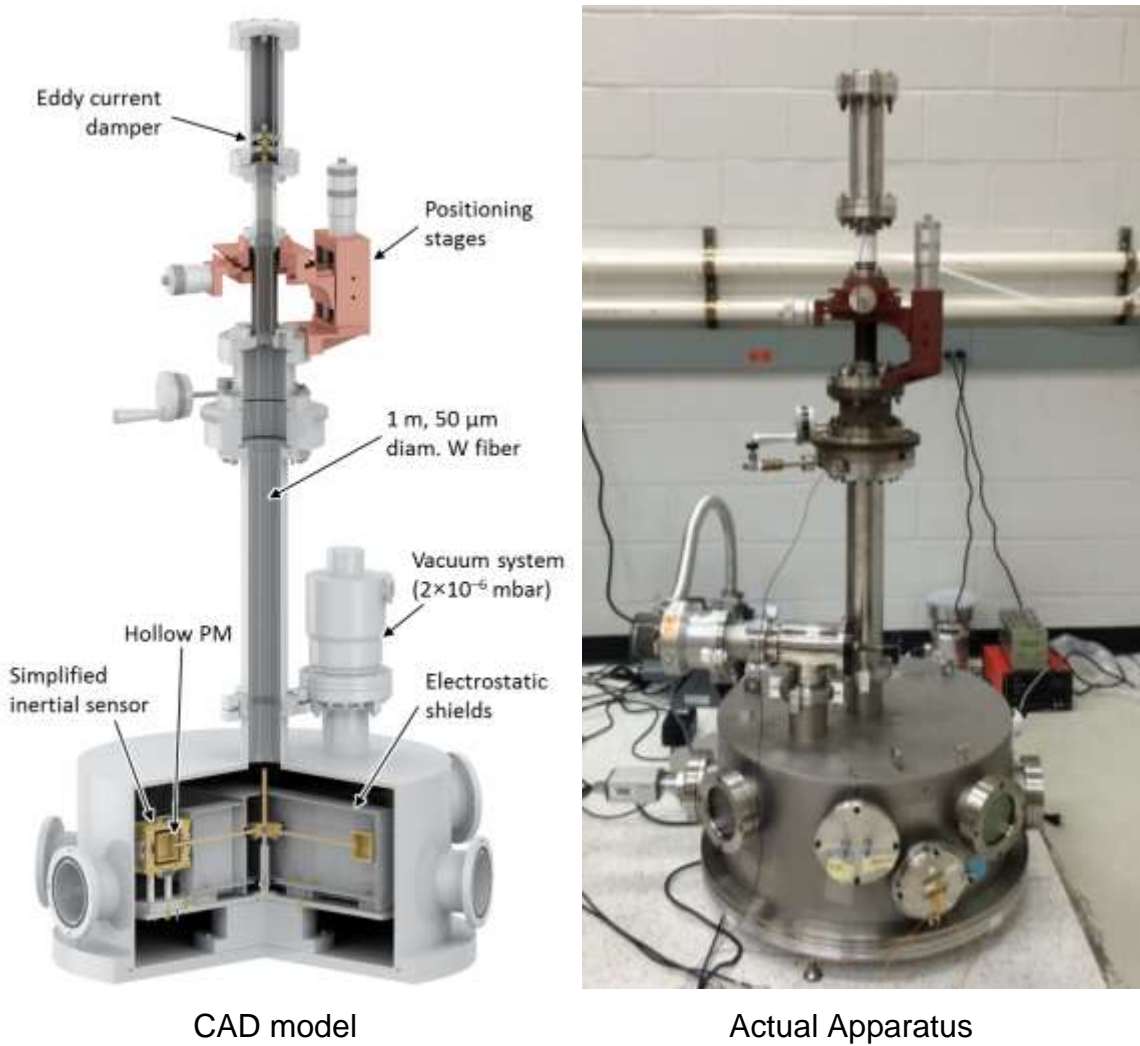


Figure 7-1. CAD model and actual apparatus of a torsion pendulum taken from Physics Space Laboratory at University of Florida in 2015 [Ciani et al., 2017].

UF precision torsion pendulum measures the residual acceleration noise of a proof mass in one degree of freedom by measuring the angle variations along the vertical axis. Figure 7-2 shows the inertial member of the pendulum, which are held by a tungsten fiber. As seen from this figure, two displacements x_1 and x_2 are measured using both capacitive sensor and laser interferometer, which are then used to compute the angle variation, ϕ . This angle measurement is first converted to a torque measurement and then to an acceleration measurement.

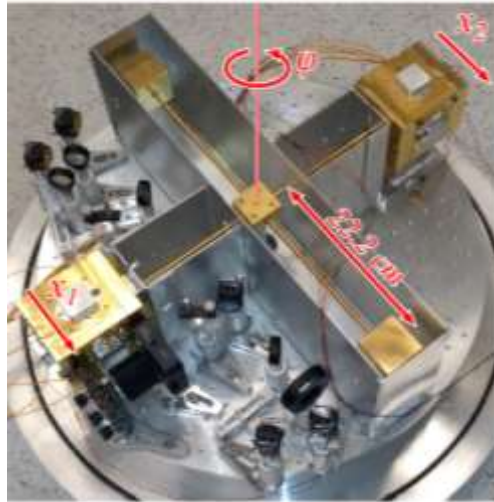


Figure 7-2. Inertial members of a torsion pendulum taken from Physics Space Laboratory at University of Florida in 2017 [Ciani *et al.*, 2017].

Accuracy of the acceleration measurement is aimed to be comparable to the LISA requirement, which is [Chilton *et al.*, 2015]

$$s_a^{1/2} < 3 \times 10^{-15} \left(1 + \left(\frac{f}{3 \text{ mHz}} \right)^2 \right)^{1/2} \frac{\text{m}}{\text{s}^2\sqrt{\text{Hz}}} \quad (7-1)$$

A gravitational reference sensor (GRS) is a key technology of a drag-free system that measures the displacement of a test mass relative to its housing. Therefore, the noise measurement from UF precision torsion pendulum can be used as the actual acceleration noise of a drag-free system. Moreover, LISA is focusing on frequencies between 0.1 mHz and 100 mHz, the same frequency band that satellite geodesy missions are interested in.

Accumulated Acceleration Noise

The acceleration noise measured by the UF precision torsion pendulum in November and December 2016 were accumulated and rearranged to be used in this research. Figure 7-3 shows the amplitude spectral density (ASD) curves of the accumulated noise. The noise data is in 3 hour segments with a sampling

frequency of 8.6 Hz. As seen from the figure, there is a peak caused by the actual swing mode of the pendulum at frequency near 0.4 Hz. This kind of error caused by the pendulum natural dynamics does not exist in an actual drag-free system. Regardless of this peak error, the errors above around 3 mHz are greatly dominated by the measurement system of the pendulum and below this frequency, the noise is dominated by the acceleration noise. Therefore, in order to extract only the acceleration noise, the low pass filter must be applied at frequency of 3 mHz and then appropriate acceleration noise must be added for frequency above 3 mHz. Acceleration noise models for drag-free systems shown in Figure 3-3, tend to decrease and level off at higher frequencies. Accordingly, white noise was added only for the frequencies higher than 3 mHz after applying the low pass filter. Therefore, this added white noise does not alter the noise at low frequencies.

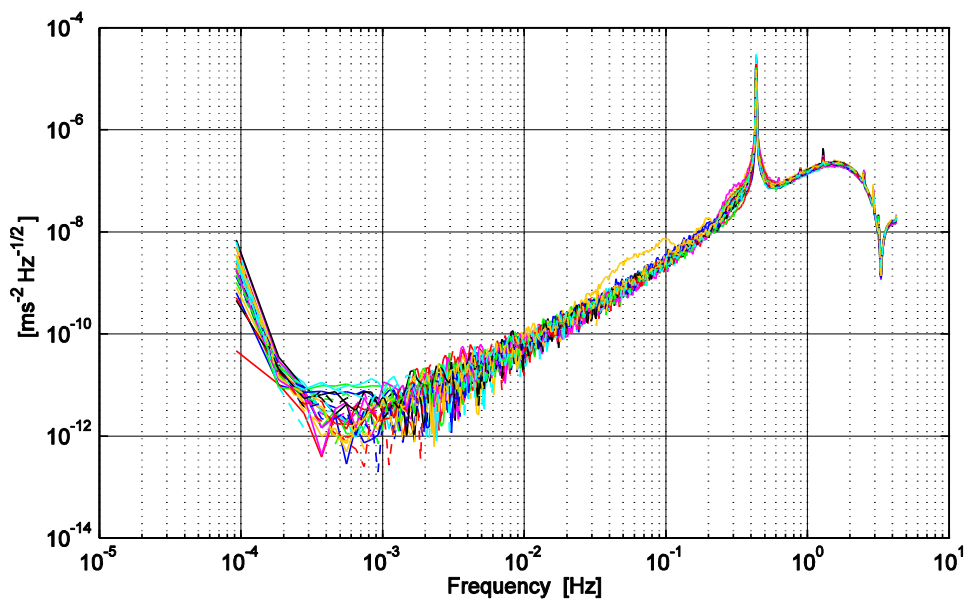


Figure 7-3. ASD of raw acceleration noise data.

In addition, the sampling frequency of the measurements in this research is 0.1 Hz, which is smaller than the sampling frequency of the pendulum. The accumulated acceleration data therefore needs to be reorganized such that the noise data is provided at slower rate. This can be done simply by taking the average of the filtered data for time interval of 10 sec. This new extracted acceleration noise from the accumulated data at 0.1 Hz are shown in Figure 7-4.

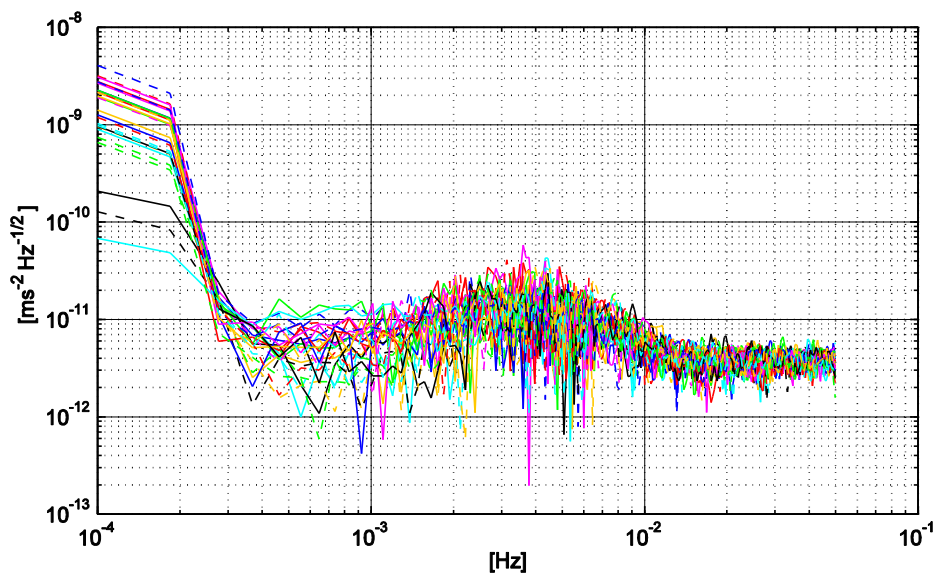


Figure 7-4. ASD of extracted acceleration noise data.

To be able to compare the actual noise with the model-based simulated noise, a simulated noise was created using the method presented in Chapter 3. Figure 7-5 shows ASD curves of actual acceleration noise, simulated acceleration noise and the model used to generate the noise. At the bottom of this figure, the model for the pendulum noise is presented. Also, the GOCE-level drag-free system simulated noise is shown in the same figure. The actual pendulum noise is steeper at low frequency, but other than this, the model-based simulated noise seems to be a good approximation of the actual pendulum noise.

The pendulum noise generally has a similar amplitude as the GOCE-level drag-free system, but the GOCE noise is slightly lower than the pendulum noise for all frequencies. At high frequencies, the pendulum noise has the magnitude of $8 \times 10^{-12} \text{ ms}^{-2}\text{Hz}^{-1/2}$, whereas the GOCE noise has the magnitude of $2 \times 10^{-12} \text{ ms}^{-2}\text{Hz}^{-1/2}$.

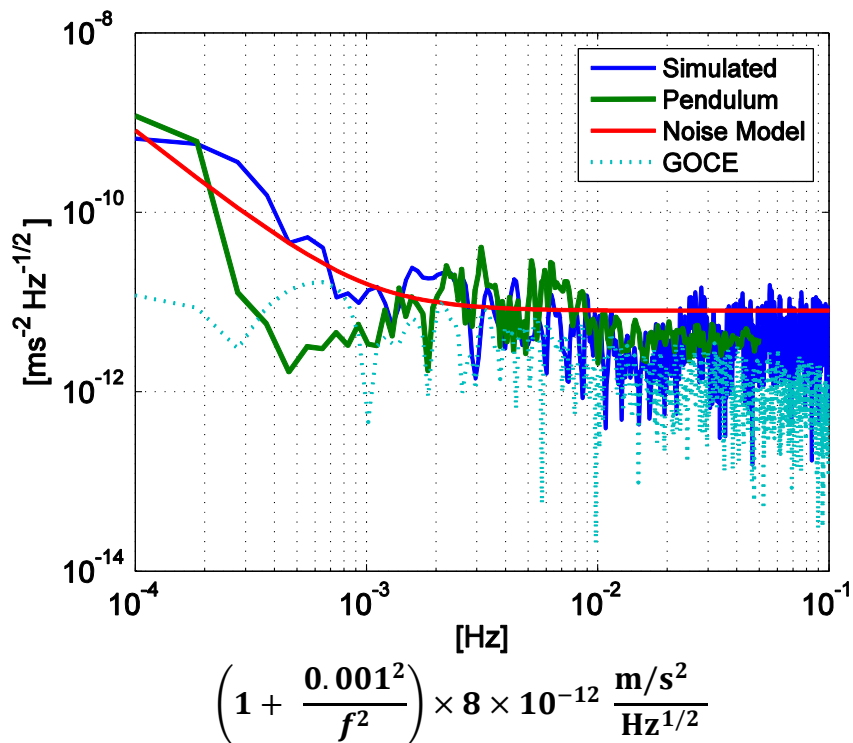


Figure 7-5. ASD of actual pendulum noise, model-based simulated pendulum noise, and GOCE-level simulated acceleration noise. The model of the simulated pendulum noise is shown below the graph.

Result

In total, there are 26 sets of pendulum acceleration noise acquired. These noise data sets were used randomly and evenly to create new measurement data. Also, equal number of simulated acceleration noise sets were created and used to compute measurement data for comparison. The solutions were computed using the same method as discussed in Chapter 4.

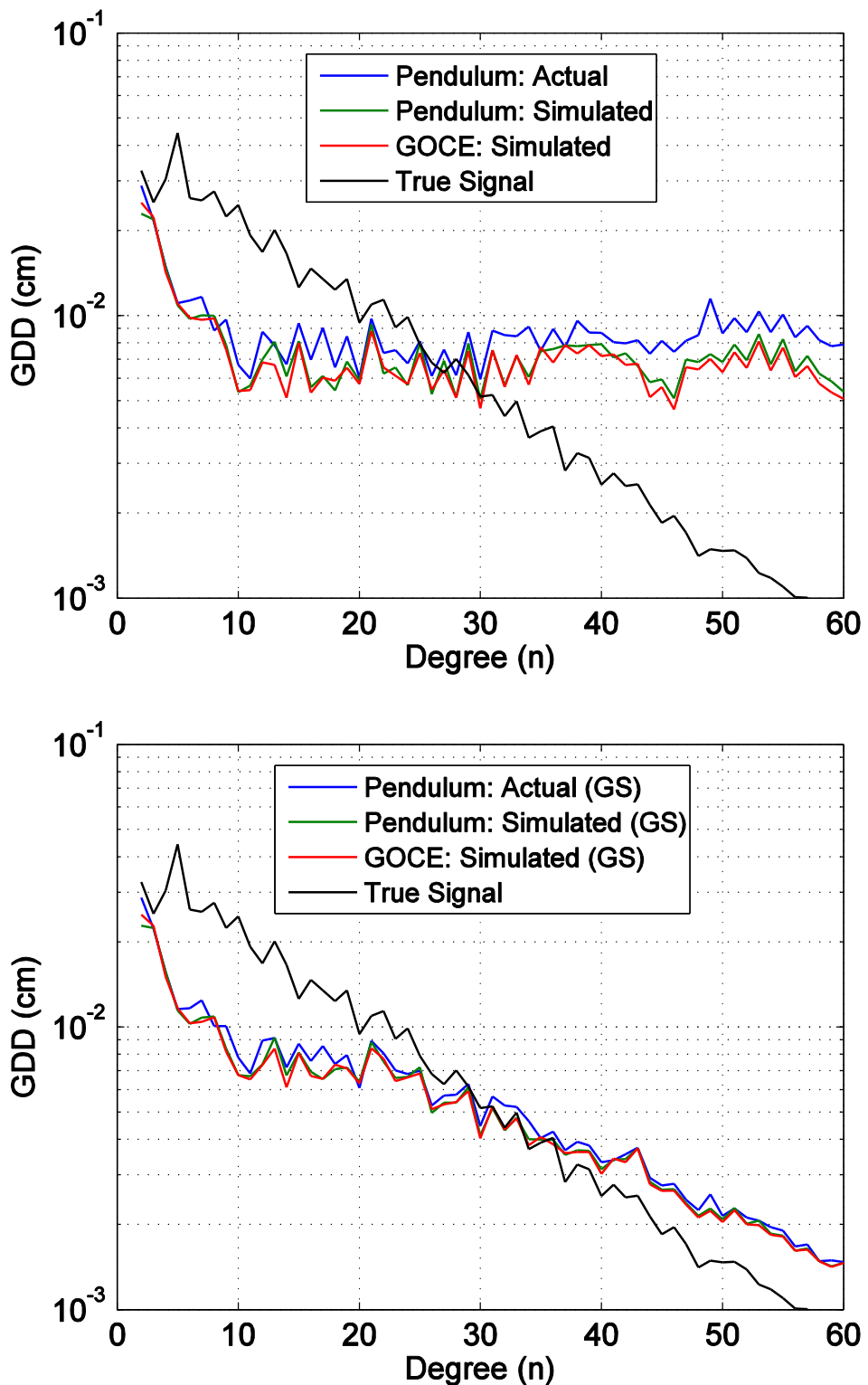


Figure 7-6. Errors of the actual and the simulated UF pendulum noise applied single pair solutions expressed as GDD. Raw errors (top) and GS-applied errors (bottom).

The GDD error curves are shown in Figure 7-6. The raw estimates are shown on top and the filtered solutions are shown on bottom with 300 km radius GS. It is clear from this figure that both cases with actual and generated pendulum noise are somewhat similar. As one would expect, the actual pendulum noise produced a slightly larger error compared to the simulated solutions even when the filter was applied. This is because the actual noise acquired from the pendulum is less consistent compared to the simulated noise. In other words, there are more fluctuations in the magnitude of the ASD of the real noise compared to the simulated noise. However, the main purpose of applying the actual noise is to validate the toolbox. The GDD error plots clearly show that the estimator produces solutions even when the ASD of the noise is more complex than the simulated noise. The solution using the simulated noise of GOCE is also drawn for comparison. It is shown that when the acceleration noise is slightly higher than the GOCE level, it worsens the solution.

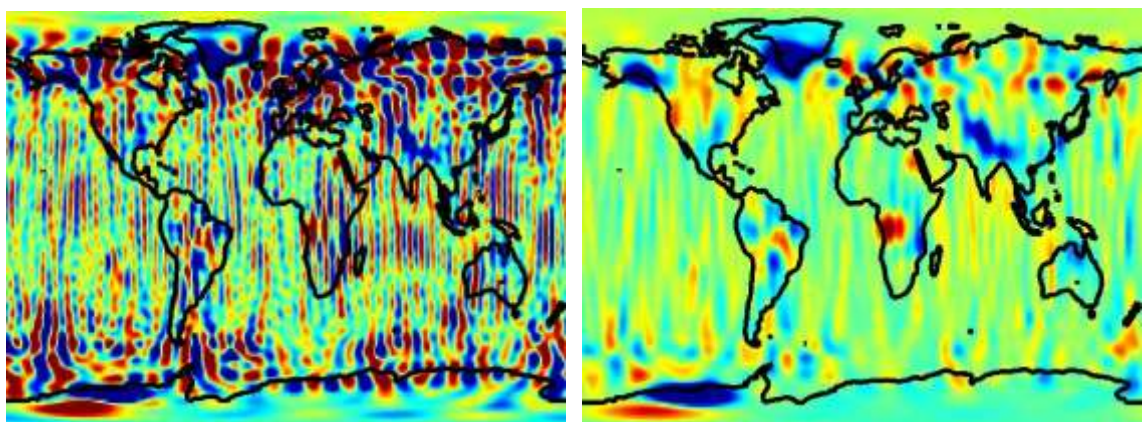


Figure 7-7. Estimated single pair solutions in units of cm of EWH applying the pendulum noise. Actual pendulum noise (row 1), generated pendulum noise (row 2) and generated GOCE noise (row 3), non-filtered (left), and filtered (right) solutions.

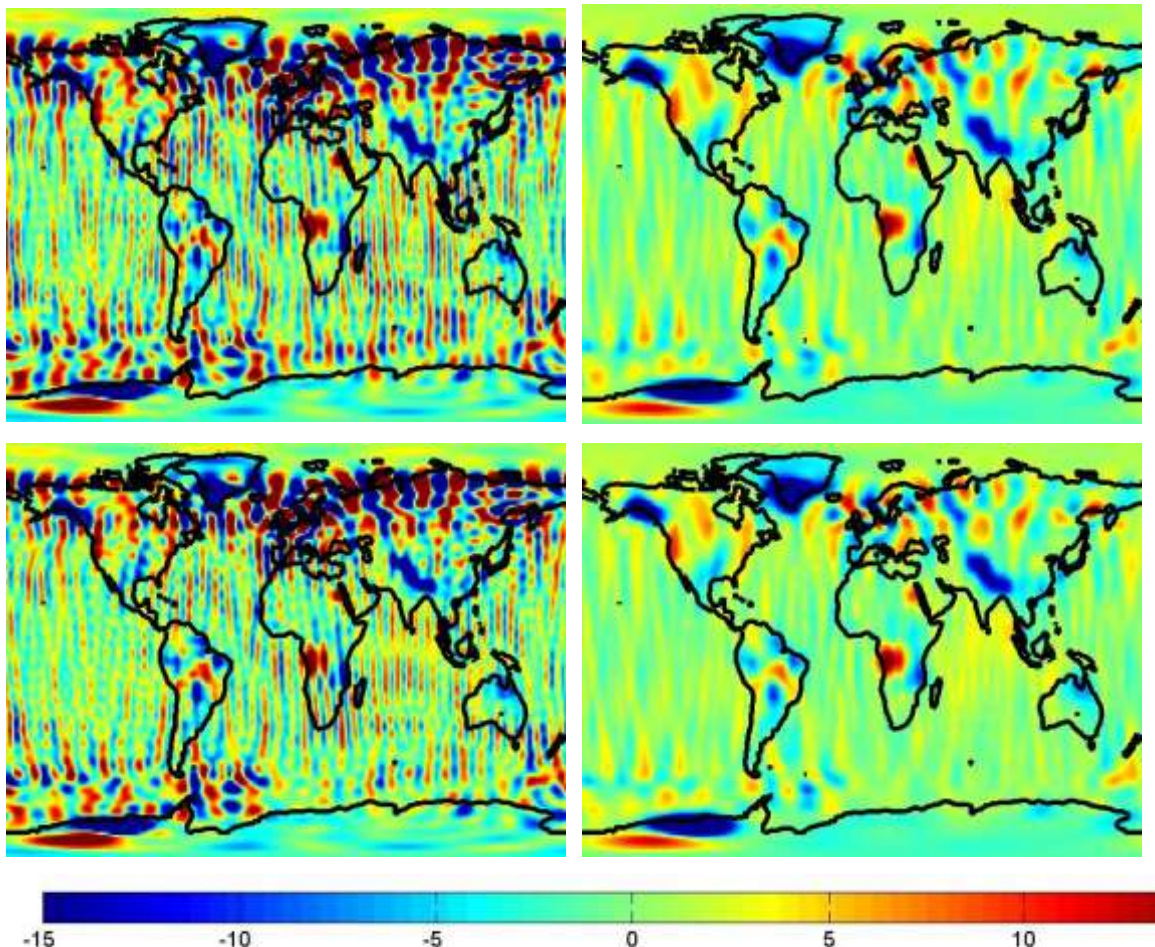


Figure 7-7. Continued.

Figure 7-7 shows the solutions in EWH. Non-filtered solutions are on left and filtered solutions are on right. The first row shows the solutions using the actual pendulum noise and right below them are solutions using the simulated pendulum noise. It is quite clear that more errors are shown in the first row than the second row. This is consistent with what we have seen from the GDD error plots in Figure 7-6. The last row shows the result using the GOCE simulated acceleration noise, and the discrepancies between the GOCE and the pendulum solutions are hard to observe for both raw and GS-applied solutions. Table 7-1 shows the numerical values of the spatial RMS EWH for all three solutions plotted in Figure 7-7. The table values tell us that on average, the actual

pendulum noise case has about 2 cm (26%) larger error compared to the generated pendulum noise. This might seem relatively large, but the actual pendulum noise has a larger variations in the noise data. For this reason, a larger error is expected when actual noise is used compared to simulated noise. If the generated noise was created more carefully constructing a more detailed acceleration noise model, then the two solutions might look more alike. However, the goal was to check the validity of the toolbox used in this simulation by the actual noise and this result proves that the toolbox operates well even when acceleration noise taken from actual hardware is used. The pendulum simulated noise is then compared with the GOCE-level simulated noise. This comparison shows that the pendulum simulated noise case produces a solution with an error of 4~5 mm (10%) higher than the GOCE-level simulated noise (Case A2).

Table 7-1. Spatial RMS error for pendulum cases and Case A2 in units of cm of EWH.

	HI Error (True: 12.44)		Total Error (True: 7.85)		Max. Error	
	Raw	GS	Raw	GS	Raw	GS
Pendulum: Actual	7.65	3.82	6.36	2.43	80.6	51.87
Pendulum: Simulated	5.64	3.61	4.90	2.18	83.16	52.50
GOCE: Simulated	5.47	3.59	4.45	2.11	82.93	52.70

Discussion

In this chapter, the UF precision pendulum was introduced and the residual acceleration noise measured by the pendulum was used to validate the toolbox that was developed and used throughout this research. The accumulated noise from the pendulum had to be modified to be applied in this simulation. Since the raw noise data is the combination of the acceleration and the

measurement noise, the acceleration noise from the raw noise data had to be extracted. This was done by applying a low pass filter and adding appropriate high frequency noise. Then simulated acceleration noise was generated based on this actual noise to compare the solutions. The result showed that the solution was successfully estimated with the actual pendulum noise. This means that the toolbox is stable and produces valid results even when the actual noise is used. Also, the solution was comparable to the solution from the simulated pendulum noise. Although the error magnitude decreased with the simulated noise, if the noise was generated more carefully the two solutions might become more alike. This shows that the generated noise can be a good representation of the actual noise. Finally, by comparing the Case A2 (GOCE acceleration noise) solution with the simulated pendulum noise, we showed that GOCE-level acceleration noise is very close to the optimal value. The acceleration noise difference between Case A2 and A3 are about 2 orders of magnitude. However, pendulum acceleration noise was only 4 times larger than the GOCE acceleration noise and the solution error increased by 4~5 mm (10%), whereas the difference between Case A2 and A3 solutions is only about 0.1 mm (0.2%). This result confirms that in order to reduce the effect of varying residual acceleration noise below 1 mm EWH, the noise magnitude must be reduced below $8 \times 10^{-12} \text{ ms}^{-2} \text{ Hz}^{-1/2}$, close to $2 \times 10^{-12} \text{ ms}^{-2} \text{ Hz}^{-1/2}$.

CHAPTER 8

CONCLUSIONS AND RECOMMENDATIONS

Conclusions

This research accomplished main objectives, which are to build a toolbox for satellite geodesy simulation and to explore the effects of different drag-free systems for future satellite geodesy missions. This toolbox was built using MATLAB from the ground up. There are two parts to this tool box. The first part creates the measurement data of the satellites and the second part uses this measurement to estimate the gravity field solutions. There are six different gravity models; static, ocean tide, ocean bottom pressure, atmosphere, hydrology and ice used in the simulation. The measurement noise and the residual acceleration noise are generated using the noise models provided from the various technology teams, and are utilized in the process of creating measurement data. The estimation part was difficult to achieve due to the large amount of data and parameters. Various methods were applied and the most efficient one in terms of computation time and a convenience, was the partitioned best linear unbiased estimator (weighted least squares estimator). With this unique toolbox, different levels of residual acceleration noise were applied, each corresponding to an existing technology. The simulation was designed that can represent future geodesy mission beyond GRACE-FO. In-line and in-line Bender configurations were both tried in the simulation to evaluate the different levels of aliasing errors. Moreover, both realistic and idealistic de-aliasing models were applied to discover the relation between the acceleration noise and the aliasing error, which are the main concerns for the next generation geodesy missions. Through repeated simulation, it was concluded that the acceleration noise level

of the drag-free system for future LL-SST mission is close to $2 \times 10^{-12} \text{ ms}^{-2} \text{ Hz}^{1/2}$, and any further reduction of this acceleration noise is not necessary even when aliasing error is reduced dramatically using idealistic de-aliasing models and the in-line Bender configuration.

In addition, the actual residual acceleration noise from the UF precision torsion pendulum was used to validate the toolbox. The noise from UF precision torsion pendulum not only validated the toolbox, but it also explored an additional level of acceleration noise which was 4 times larger than the GOCE drag-free system noise. The solution using the UF pendulum acceleration noise showed that the acceleration noise must be reduced down to GOCE level, in order to reduce the effect of acceleration noise below 1 mm of EWH.

Moreover, the estimation routine was revisited by removing some of the assumptions regarding the noise. The ARMA approximation and the ANC methods were introduced to modify the measurement noise covariance matrix. The ARMA approximation was applied to consider the correlation of the noise and the ANC was applied to add the effects of acceleration noise on the measurement. It was shown that the ANC improved the EWH results by ~30% at GRACE-level and ~3% at GOCE-level acceleration noise. However, the ARMA approximation increased the EWH error for both cases.

Recommendations for Future Research

There are several recommendations for the future research. Updating the toolbox is highly recommended. First, the toolbox can be converted to different programming language to increase the speed of computation because MATLAB is inefficient at processing large volumes of data. This way, more parameters can

be estimated, increasing the spatial resolution of the solution and saving computation time. Also, this toolbox uses spherical harmonic coefficients to represent the gravity field. Instead of spherical harmonic coefficients, mascon parameters can be used [Save *et al.*, 2016]. This new class of parameters are more accurate because each of parameter represents a single independent grid of the map, whereas one spherical harmonic coefficient effects the entire globe.

Optimizing the arc length should also be explored. Currently, different institutions use different arc length. However, there is no dedicated study done to find the optimal arc length.

It would be valuable to do a research on CubeSat-based geodesy missions. Accurate mathematical models and data from the actual hardware can be applied to this toolbox and the efficiency of CubeSats on geodesy missions could be explored. Multiple CubeSat formations can be considered, and the optimal orbits for multiple CubeSats could be found and compared to the one and two-pair GRACE-like missions.

LIST OF REFERENCES

- Antonucci, F., Armano, M., Audley, H., Auger, G., Benedetti, M., Binetruy, P., ... & Caleno, M. (2012). The LISA pathfinder mission. *Classical and Quantum Gravity*, 29(12), 124014.
- Armano, M., Audley, H., Auger, G., Baird, J., Binetruy, P., Born, M., ... & Cavalleri, A. (2015). The LISA pathfinder mission. In *Journal of Physics: Conference Series* (Vol. 610, No. 1, p. 012005). IOP Publishing.
- Armano, M., Audley, H., Auger, G., Baird, J. T., Bassan, M., Binetruy, P., ... & Carbone, L. (2016). Sub-femto-g free fall for space-based gravitational wave observatories: LISA pathfinder results. *Physical Review Letters*, 116(23), 231101
- Barthelmes, F. (2009). Definition of functionals of the geopotential and their calculation from spherical harmonic models. [http://publications.iass-potsdam.de/pubman/item/escidoc_104132\(3\)_0902-2](http://publications.iass-potsdam.de/pubman/item/escidoc_104132(3)_0902-2).
- Bettadpur, S. (2012). UTCNR Level-2 processing standards document for Level-2 product release 5.
- Bruinsma, S. L., Förste, C., Abrikosov, O., Marty, J. C., Rio, M. H., Mulet, S., & Bonvalot, S. (2013). The new ESA satellite-only gravity field model via the direct approach. *Geophysical Research Letters*, 40(14), 3607-3612.
- Canuto, E., & Massotti, L. (2009). All-propulsion design of the drag-free and attitude control of the European satellite GOCE. *Acta Astronautica*, 64(2), 325-344.
- Chen, Q., Shen, Y., Chen, W., Zhang, X., & Hsu, H. (2016). An improved GRACE monthly gravity field solution by modeling the non-conservative acceleration and attitude observation errors. *Journal of geodesy*, 90(6), 503-523.
- Chilton, A., Shelley, R., Olatunde, T., Ciani, G., Conklin, J. W., & Mueller, G. (2015). The UF Torsion Pendulum, a LISA Technology Testbed: Sensing System and Initial Results. In *Journal of Physics: Conference Series* (Vol. 610, No. 1, p. 012038). IOP Publishing.
- Ciani, G., Aitken, M., Apple, S., Chilton, A., Olatunde, T., Mueller, G., & Conklin, J. W. (2017). A New Torsion Pendulum for Gravitational Reference Sensor Technology Development. *arXiv preprint arXiv:1701.08911*.
- Conklin, J. W. (2015). Drift mode accelerometry for spaceborne gravity measurements. *Journal of Geodesy*, 89(11), 1053-1070.
- Dahle, C. (2013). GFZ Level-2 processing standards document for Level-2 product release 5.

- DeBra, D. B., & Conklin, J. W. (2011). Measurement of drag and its cancellation. *Classical and Quantum Gravity*, 28(9), 094015.
- Dobslaw, H., Flechtner, F., Bergmann-Wolf, I., Dahle, C., Dill, R., Esselborn, S., ... & Thomas, M. (2013). Simulating high-frequency atmosphere-ocean mass variability for dealiasing of satellite gravity observations: AOD1B RL05. *Journal of Geophysical Research: Oceans*, 118(7), 3704-3711.
- Dobslaw, H., Bergmann-Wolf, I., Dill, R., Forootan, E., Klemann, V., Kusche, J., & Sasgen, I. (2015). The updated ESA Earth System Model for future gravity mission simulation studies. *Journal of Geodesy*, 89(5), 505-513.
- Dolesi, R., Bortoluzzi, D., Bosetti, P., Carbone, L., Cavalleri, A., Cristofolini, I., ... & Hoyle, C. D. (2003). Gravitational sensor for LISA and its technology demonstration mission. *Classical and quantum gravity*, 20(10), S99.
- Elsaka, B., Raimondo, J. C., Brieden, P., Reubelt, T., Kusche, J., Flechtner, F., ... & Müller, J. (2013). Comparing seven candidate mission configurations for temporal gravity field retrieval through full-scale numerical simulation. *Journal of Geodesy*, 88(1), 31-43.
- Elsaka, B. (2014). Sub-monthly gravity field recovery from simulated multi-GRACE mission type. *Acta Geophysica*, 62(1), 241-258.
- Flechtner, F. (2007). AOD1B Product Description Document for Product Releases 01 to 04 (Rev. 3.1, April 13, 2007). *GRACE project document*, 327-750.
- Flechtner, F., Dobslaw, H., & Fagioli, E. (2014). AOD1B Product Description Document for Product Release 05 (Rev. 4.2, May 20, 2014). *Tech. Rep.*, GFZ German Research Centre for Geosciences, Potsdam.
- Flechtner, F., Morton, P., Watkins, M., & Webb, F. (2014). Status of the GRACE follow-on mission. In *Gravity, geoid and height systems* (pp. 117-121). Springer International Publishing.
- Flechtner, F., Neumayer, K. H., Dahle, C., Dobslaw, H., Fagioli, E., Raimondo, J. C., & Guntner, A. (2016). What can be expected from the GRACE-FO Laser Ranging Interferometer for Earth Science applications?. In *Remote Sensing and Water Resources* (pp. 263-280). Springer International Publishing.
- Floberghagen, R., Fehringer, M., Lamarre, D., Muzi, D., Frommknecht, B., Steiger, C., ... & Da Costa, A. (2011). Mission design, operation and exploitation of the gravity field and steady-state ocean circulation explorer mission. *Journal of Geodesy*, 85(11), 749-758.
- Flury, J., Bettadpur, S., & Tapley, B. D. (2008). Precise accelerometry onboard the GRACE gravity field satellite mission. *Advances in Space Research*, 42(8), 1414-1423.

- Foerste, C., Flechtner, F., Schmidt, R., Stubenvoll, R., Rothacher, M., Kusche, J., ... & Bruinsma, S. (2008, April). EIGEN-GL05C-A new global combined high-resolution GRACE-based gravity field model of the GFZ-GRGS cooperation. General Assembly European Geosciences Union (Vienna, Austria 2008), *Geophysical Research Abstracts 10* (EGU2008-A-06944).
- Gruber, T., Bamber, J. L., Bierkens, M. F. P., Dobslaw, H., Murböck, M., Thomas, M., ... & Visser, P. N. A. M. (2011). Simulation of the time-variable gravity field by means of coupled geophysical models. *Earth System Science Data*, 3(1), 19-35.
- Heinzel, G., Sheard, B., Brause, N., Danzmann, K., Dehne, M., Gerberding, O., ... & Klipstein, W. (2012). Laser ranging interferometer for GRACE follow-on. In *Proceeding of International Conference on Space Optics (ICSO)(Ajaccio, Corsica, France, 2012)*.
- Heiskanen, W. A., & Moritz, H. (1967). Physical geodesy. *Bulletin Géodésique (1946-1975)*, 86(1), 491-492.
- Kang, Z., Tapley, B., Bettadpur, S., Ries, J., Nagel, P., & Pastor, R. (2006). Precise orbit determination for the GRACE mission using only GPS data. *Journal of Geodesy*, 80(6), 322-331.
- Kasdin, N. J. (1995). Discrete simulation of colored noise and stochastic processes and $1/f^{1/\alpha}$ power law noise generation. *Proceedings of the IEEE*, 83(5), 802-827.
- Kim, J. (2000). *Simulation study of a low-low satellite-to-satellite tracking mission* (Doctoral dissertation, The University of Texas at Austin).
- Klees, R., Ditmar, P., & Broersen, P. (2003). How to handle colored observation noise in large least-squares problems. *Journal of Geodesy*, 76(11-12), 629-640.
- Klinger, B., & Mayer-Gürr, T. (2016). The role of accelerometer data calibration within GRACE gravity field recovery: Results from ITSG-Grace2016. *Advances in Space Research*, 58(9), 1597-1609.
- Kurtenbach, E., Mayer-Gürr, T., & Eicker, A. (2009). Deriving daily snapshots of the Earth's gravity field from GRACE L1B data using Kalman filtering. *Geophysical Research Letters*, 36(17).
- Loomis, B. D., Nerem, R. S., & Luthcke, S. B. (2012). Simulation study of a follow-on gravity mission to GRACE. *Journal of Geodesy*, 86(5), 319-335.
- Lyard, F., Lefevre, F., Letellier, T., & Francis, O. (2006). Modelling the global ocean tides: modern insights from FES2004. *Ocean Dynamics*, 56(5-6), 394-415.
- Montenbruck, O., & Gill, E. (2005). *Satellite orbits Models, Methods and Applications*. (3rd Edition) New York: Springer.

- Moore, P., Zhang, Q., & Alothman, A. (2005). Annual and semiannual variations of the Earth's gravitational field from satellite laser ranging and CHAMP. *Journal of Geophysical Research: Solid Earth*, 110(B6).
- Nerem, R. S., Jekeli, C., & Kaula, W. M. (1995). Gravity field determination and characteristics: retrospective and prospective. *Journal of Geophysical Research: Solid Earth*, 100(B8), 15053-15074.
- Nguyen, A. (2016). *Small satellite technologies for precision drag-free control and drag force recovery* (Doctoral dissertation, The University of Florida).
- Nguyen, A., & Conklin, J. W. (2015). Three-Axis Drag-Free Control and Drag Force Recovery of a Single-Thruster Small Satellite. *Journal of Spacecraft and Rockets*, 52(6), 1640-1650.
- Pail, R., Bingham, R., Braatenberg, C., Dobslaw, H., Eicker, A., Guntner, A., ... & Wouters, B. (2015). Science and user needs for observing global mass transport to understand global change and to benefit society. *Surveys in geophysics*, 36(6), 743-772.
- Petovello, M. G., O'Keefe, K., Lachapelle, G., & Cannon, M. E. (2009). Consideration of time-correlated errors in a Kalman filter applicable to GNSS. *Journal of Geodesy*, 83(1), 51-56.
- Reigber, C., Schwintzer, P., Neumayer, K. H., Barthelmes, F., König, R., Förste, C., ... & Bruinsma, S. (2003). The CHAMP-only Earth gravity field model EIGEN-2. *Advances in Space Research*, 31(8), 1883-1888.
- Rieser, D., Mayer-Gürr, T., Savcenko, R., Bosch, W., Wünsch, J., Dahle, C., & Flechtner, F. (2012). The ocean tide model EOT11a in spherical harmonics representation. URL: http://portal.tugraz.at/portal/page/portal/Files/i5210/files/projekte/COTAGA/TN_EOT11a.pdf.
- Sakumura, C., Bettadpur, S., Save, H., & McCullough, C. (2016). High-frequency terrestrial water storage signal capture via a regularized sliding window mascon product from GRACE. *Journal of Geophysical Research: Solid Earth*, 121(5), 4014-4030.
- Savcenko, R., & Bosch, W. (2012). EOT11a-empirical ocean tide model from multi-mission satellite altimetry.
- Save, H., Bettadpur, S., & Tapley, B. D. (2016). High-resolution CSR GRACE RL05 mascons. *Journal of Geophysical Research: Solid Earth*, 121(10), 7547-7569.
- Seeber, G. (2003). *Satellite geodesy: foundations, methods, and applications*. Walter de Gruyter.

- Sheard, B. S., Heinzel, G., Danzmann, K., Shaddock, D. A., Klipstein, W. M., & Folkner, W. M. (2012). Intersatellite laser ranging instrument for the GRACE follow-on mission. *Journal of Geodesy*, 86(12), 1083-1095.
- Sneeuw, N., Flury, J., & Rummel, R. (2005). Science requirements on future missions and simulated mission scenarios. In *Future Satellite Gravimetry and Earth Dynamics* (pp. 113-142). Springer New York.
- Stoica, P., & Moses, R. L. (1997). *Introduction to spectral analysis* (Vol. 1, pp. 3-4). Upper Saddle River: Prentice hall.
- Stoyanov, M., Gunzburger, M., & Burkardt, J. (2011). Pink noise, $1/f^\alpha$ noise, and their effect on solutions of differential equations. *International journal for uncertainty quantification*, 1(3).
- Swenson, S., & Wahr, J. (2002). Methods for inferring regional surface-mass anomalies from Gravity Recovery and Climate Experiment (GRACE) measurements of time-variable gravity. *Journal of Geophysical Research: Solid Earth*, 107(B9).
- Tapley, B. D., Bettadpur, S., Watkins, M., & Reigber, C. (2004). The gravity recovery and climate experiment: Mission overview and early results. *Geophysical Research Letters*, 31(9).
- Tapley, B. D., Ries, J., Bettadpur, S., Chambers, D., Cheng, M., Condi, F., & Poole, S. (2007, December). The GGM03 mean earth gravity model from GRACE. In *AGU Fall Meeting Abstracts* (Vol. 1, p. 03).
- Touboul, P., Foulon, B., Christophe, B., Marque, J.P., (2012). CHAMP, GRACE, GOCE instruments and beyond. *Geodesy for planet earth*. In: Kenyon, S., et al. (Eds.), IAGS, vol. 136, pp. 215–221.
- Vtipil, S., & Newman, B. (2012). Determining an Earth Observation Repeat Ground Track Orbit for an Optimization Methodology. *Journal of Spacecraft and Rockets*, 49(1), 157-164.
- Wahr, J., Molenaar, M., & Bryan, F. (1998). Time variability of the Earth's gravity field: Hydrological and oceanic effects and their possible detection using GRACE. *Journal of Geophysical Research: Solid Earth*, 103(B12), 30205-30229.
- Watkins, M. M., & Yuan, D. N. (2012). JPL Level-2 processing standards document for Level-2 product release 5.
- Wiese, D. N. (2011). *Optimizing two pairs of GRACE-like satellites for recovering temporal gravity variations* (Doctoral dissertation, The University of Colorado).
- Wiese, D. N., Nerem, R. S., & Lemoine, F. G. (2012). Design considerations for a dedicated gravity recovery satellite mission consisting of two pairs of satellites. *Journal of Geodesy*, 86(2), 81-98.

BIOGRAPHICAL SKETCH

Seong Hyeon Hong received his bachelor's (B.S.) degree in mechanical and electronic control engineering as a dual degree in Feb. 2012. He did his entire undergraduate at the Handong Global University (HGU) starting from Mar. 2005. Between his undergraduate years, he served in the Republic of Korea military for two years from 2007 to 2009. At HGU, he was a member of robotics group and participated in the national robot competition with unmanned vehicles. He worked on building a two-wheeled self-balancing vehicle with a linear quadratic controller for his thesis.

Seong Hyeon began his graduate study from Aug. 2012 at University of Florida. He was awarded with Master of Science (M.S.) degree in Dec. 2013 in mechanical engineering. He continued his graduate study at University of Florida in a Ph.D. program. During his time at University of Florida, he worked as a research assistant in Precision Space Systems Laboratory from Jan. 2013 to Apr. 2017. His research field was satellite geodesy, specifically working on the effects of drag-free system acceleration noise levels for future low-low satellite-to-satellite tracking missions. For this research, he built a new toolbox that can be used to simulate satellite geodesy missions and estimate gravity field solutions. He also served as a teaching assistant for Mechanical and Aerospace Engineering Department from Jan. 2013 to Apr. 2017. He served as a mentor for a student with a learning disability with the same major from Aug. 2014 to Apr. 2015. In the summer 2016, he did internship at Korea Helicopter Company in South Korea. He worked on building commercial quadrotors, which spray agricultural chemicals.

Seong Hyeon will be awarded with Doctor of Philosophy (Ph.D.) degree as a mechanical engineering major in May 2017 at University of Florida. He will continue to work on advanced research with experience he gained at University of Florida.